University of Trieste

PhD School in Physics

Analysis and estimation of the scientific performance of the GAMMA-400 experiment

Candidate:
Paolo Cumani

Academic Supervisor:
Dr. Anna Gregorio

Supervisor:
Dr. Francesco Longo

Co-Supervisor:
Dr. Valter Bonvicini

Academic year 2013–2014

Contents

Introduction

Both gamma-ray and cosmic-ray physics still present a number of unresolved issues, many of which can only be faced with a joint study of the two channels of information. Ranging from the nature of Dark Matter to the origin and propagation of cosmic rays, the multi-messenger approach is one of the most promising ways to tackle the unanswered questions in astroparticle physics. GAMMA-400, thanks to its dual nature, devoted to the study of both gamma rays and cosmic rays (electrons, protons and nuclei), will address these issues.
GAMMA-400 is a Russian space mission with an international contribution. At the moment the main contributors are Italy, Sweden and Ukraine. The launch is currently scheduled for the end of the decade by means of a Proton-M rocket. GAMMA-400 will be installed on the platform Navigator, manufactured by Lavochkin, and it will have a total mass of 4100 kg, 2 kW of power budget and a telemetry downlink capability of 100 GB/day. A lifetime of at least seven years is guaranteed by the manufacturer.
The foreseen orbit will have an inclination of 51.8° and, initially, a high eccentricity. The initial apogee and perigee will be, respectively, at 300000 and 500 km. The orbit after five months will become more circular, with a radius of $\sim$ 200000 km. This kind of high altitude orbit, while presenting some disadvantages for gamma-ray observations related mainly to the high background from charged particles, it is particularly interesting when combined with the planned observation strategy. GAMMA-400 will operate in pointing mode, observing a portion of the sky with long exposure and not surveying the sky at each orbit. This kind of orbit allows observation without Earth occultation which, in a low earth orbit, reduces the available observation time. In addition, the calorimeter acceptance for cosmic-ray study is wider with respect to satellites in a low Earth orbit, thanks to the possibility to study particles arriving from direction with incidence angle even greater than 90°, normally shadowed by the Earth in lower orbits.
The purpose of this work is to study the performance of GAMMA-400 for gamma-ray observations. In order to do so I have:

- developed a reconstruction algorithm that uses information from different

parts of the apparatus,

- implemented a preliminary set of trigger conditions,
- applied the reconstruction and trigger algorithms to the detection of fast transients.

My work is presented in the chapters from 4 to 6 (with the exception of the fitting method using only information from the calorimeter described in sec. 4.2).
After a review of the current science objectives in gamma-ray and cosmic-ray physics in chap. 1 and the present gamma-ray space missions in chap. 2, the GAMMA-400 instrument configuration will be presented in chap. 3. My algorithm to reconstruct the direction of the incoming gamma ray will be presented in chap. 4, while the results of a preliminary study of a trigger system for gamma-ray observation will be presented in chap. 5. The results obtained will be used on a science case (detection of fast transients) described in chap. 6. Some conclusions will be drawn in the final chapter.

Chapter 1

GAMMA-400 Scientific Objectives

Many questions in cosmic-ray and gamma-ray physics are still unanswered. GAMMA-400 is designed as a dual instrument capable of detecting both gamma rays, electrons, protons and nuclei. The possibility of a simultaneous study using different channels of information will provide a complete investigation of many of these questions.
The chapter is divided into four sections. In each section the present understanding of a different issue and different ways to tackle it, are presented. Starting with the search of Dark Matter related signal (sec. 1.1), the chapter will also cover the origin and propagation of cosmic rays (sec. 1.2), the nature of transients (sec. 1.3) and observations related to cosmology (sec. 1.4).

1.1 Indirect Dark Matter Detection

Dark Matter (DM) is the main component of a large fraction of the Universe. The nature of this elusive particle and how it couples to other particles represents still an unresolved problem. In the past few years many models were created, a graphic view of which is presented in fig. 1.1.

Searches for DM signals are performed with different techniques (see fig. 1.2) depending on the type of coupling of the DM particle. In the case of interaction with Standard Model particles, the research can be made directly, indirectly or using particle colliders. The results of each search channel are complementary and help in setting limits to the mass and cross section of the DM candidate. Weakly Interacting Massive Particles (WIMPs) remain the primary candidate for the cosmological dark matter, even though the LHC has not found any new particles in sub TeV energy range (apart form the Higgs boson) [3].
GAMMA-400 will be able to perform indirect search of DM by means of both

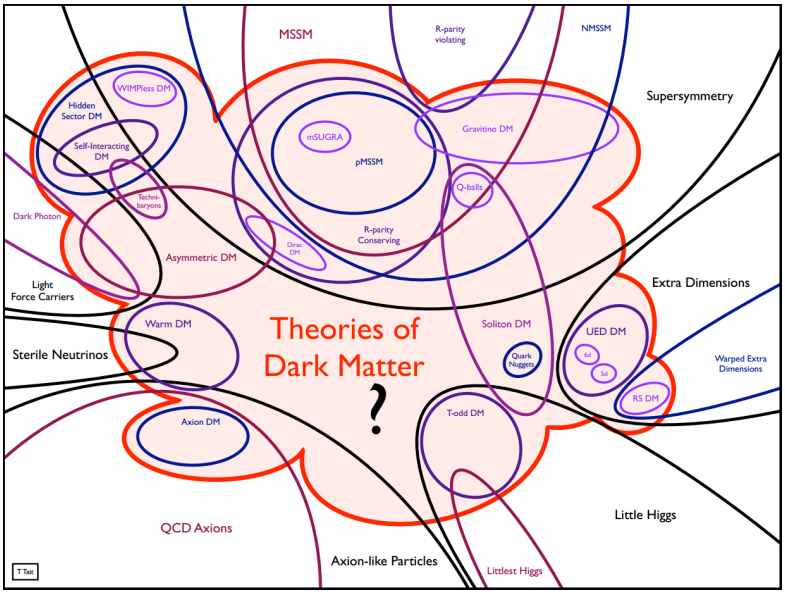

Figure 1.1: Graphic representation of the possible models of Dark Matter [1].

gamma rays (sec. 1.1.1) and cosmic rays (sec. 1.1.2).

1.1.1 Gamma-ray Spectrum

The indirect detection of DM particles using gamma rays searches for the results of the particle decay or annihilation. These processes leave features in the gamma-ray spectrum that can vary from one or more lines, the detection of which would be a "smoking gun", to bumps depending on the DM candidate. The flux from WIMP annihilation can be expressed as

$$\Phi_{WIMP}(E,\psi) = \frac{1}{2}\frac{<\sigma v>}{4\pi}\sum_f \frac{dN_f}{dE}B_f \int_{l.o.s.} dl(\psi)\frac{\rho(l)^2}{m^2_{WIMP}},$$

where σ is the total mean annihilation cross section, v is the relative velocity of the particles, $\rho(l)$ is the density of DM, and $(dN_f/dE)\cdot B_f$ is the photon yield of a particular annihilation channel multiplied by its branching ratio [4].
The flux is expected to be proportional to both the cross section of the annihilation process and the density square of the DM in the region observed. The regions of interest in the DM search are:

- the Galactic Center;

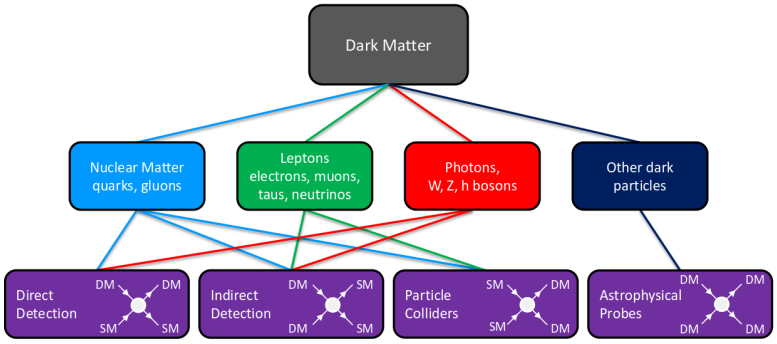

Figure 1.2: Dark Matter interaction chart and related searches techniques [2].

- Dwarf Spheroidal Galaxies;
- Unidentified high-latitude gamma-ray sources. These sources could possibly be DM clumps, or satellites.

The observations made by Fermi [5] of Milky Way satellite galaxies, although there was no significant signal, were able to give some upper limits on dark matter annihilation cross section [6; 7].
The Galactic Center (GC), while theoretically presenting the highest DM density and thus photon flux, presents some observational challenges. The high background from unresolved sources is the main problem. Looking to the GC and subtracting the contribution from the known background a line-like feature at 133 GeV (see left of fig. 1.3) appears in the Fermi-LAT data. Firstly reported in [8], the line, if indeed related to DM annihilation, would correspond to a dark matter mass of $\sim$ 150 GeV. The line is found to be strongly correlated with the GC, nearby galaxy clusters and unassociated sources but not with dwarf galaxies [9]. The reasons why this could not be claimed as a discovery are mainly three: the significance of the line itself, its presence also in some of the so-called control regions and the fact that is narrower than the expected energy resolution. The global significance of 3.1 σ [8] reported at the beginning was found to be overestimated and it drops to a global significance of 1.5 σ (local significance of 3.3 σ) with the addition of new data and taking in consideration possible systematic effects [9]. The progress of the significance with the adding of new data is shown on the right of fig. 1.3. The control regions are expected to contain little or no DM, thus the line should not be present in the spectra of these regions. One of these regions is the Earth Limb. The Limb is a very bright γ-ray source of secondary gamma rays produced by cosmic-ray interactions in the upper atmosphere. The line is instead visible in this region with a low but still troublesome significance of 1 σ. However the line does not appear in other control regions, excluding an explanation entirely

based on systematic effects.

More recently a spatially extended excess at ∼1-3 GeV was found in the GC [11]. The excess is found to be robust and statistically significant. The add of a DM component to the spectrum fit is statistically favoured by a factor of tens of σ. This excess has a spectrum and angular distribution that are in agreement with what expected from annihilating DM. The best DM candidate in this case is a 31-40 GeV particle annihilating to $b\bar{b}$. Other explanations of the excess such as millisecond pulsars are disfavoured since their spectra are softer than the observed excess at energies below ∼1 GeV (see fig. 1.4). These results were obtained under the assumption of a steady-state source. If this theoretical hypothesis is dropped, other alternatives in fitting the excess at the GC appear [12]. The main spectral and angular features of the excess can be reproduced by the inverse Compton emission from a population of high-energy electrons accelerated in a burst event about 10^6 years ago. Other independent evidences seem to confirm the hypothesis of a very active GC over similar timescales. One of these evidences is the recently discovered Fermi bubbles, described in sec. 1.2.7.

GAMMA-400, thanks to a better angular resolution at high energies compared to Fermi (a factor of ~ 2 at 100 GeV), will be able to disentangle the contributions from different sources in the GC [13]. In addition, thanks to the improvement in energy resolution, of the order of 1% starting from 10 GeV, the features in the spectrum, whether line-like or bump-like, will be resolved better [13; 14]. The better energy resolution helps also in the discrimination of different DM candidates (e.g. [15]), thanks to the possible detection, or lack of, different spectral shapes.

1.1.2 Electrons spectrum

In 2008 ATIC (Advanced Thin Ionization Calorimeter, a balloon-borne experiment [18]) [19] reported the measurement of an excess between 300 and 800 GeV in the all electron spectrum ($e^- + e^+$). The spectrum was found to be higher than the result of calculation using a conventional diffusive model (e.g [16]) for energies $\gtrsim$ 100 GeV. This measurement, combined with the rise in the e^+ fraction reported by PAMELA (Payload for Antimatter Matter Exploration and Light-nuclei Astrophysics, see [20] for a description of the experiment) [21] and later confirmed by Fermi [22] and more recently by AMS (Alpha Magnetic Spectrometer, an experiment mounted on the International Space Station[23]) [24], was interpreted as a contribution from DM. Alternative interpretations include a contribution from a nearby electron source like pulsar or a supernova remnant (see also sec. 1.2.2).

Follow-up observations made by H.E.S.S. (High Energy Spectroscopic System [26]) showed a spectrum compatible, within statistical and systematic errors, with the one computed by ATIC, with a steepening at energies greater than $\sim$ 1 TeV

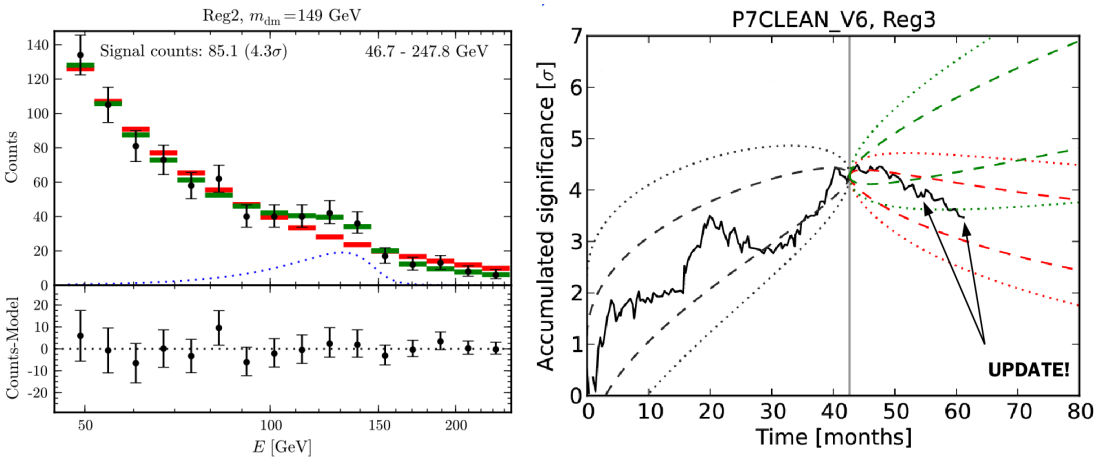

Figure 1.3: *Left*: Fit to data using background only (red bars) and adding the DM signal (green bars). The blue line corresponds to the flux of the virtual internal bremsstrahlung [8]. *Right*: Accumulated significance of the 133 GeV line with the add of new data. The green lines refer to the behaviour expected in the presence of a DM-related line while the red lines are the expectation for a statistical fluke [10].

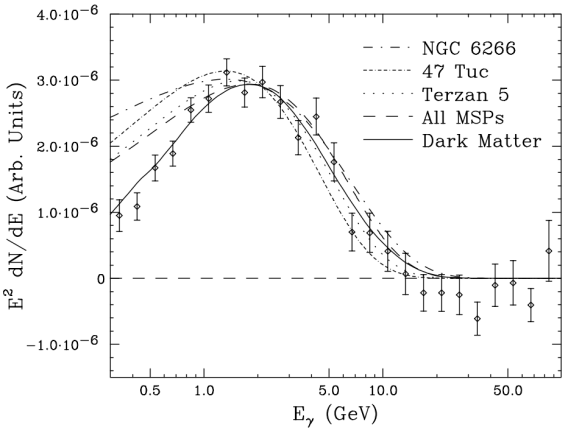

Figure 1.4: A comparison of the spectral shape of the gamma-ray excess (error bars) to that measured from a sum of all millisecond pulsars (MSPs) detected as individual point sources by Fermi and from a number of globular clusters (NGC 6266, 47 Tuc and Terzan 5), whose emission is believed to be dominated by MSPs.[11].

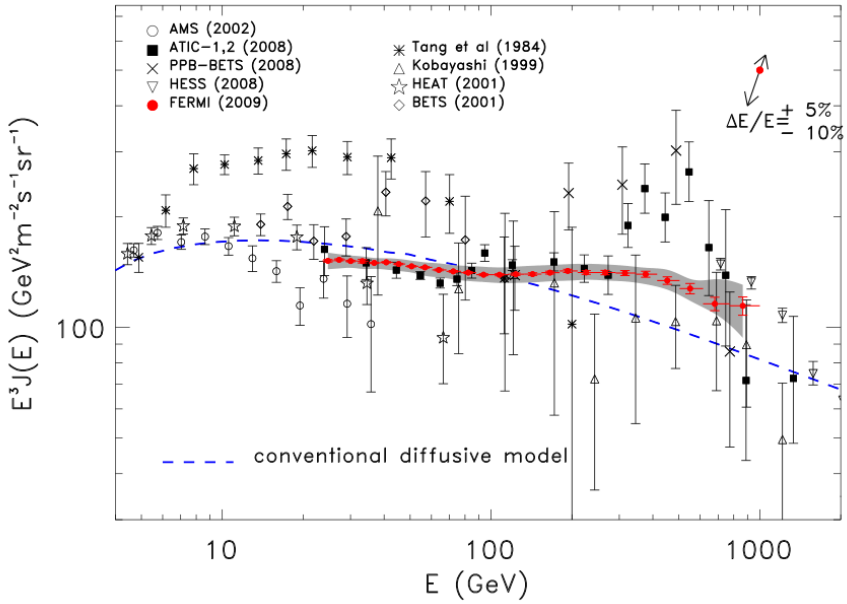

Figure 1.5: The Fermi LAT cosmic-ray electron spectrum (red filled circles). The ATIC data (black squares) and HESS data (triangle down) are also shown. Systematic errors are shown by the gray band. The two-headed arrow in the top-right corner of the figure gives size and direction of the rigid shift of the spectrum implied by a shift of $^{+5\%}_{-10\%}$ of the absolute energy, corresponding to the estimate of the uncertainty of the LAT energy scale. Other high-energy measurements and a conventional diffusive model ([16]) are shown. [17]

[25]. HESS is capable to measure the electrons energy from ∼340 GeV, missing only the rising of the ATIC-reported excess but not its bulk. The excess was however not present in the HESS spectrum.
HESS results were confirmed and extended to lower energies by Fermi [17]. The spectrum, shown in fig. 1.5, was computed between 20 GeV and 1 TeV at higher energy resolution with respect to HESS in the overlapping energy range. The spectrum is significantly flat on the whole energy range and no peak is present.
Both Fermi and HESS data, while not presenting any excess, still demonstrate a deviation from a conventional model explainable as DM contribution. The absence of the peak in the HESS and Fermi data seems to favour a nearby source explanation but does not exclude a DM one. This absence could help in the exclusion of some DM candidate, e.g. a 620 GeV Kaluza-Klein particle shown in fig. 1.6. In order to reconcile with the data, the DM candidate should have a high mass, $\mathcal{O}$(TeV). A DM annihilation or decay in a mixture of leptonic final states provides

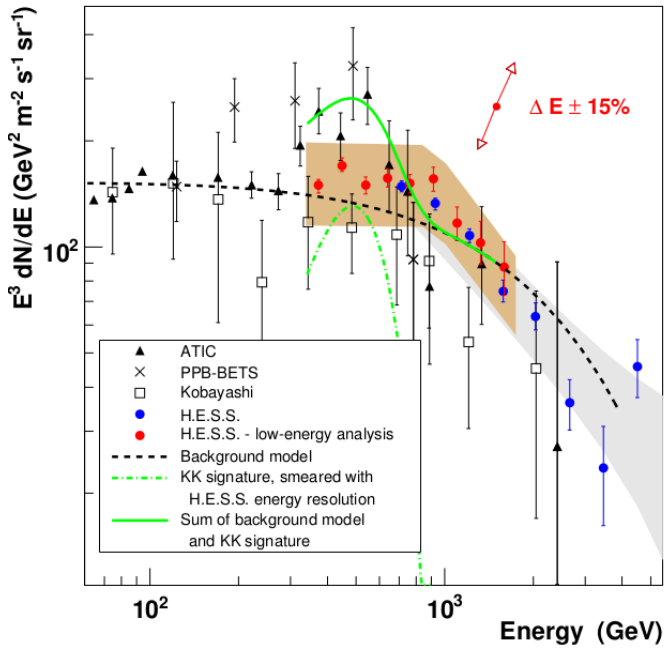

Figure 1.6: The energy spectrum $E^3 dN/dE$ of cosmic-ray electrons measured by H.E.S.S. (blue and red dots) and balloon experiments. Also shown are calculations for a Kaluza-Klein signature in the H.E.S.S. data with a mass of 620 GeV and a flux as determined from the ATIC data (dashed-dotted line), the background model fitted to low-energy ATIC and high-energy H.E.S.S. data (dashed line) and the sum of the two contributions (solid line). The shaded regions represent the approximate systematic error of H.E.S.S. [25].

a good fit to the data [27]. While modes involving the creation of a $\tau^+\tau^-$ pair provide the best fit, they imply a large γ flux from the π^0 results of the τ decay. The τ modes are compatible with the constraints given by γ observations only if the DM has a quasi-constant density profile (disfavoured by N-body simulations), the DM annihilation proceeds via extra long-lived ($> 10^{12}$s) particles or the DM decays. Annihilations in 4μ provides a good fit to the spectra (for M$\sim$ 3 TeV) and are marginally compatible with the constraints from γ observations. The fit to the electron spectrum and the gamma contribution of a 3 TeV particle in the two modes are shown in fig. 1.7. Other modes, like 4e, give poorer fit.
GAMMA-400 will be able to detect electrons up to 20 TeV with an unprecedented energy resolution. The large calorimeter will help to extend the measurements up to high energies with good statistic [28]. The results obtained so far from the different experiments will be confirmed or disproved with high precision and possible

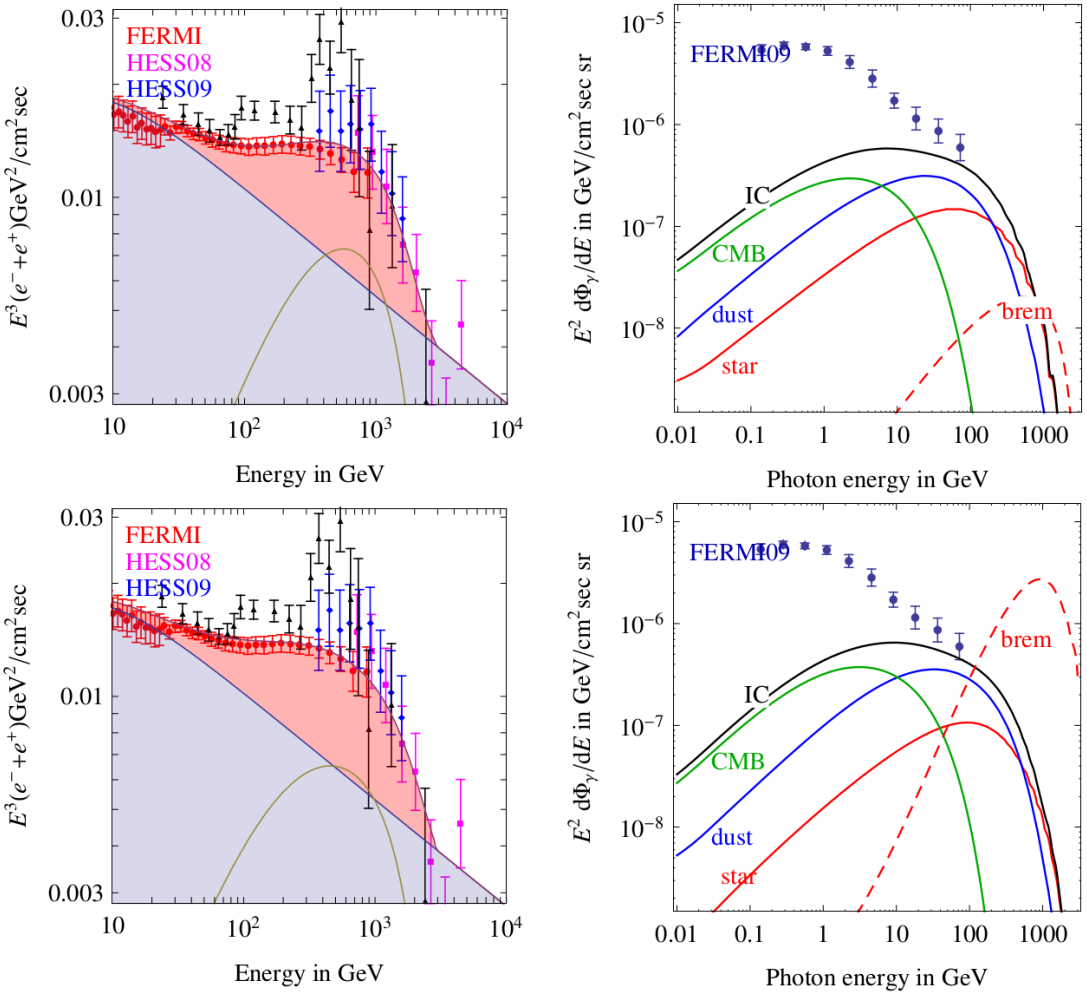

Figure 1.7: DM with M= 3TeV that annihilates in 4μ (*top*) or in $\tau^+\tau^-$ (*bottom*). The e^++e^- flux compared with the ATIC (black points), FERMI and HESS data are shown on the left while the contribution to the diffuse photon energy spectra produced by bremsstrahlung (dashed red curve) and Inverse Compton (black thick line) for the same annihilation channel is shown on the right. The components of the Inverse Compton contribution are also shown separately: from star-light (red), CMB (green) and dust (blue) [27].

feature in the all electron spectrum could be identified by GAMMA-400 thanks to its optimal energy resolution ($\sim 1\%$ for energies higher than 10 GeV).

1.2 Cosmic-ray origin and propagation

Cosmic rays are charged particles that reach Earth from outer space with an energy that can span more than 10 orders of magnitude. They are primarily composed by protons ($\sim 90\%$). Other significant components are α particles ($\sim$9%) and electrons ($\sim 1\%$). The remaining fraction is made up by other heavier ionized nuclei.
While convincing theories exist, many issues on the origin, acceleration and propagation of the cosmic rays lack of a definitive solution. Useful information can come not only from the direct study of the charged particles (sec. 1.2.1, 1.2.2, 1.2.3, 1.2.4), which are deflected by magnetic fields, but also from the detection of gamma rays (sec. 1.2.5, 1.2.6, 1.2.7), which permits to study directly their sources.

1.2.1 Knee origin

The cosmic-ray spectrum presents a clear change of slope at an energy of $\sim 10^{15} - 10^{16}$ eV, called knee, visible in fig. 1.8. At these energies the spectrum steepens passing from being $\propto E^{-2.7}$ to $\propto E^{-3.1}$. After the knee not only the slope, but also the composition seems to change, with a raise of the percentage of heavier nuclei[30]. A rigidity dependent acceleration mechanism provides a simple explanation to both the change in slope and composition. In this case, the knee would represent the end of the Galactic cosmic-ray spectrum, starting with protons at $\sim 5 \cdot 10^{15}$ eV and continuing with the heavier nuclei, exactly as observed [30]. The overall shape would be the result of the superposition of the cut-offs of different species.
In this context a Galactic population of sources is needed to accelerate the cosmic rays up to $\sim 10^{15}$ eV. The most promising of this kind of sources are Supernova Remnants (SNRs). SNRs have the right energy budget to accelerate particles to such high energies. In linear theory, if the magnetic field near the SNR is equal to the interstellar magnetic field, the maximum energy attainable for a particle of charge Z is $\sim Z \cdot 10^{14}$ [31]. While the limit is rigidity-dependent, the maximum energy is too low to account for the cosmic-ray spectra. It is therefore mandatory to take in consideration non-linear diffusive shock acceleration and an amplified magnetic field [32]. These hypotheses boost the efficiency of the acceleration mechanism. While this approach solves the energy problem and it has some observational confirmation, it presents a troublesome difference between the

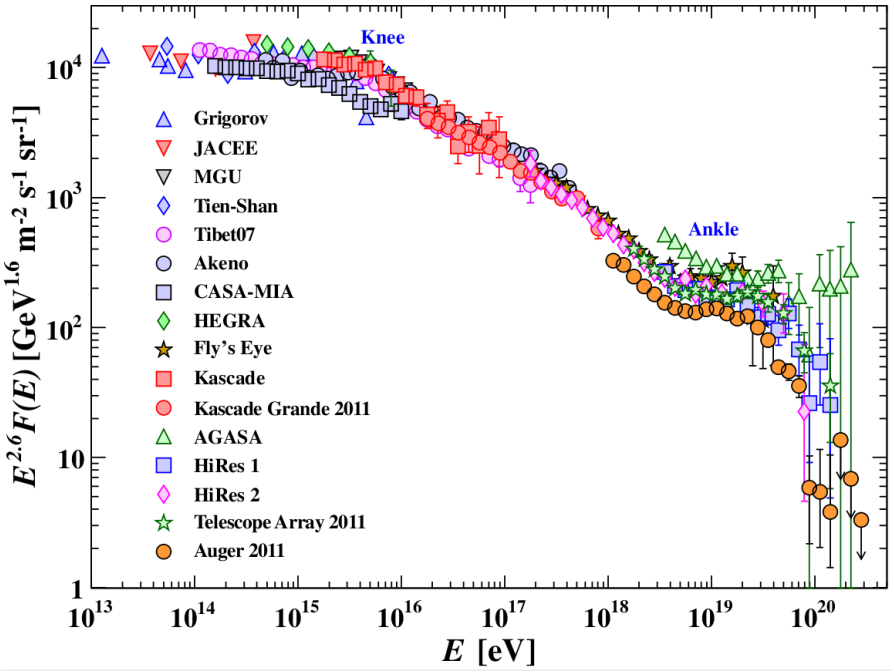

Figure 1.8: All particle cosmic-ray spectrum as a function of E (energy-per-nucleus) from air shower measurements. There is a change of slope at the knee ($\sim 5 \cdot 10^{15}$ eV) and at the ankle ($\sim 5 \cdot 10^{18}$ eV) [29].

calculated and the observed spectrum at the source. The spectrum inferred from γ observation of SNR, in a hadronic interpretation, is steeper than the calculated one, as more thoroughly discussed in sec. 1.2.5.
A theory for the knee origin, seen as a convolution of the spectrum of different isotopes, linked to the acceleration process, while compelling, is not yet proven. An alternative explanation of the knee relates it to the leakage of cosmic rays from the Galaxy. In this case the knee is expected to occur at lower energies for lighter nuclei due to the rigidity dependence of the Larmor radius of cosmic rays propagating in the galactic magnetic field [33].
GAMMA-400, being a space-borne experiment, will be able to study directly the knee, without any previous interaction of the particles with the atmosphere. Thanks to its great acceptance (> 3 m^{2}sr), high angular ($\sim 0.05°$ at 100 GeV) and energy ($\sim 35\%$) resolution and peculiar orbit, GAMMA-400 will combine gamma-ray (see sec. 1.2.5) and charged particles observations to try to resolve the remaining issues concerning the knee origin thanks to high-statistic observations without previous interaction in the atmosphere.

1.2.2 Electrons anisotropies

In their propagation in the Galactic magnetic field, electrons with energy higher than 10 GeV lose energy preferentially via inverse Compton and synchrotron[34]. The energy loss rate can be written as

$$-\frac{dE}{dt} = bE^2, \tag{1.1}$$

where E is the electron energy, and b depends on its mass, the magnetic field, the scattering cross section and the energy density of interstellar photons. Interstellar photons can be generated either from stellar radiation, re-emission radiation from dust grains or the CMB (Cosmic Microwave Background). The energy loss of TeV electrons from interactions with the CMB dominates over the other two components.
Since the energy loss rate is proportional to b, an electron loses almost all its energy after a time $T = 1/(bE)$. Accordingly, between the acceleration and the detection of an electron of energy E, a time no longer than $T = 1/(bE)$ must have passed. Higher energy electrons have a smaller lifetime than low energy ones. Kobayashi and collaborators [34] calculated $T = 2.5 \times 10^5 \mathrm{yr}/E(\mathrm{TeV})$ which lead to a possible diffusion distance for 1 TeV electrons of $\sim 0.6 - 0.9$kpc, depending on the diffusion coefficient. TeV electrons have to be accelerated in nearby sources, and these sources should leave a signature in the electron spectrum. Depending on the diffusion coefficient, the signature could be more or less evident. For high value of the diffusion coefficient, hence with a longer propagation of the electrons in the interstellar medium, the spectral shape and the peak flux of the sources should be flatter, as visible in fig. 1.9. The time of acceleration in Supernova Remnants gives an indication of the features of which sources would be visible. Features in the spectrum are not the only indication of a nearby sources. Observations can be made to search for anisotropies created by the same sources.
It is therefore possible, by studying the electron spectrum and searching for anisotropies, to obtain information on both the acceleration sites and the propagation of electrons in the interstellar medium. The detection of the feature in the spectrum, and thus a nearby population of cosmic-ray acceleration sites, can also provide an explanation for the excess in the electron spectrum at high energy (see sec. 1.1.2) without resorting to DM. The detection of an anisotropy in the arrival direction of the electrons can instead possibly discard altogether the hypothesis of a DM origin for the anomalous rising in the positron fraction [35].
GAMMA-400, thanks to its high energy ($\sim 1\%$ for energies higher than 10 GeV) and angular resolution ($\sim 0.02^\circ$ at 500 GeV) and its great acceptance (> 3 m^{2}sr), will be able to detect features in the all electron spectrum related to nearby sources and search for possible anisotropies in the arrival direction of high energy electrons.

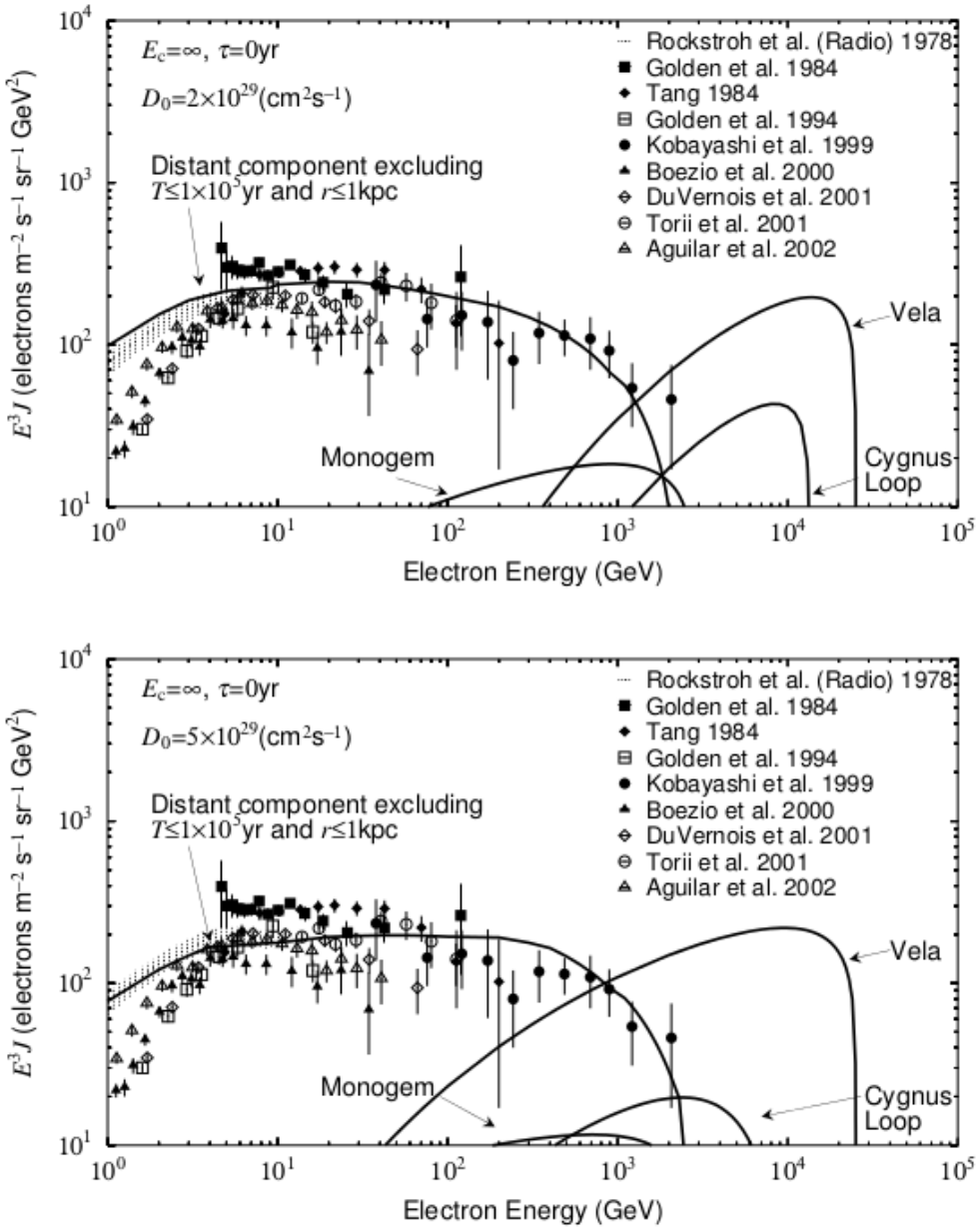

Figure 1.9: Calculated energy spectra of electrons without a cut-off of the injection spectrum for the prompt release after the explosion, compared with presently available data. The two graph differs for the diffusion coefficient $D = D_0(E/\mathrm{TeV})^{0.3}$ used in the calculation (*top*: $D_0 = 2 \times 10^{29}$ cm^2/s, *bottom*: $D_0 = 5 \times 10^{29}$ cm^2/s [34]

1.2.3 Cosmic-ray elemental spectra

For long it was believed that the cosmic-ray spectrum presents no structure before the knee and that it could be fit by a single power-law in this broad energy range. A first indication of the contrary came from the results by the balloon experiment CREAM (Cosmic-Ray Energetics And Mass, e.g. [37]) [38]. The measured spectra of both protons and helium nuclei were harder than what would be indicated by extrapolation of a single power-law fit of lower energy measurements. This first indication, with low statistical and systematic significance, has been later confirmed by PAMELA data [36]. The proton and helium fluxes measured by PAMELA and some other experiments are shown in fig. 1.10. Using the PAMELA data the hypothesis of a single power-law to describe the spectrum at energies lower than the knee is rejected with a confidence level greater than 95%. At few hundreds of GeV the proton and helium data exhibit a spectral hardening, as visible in fig. 1.10. The observed helium spectra is also significantly harder than the spectrum of protons. The proton-to-helium ratio flux (fig. 1.11) shows a continuous and smooth decrease well described by a power-law down to ~ 5 GV. The detection of a hardening in the cosmic-ray spectra around 200 GeV/n agrees with theoretical calculations on the cosmic-ray propagation [32]. A change in the propagation regime is foreseen due to the transition of a different scattering regime, resulting in the slope change in the spectrum. Another explanation is that the hardening indicates a different population of cosmic-ray sources [36]. One of these models, which considered novae and explosions in superbubbles as additional cosmic-ray sources, is found to be in agreement with the data, as shown in fig. 1.11.
While these mechanisms can explain the hardening in the spectra, they are not able to explain why the helium spectrum is harder than the protons spectrum. One of the available explanations is based on preferential injection of He in the acceleration mechanism.
The PAMELA results, although in agreement with the measurements by CREAM and the other high-energy experiments and the results expected by theoretical calculations, seems to be challenged by very preliminary AMS-02 measurements [39; 40].
GAMMA-400, thanks to a calorimeter with high acceptance (> 3 m^{2}sr) and energy resolution ($\sim 35\%$ for protons), will be able to study the cosmic-ray elemental spectra up to the knee in order to provide valuable information to understand the acceleration and subsequent propagation of cosmic rays in the Galaxy. In order to study also heavier nuclei, a charge identification system will be mounted on GAMMA-400, as described in sec. 3.2.5.

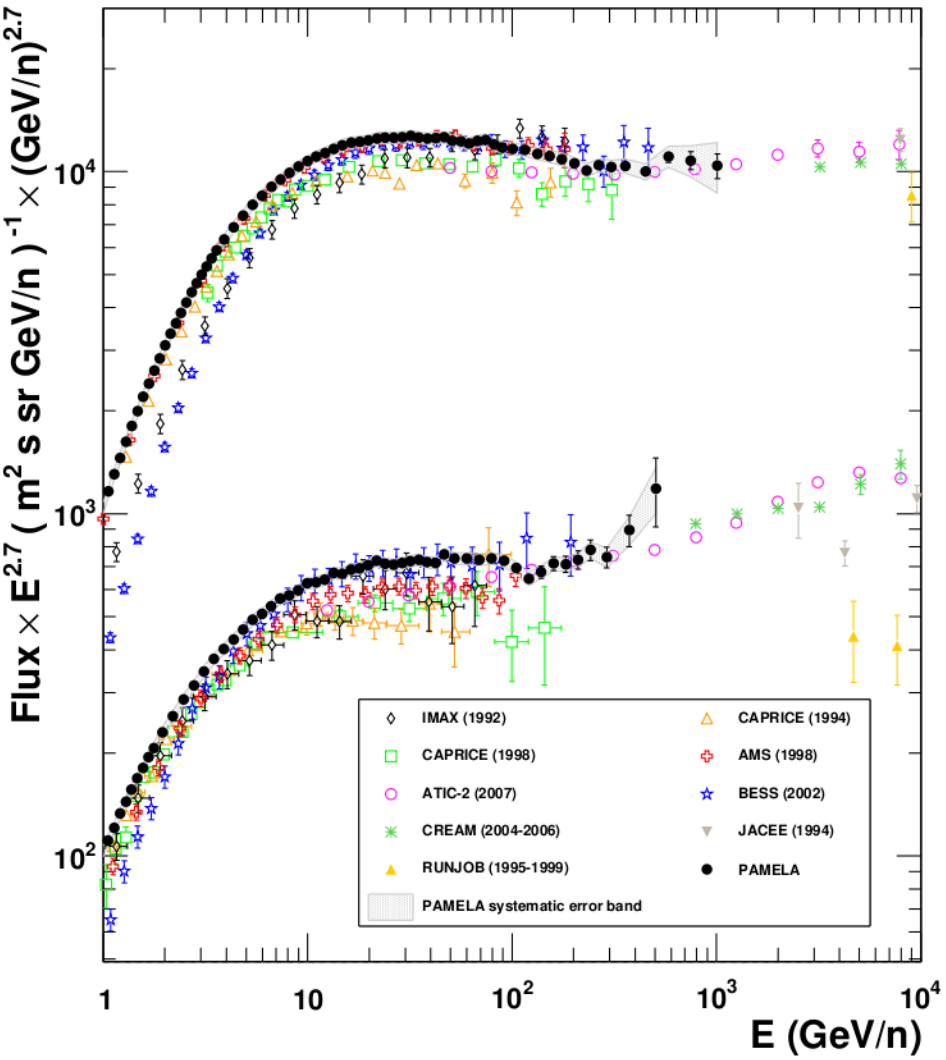

Figure 1.10: Proton and helium fluxes above 1 GeV/n measured by PAMELA and few others precedent experiments. All previous measurements but the results of AMS-01 (AMS (1998)) come from balloon-borne experiments. Error bars are statistical, the shaded area represents the estimated systematic uncertainties [36].

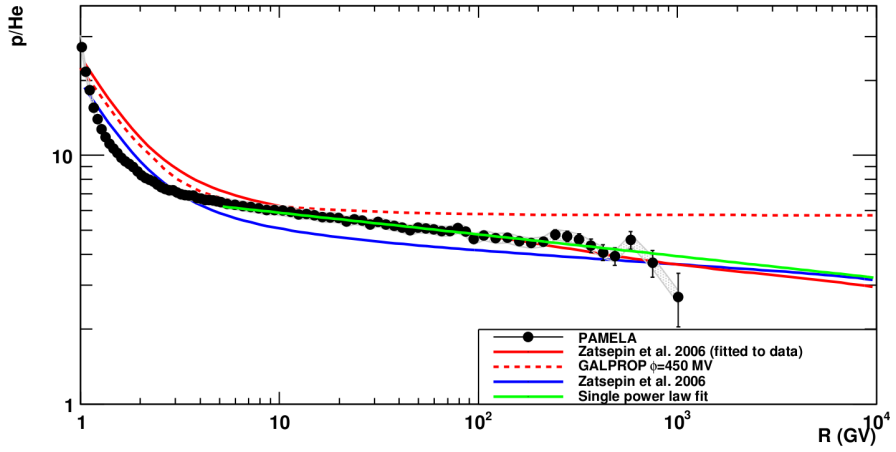

Figure 1.11: Ratio of the flux between proton and helium data of PAMELA vs. Rigidity. The shaded area represents the estimated systematic uncertainty. Lines show the fit using one single power law (describing the difference of the two spectral indices), GALPROP and one of the models taking in consideration different cosmic-ray sources [36].

1.2.4 Secondary nuclei

The relative element abundance of galactic and solar cosmic rays are pretty similar, apart from two groups of elements much more abundant in galactic cosmic rays: Li, Be, B and Sc, Ti, V, Cr, Mn. These are secondary elements, product of spallation, a process in which a primary cosmic ray, synthesized in stars, interact with matter forming as a result a different nucleus. Li, Be and B are a spallation product of Carbon and Oxygen, while Sc, Ti, V, Cr and Mn are produced by Iron. By studying the ratio between secondary and primary nuclei, such as the Boron-to-Carbon ratio (B/C), information on the amount of material traversed by the cosmic rays between injection and observation can be inferred. Similarly, looking at long-lived radioactive secondary isotopes can give insights on the confinement of the cosmic rays in the Galaxy. Information about the secondary production and propagation, as well as their dependence from energy or rigidity, can be deduced by comparing the energy spectra of different nuclei.
The latest results by PAMELA [41], as well as a compilation of previous results, are shown in fig. 1.12. The results are found to be in good agreement both between them and with a theoretical calculation made with a numerical calculation model (GALPROP [42]). Some discrepancies in the absolute fluxes are present at low energy but they can be reasonably ascribed to solar modulation.
Nuclei are not the only secondary component of cosmic rays. As discussed in sec.

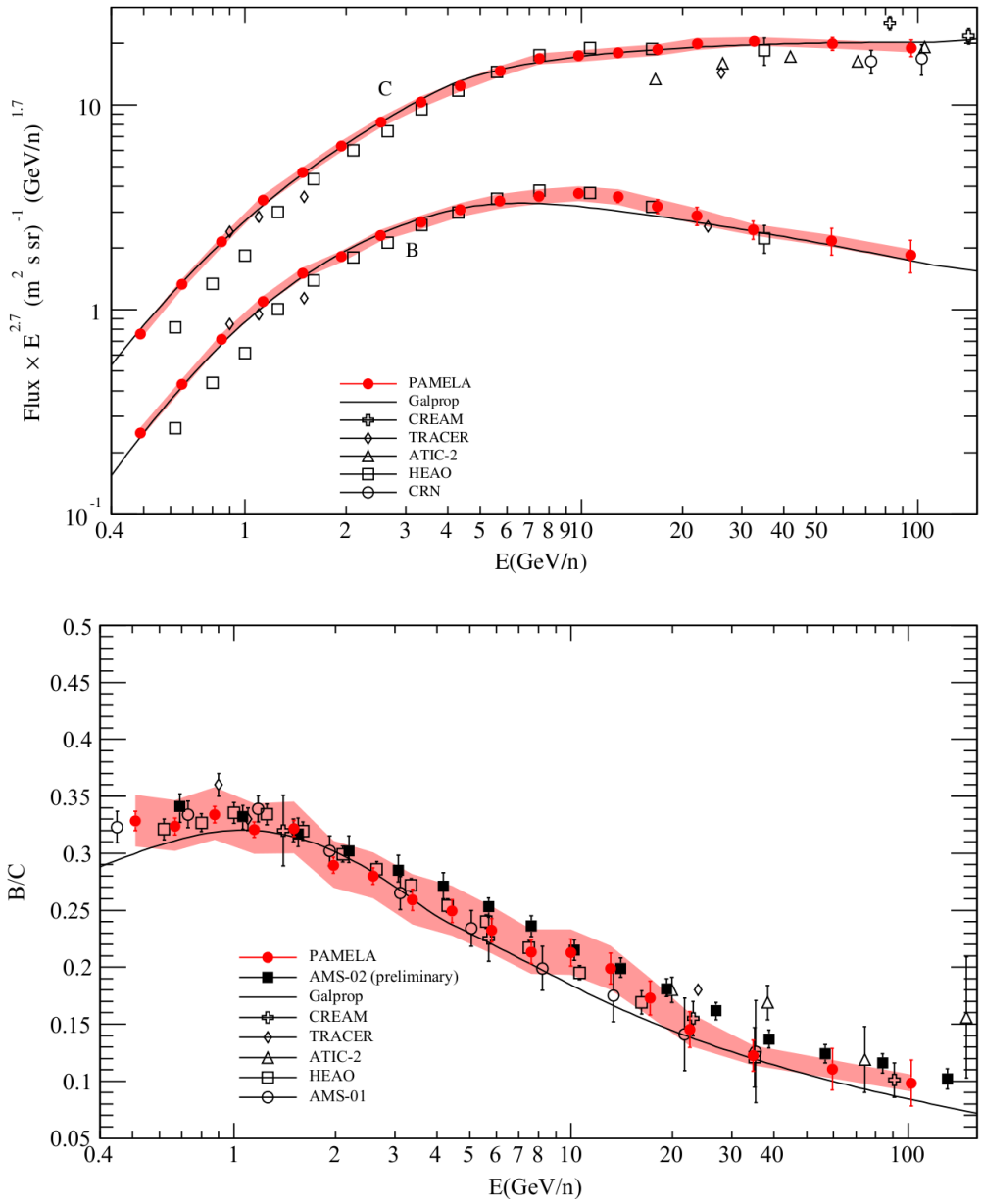

Figure 1.12: Absolute boron and carbon fluxes multiplied by $E^{2.7}$ (*top*) and B/C ratio as a function of kinetic energy per nucleon (*bottom*). The results are from: PAMELA, for which the shaded area represents systematic uncertainty, AMS-02, CREAM, TRACER, ATIC-2, HEAO, CRN and AMS-01. Also shown a theoretical calculation based on GALPROP [41].

1.1.2, the rise in the positron fraction has been ascribed to an additional primary component such as DM. The rise can also be explained by models with secondary production at the source [43]. The results on the B/C ratio can provide constraints to such models.
GAMMA-400, thanks to a high acceptance (> 3 m^{2}sr) and a good energy resolution ($\sim 40\%$), will be able to detect nuclei with good statistic up to high energies, providing an excellent measurements of the ratio secondary-to-primary nuclei.

1.2.5 Gamma-ray emission of Cosmic-ray sources

As previously stated in sec. 1.2.1, SNRs are believed to be the acceleration sites of cosmic rays. While for protons and nuclei a definitive proof is still lacking for all the types of SNRs, the acceleration of electrons in SNRs has been confirmed thanks to multiwavelength observations.
A signature of electrons acceleration is the presence of a non-thermal X-ray spectrum related to the synchrotron emission of the accelerated particles in the SNR magnetic field. The same population of electrons should also emits gamma rays through inverse Compton, with a morphology similar to the one observed in X-ray. Such a correlation between synchrotron and inverse Compton emission has been observed in several SNR, such as RX J1713.7-3946 [44], Cassiopeia A (Cas A) [45] and SN 1006 [46].
Cas A exhibits a broken power-law spectrum not well fitted by one or more thermal components. The multiwavelength spectrum of Cas A is shown on the bottom of figure 1.13. Among the non-thermal processes taken in consideration in [45] as a possible explanation of the Cas A spectrum, there are non-thermal bremsstrahlung, inverse Compton scattering and synchrotron emission. The X-ray tails of Cas A are too steep to be compatible with a non-thermal bremsstrahlung emission process. Inverse Compton emission could describe well the shape of the tail but the estimated flux in this case would be 10^4 times smaller than the observed one. A pulsar could in theory produce nonthermal X-ray continua, but no pulsation were detected in X-ray, radio or optical, nor a bright X-ray feature is present near the center of the remnant. Synchrotron emission can instead explain both the shape and the flux. If the synchrotron spectrum extends to energies of at least 120 keV and the magnetic field in Cas A is 1 mG, then the accelerated electron spectrum extends up to at least 40 TeV [45].
X-ray observations reveal a synchrotron emission also in RX J1713.7-3946. This X-ray emission is found to have a remarkable correlation with the TeV gamma-ray emission detected by H.E.S.S. [44], as visible in fig. 1.13. Such a correlation could be also explained by hadronic models in which the electrons are secondary particles, product of the decay of pions created in the interaction of the protons with

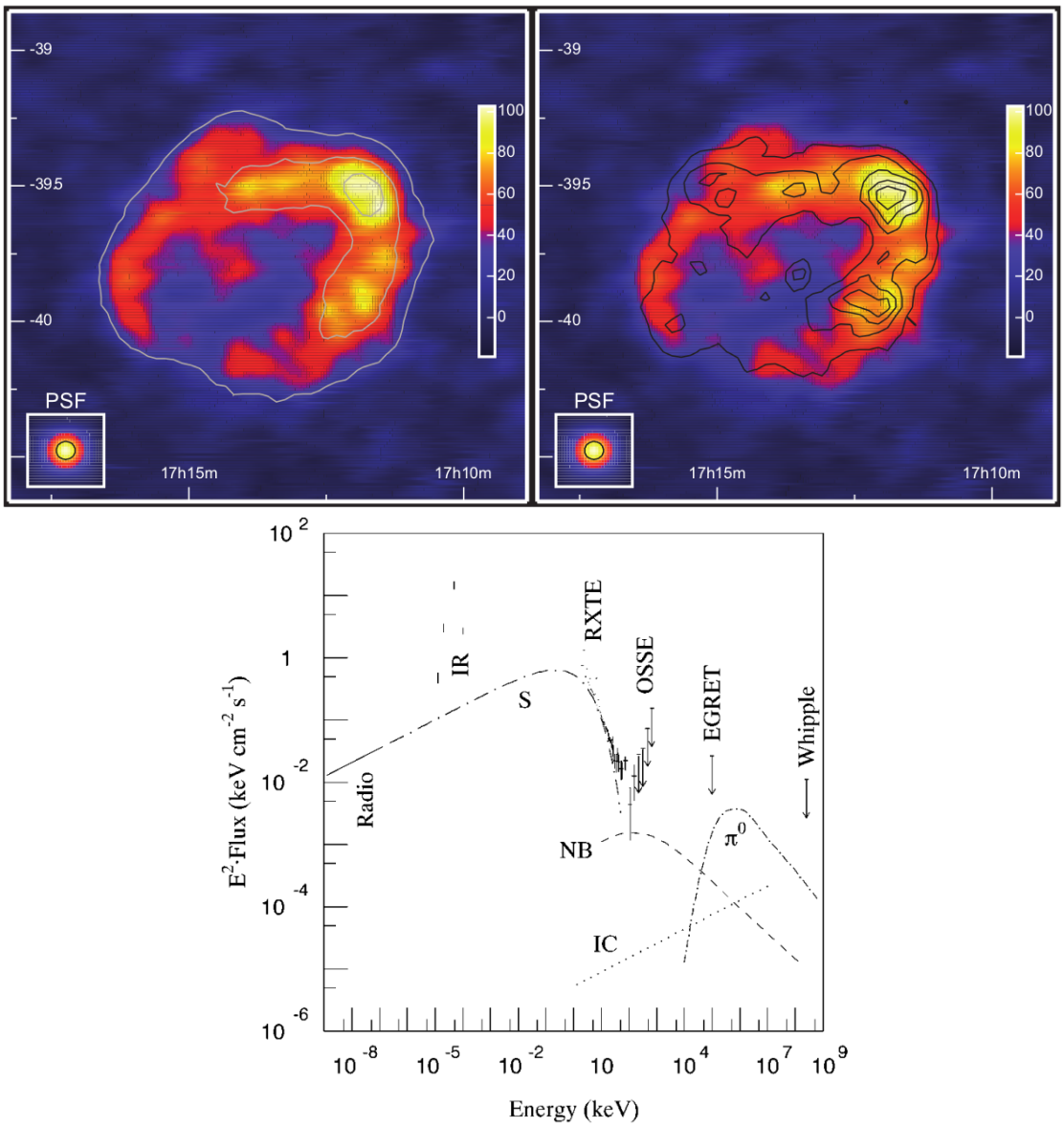

Figure 1.13: *Top*: Two versions of RX J1713.7-3946 as seen by HESS. *Left* the overlaid light-gray contours illustrate the significance of the different features. The levels are at 8, 18, and 24 σ. *Right* X-ray contours from ASCA data are drawn as black lines for comparison [44]. *Bottom*: The multiwavelength photon spectrum of Cas A. The four broken lines are estimates of the fluxes from synchrotron radiation (S), nonthermal bremsstrahlung (NB), inverse Compton scattering of the cosmic microwave background (IC), and the decay of neutral pions (π^0) [45].

the surrounding medium. Hadronic models can not explain the emission in this case since the X-ray flux exceeds the gamma-ray flux, contrary to what happens in hadronic models. The gamma-ray spectrum of RX J1713.7-3946 has been measured up to 30 TeV confirming the existence of primary radiating particles with energy of at least 100 TeV [44].

A signature of the protons acceleration in SNR is the presence in the gamma-ray spectrum of a feature related to pion decay. The protons, accelerated by the SNR, would interact with the surrounding gas producing both neutral and charged pions, the first of which would decay in gamma rays. Recently such a signature was found in the SNRs W44 [48] and IC443 [47]. Both these SNRs are middle-aged ($\mathcal{O}(10^4)$ yr) and consequently they are not expect to accelerate cosmic rays very efficiently [32]. The behaviour of these two SNRs reflects this expectation: both gamma-ray spectra can be described by a broken power-law (see fig. 1.14). At low energies the gamma-ray data of W44 well fit a proton distribution index of ~ 2.2 (2.36 ± 0.05 in [47], 2.2 ± 0.1 in [49]). This result in the energy space implies an index in the momentum space similar (2.4 - 2.5) to the cosmic-ray spectrum one before the knee (2.5). Similar results are obtained also for IC443.

Differently from younger SNRs, W44 and IC443 exhibit a steepening in the spectrum at higher energies. For W44 this steepening appears for momenta higher than 22 ± 8 GeVc^{-1} while for IC443 for momenta higher than 239 ± 74 GeVc^{-1} [47]. The resulting steeper spectrum at higher energies (proton distribution index of 3.1 ± 0.1 for IC443 [47] and 3.2 ± 0.1 in [49] or 3.5 ± 0.3 in [47]), shown in the top of fig. 1.15, is not compatible with the interstellar cosmic-ray index.

It should be emphasize that a leptonic-only model fails to describe the emission of both these SNRs. Electrons distributions, constrained by multiwavelength observations, fail to reproduce both the shape and brightness of the observed spectrum [47; 49].

The brightness of W44 and IC443 is not due to a high flux of relativistic hadrons, but rather to a high target density for nuclear collisions given by the interaction with a molecular cloud. A proof for efficient hadron acceleration in SNRs has to be found in young objects. The problem in the observation of young SNRs is that their emission is harder to describe and thus conclusions are more difficult to be drawn. As an example, as mentioned before, early observation of RX J1713.7-3946 suggested a hadronic emission inside the remnant. Only with the refined observation in X-ray and the absence of a π^0 relate component in gamma rays, the interpretation changed radically, as explained in the previous paragraph. Another example is Tycho, a young SNR believed to accelerate protons up to energy of the order of 500 TeV. In this case the difficulty in evaluating the galactic background, results in high error band in the spectrum, as shown in the bottom of fig. 1.15

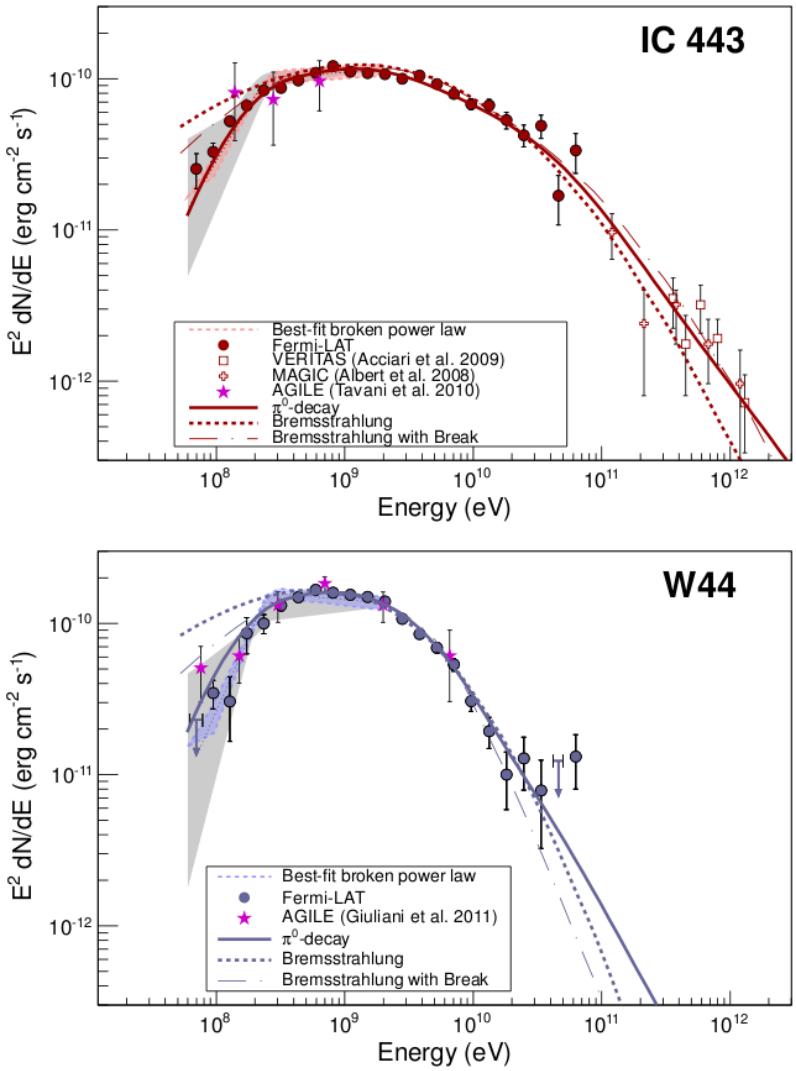

Figure 1.14: Gamma-ray spectra of IC443 (*top*) and W44 (*bottom*) as measured with the Fermi-LAT. Color-shaded areas bound by dashed lines denote the best-fit broadband smooth broken power law (60 MeV to 2 GeV), gray-shaded bands show systematic errors below 2 GeV due mainly to imperfect modeling of the galactic diffuse emission. At the high- energy end, TeV spectral data points for IC443 from MAGIC and VERITAS are shown. Also shown the best-fit pion-decay gamma-ray spectra (solid lines), the best-fit bremsstrahlung spectra (dashed lines) and the best-fit bremsstrahlung spectra when including an ad hoc low-energy break at 300 MeV c^{-1} in the electron spectrum (dash-dotted lines). These fits were done to the Fermi LAT data alone (not taking the TeV data points into account). Magenta stars denote measurements from the AGILE satellite for these two SNRs [47].

[50]. Additional observations of younger SNRs using a multiwavelength approach are then necessary to provide a definitive confirmation of hadron acceleration in SNRs.

GAMMA-400, thanks to its improved energy resolution ($\sim 1\%$ for energies higher than 10 GeV) and high angular resolution ($\sim 0.05^\circ$ at 100 GeV), will be able to provide information on the shape of the high energy spectrum of SNRs. These information, connected also with multiwavelength observations, will help in the search of features related to hadron acceleration, especially in the poor populated region between the Fermi data and the data from on-ground Cherenkov telescopes. This improvement will be particularly helpful for the observation of young SNRs, difficult to model.

1.2.6 Diffuse emission

The high energy gamma-ray diffuse emission is dominated by gamma rays produced by the interaction of cosmic rays with the Galactic gas and radiation fields, hence the name Diffuse Galactic Emission (DGE). Diffuse gamma rays trace the cosmic rays density and the interstellar medium column density in the Galaxy [53]. A much fainter diffuse component is also present: the Extragalactic Gamma-ray Background (EGB) [54], whose multiwavelength spectrum is shown on top of fig. 1.16. The EGB has an isotropic distribution in the sky and it is believed to be the result of the superposition of contributions from unresolved extragalactic sources and truly diffuse emission processes, but the bulk of its radiation is of unknown origin. Among the sources that contribute to the EGB there are: radiations from unresolved extragalactic sources, starburst galaxies, gamma-ray bursts and truly diffuse processes such as signatures of large-scale structure formation, emission produced by ultra high energy cosmic rays with relic photons of the CMB or DM contribution. However, also diffuse gamma-ray emission from the interaction between the cosmic rays and a Galactic halo, solar photons or solar system bodies, can contribute to this component. Unresolved extragalactic sources represent $\sim 16\%$ of the emission (see bottom of fig. 1.16), starburst and normal star-forming galaxies a $\sim$10% each due to cosmic-ray-interstellar gas interaction [52]. Blazars, active galactic nuclei with a relativistic jet pointing close to our line-of-sight, while could in theory explain most of the background, are detected in too small a number.

Achieving a good knowledge of the diffuse emission is both important and difficult, especially for the study of cosmic-ray propagation and search for DM signals. Only by being able to subtract the contribution from the diffuse emission it is possible to identify new sources (see also sec. 1.2.7) and estimate the contribution from DM annihilation and decay and cosmic-ray interaction with radiation fields and gas.

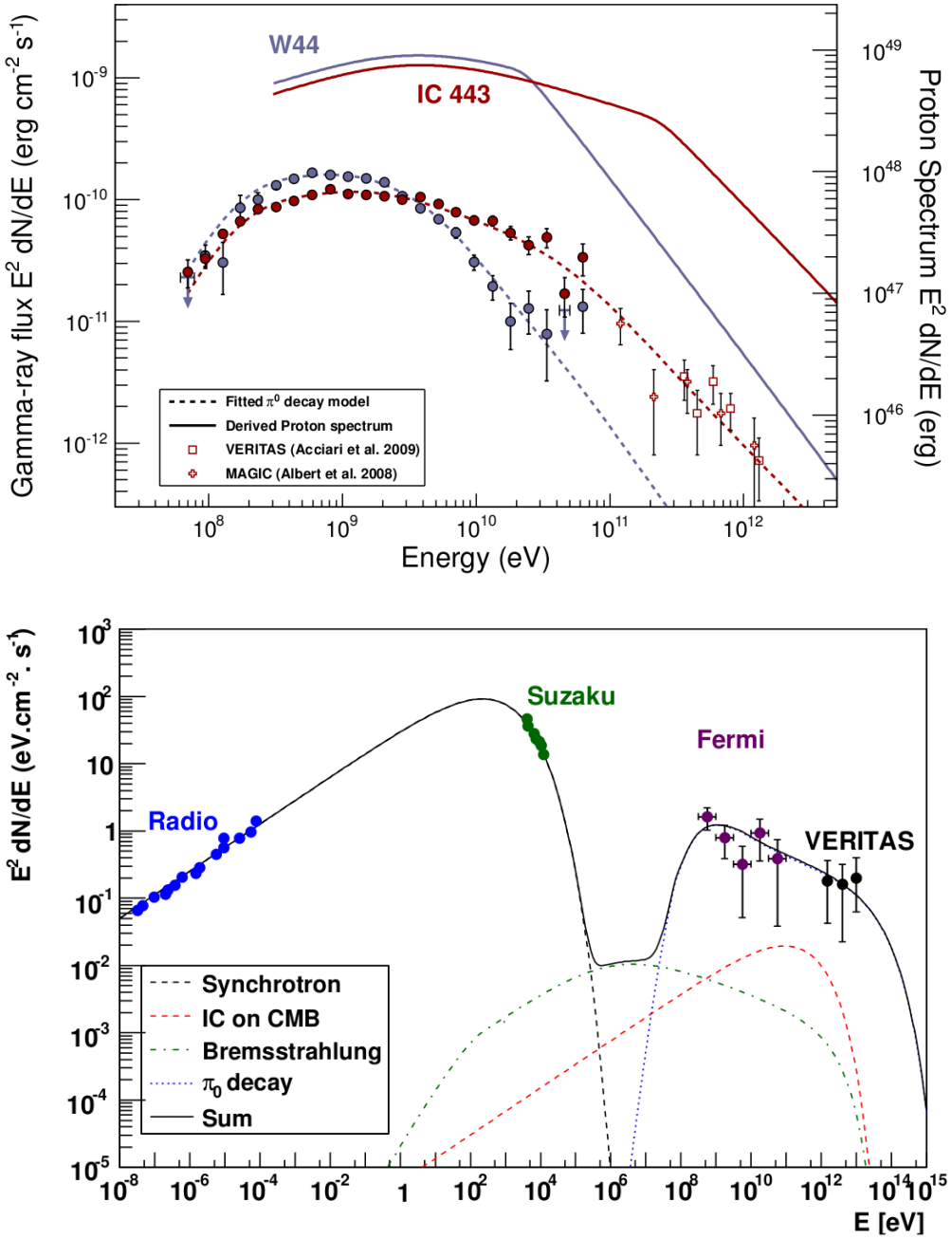

Figure 1.15: *Top*: Proton (solid lines) and gamma-ray spectra determined for IC443 and W44. Also shown are the broadband spectral flux points and TeV spectral data for IC443 from MAGIC and VERITAS [47]. *Bottom - right*: Broadband spectral energy distribution of Tycho's SNR in the hadronic interpretation [50].

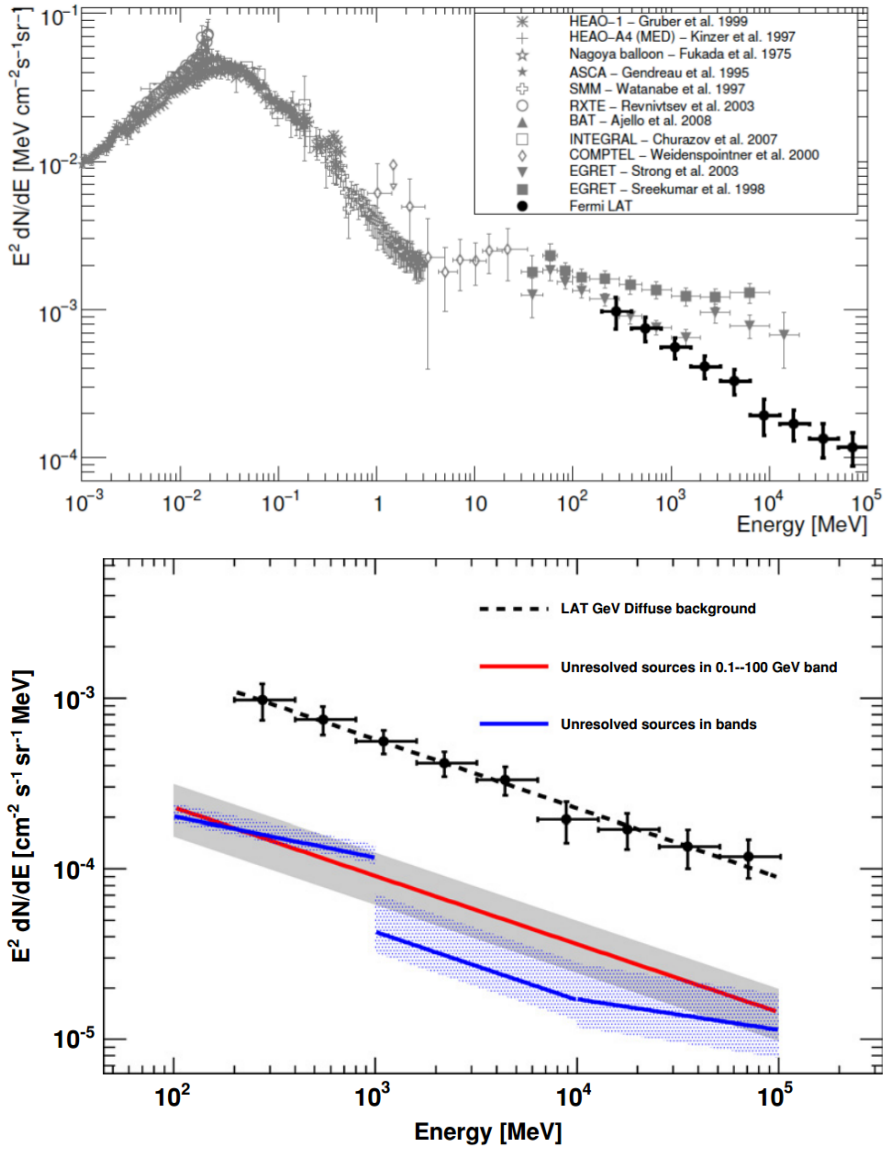

Figure 1.16: *Top*: Spectral energy distribution of the extragalactic diffuse emission between 1 keV and 100 GeV measured by various instruments [51]. *Bottom*: Contribution of point sources to the diffuse GeV background from whole band study (red solid line) and individual energy bands study (blue solid lines). The bands (gray solid and hatched blue) show the total (statistical plus systematic) uncertainty [52].

An extragalactic origin for such a component is not clear. GAMMA-400, with the high resolution it will be able to provide, will study the diffuse emission in order to understand its nature, searching for distinct spectral features and identify some of the unresolved sources in order to better calculate the different contributions to the emission. Observations from GAMMA-400 will be complementary to the results of HAWC (High Altitude Water Cherenkov Detector [55]) to provide a complete description of the gamma-ray diffuse emission in the GeV-TeV energy range.

1.2.7 Fermi bubbles

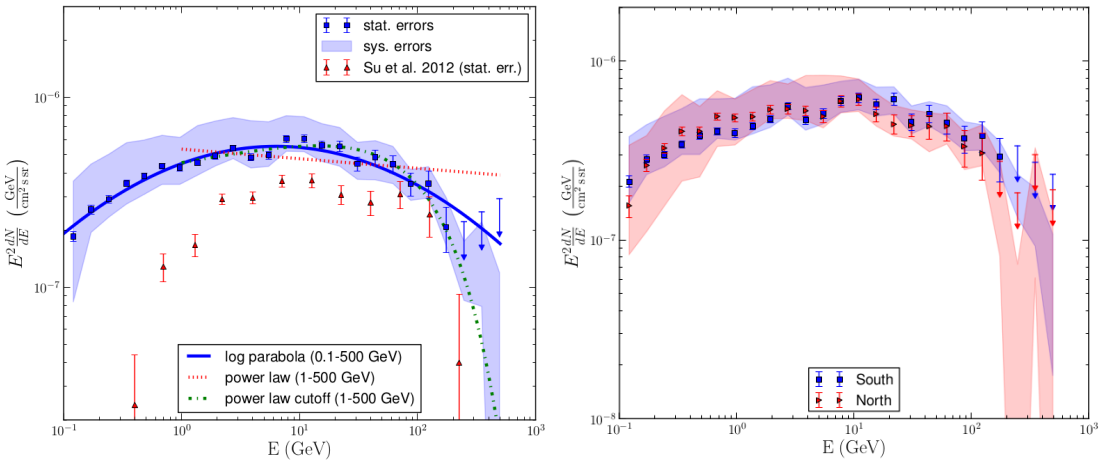

Figure 1.17: *Left:* Combined bubble spectrum compared with previous results for $|b| > 20°$.The curves show the fits to the points using a log parabola (solid blue line), a simple power-law (dotted red line) and a power-law with an exponential cut-off (dash-dotted green line) [56]. *Right:* Spectra of the two bubbles. The bands represent different derivations of the Galactic foreground and the definitions of the template of the bubbles [56]

A good knowledge of the diffuse emission and of the different contributions to it is what lead to the discovery of the Fermi bubbles [57]. The Fermi bubbles are two large gamma-ray bubbles, extending 50° above and below the Galactic Center (GC) and spanning ∼40° in longitude.
Indications of excess near the GC were already found in other experiments at different wavelengths. A biconical X-ray structure around the GC, later interpreted as a superwind bubble, was found in the ROSAT All-Sky Survey at 1.5 keV [58]. A so-called GC lobe, a limb-brightened bipolar structure, was found by the combination of the Midcourse Space Experiment and IRAS data [59]. Both

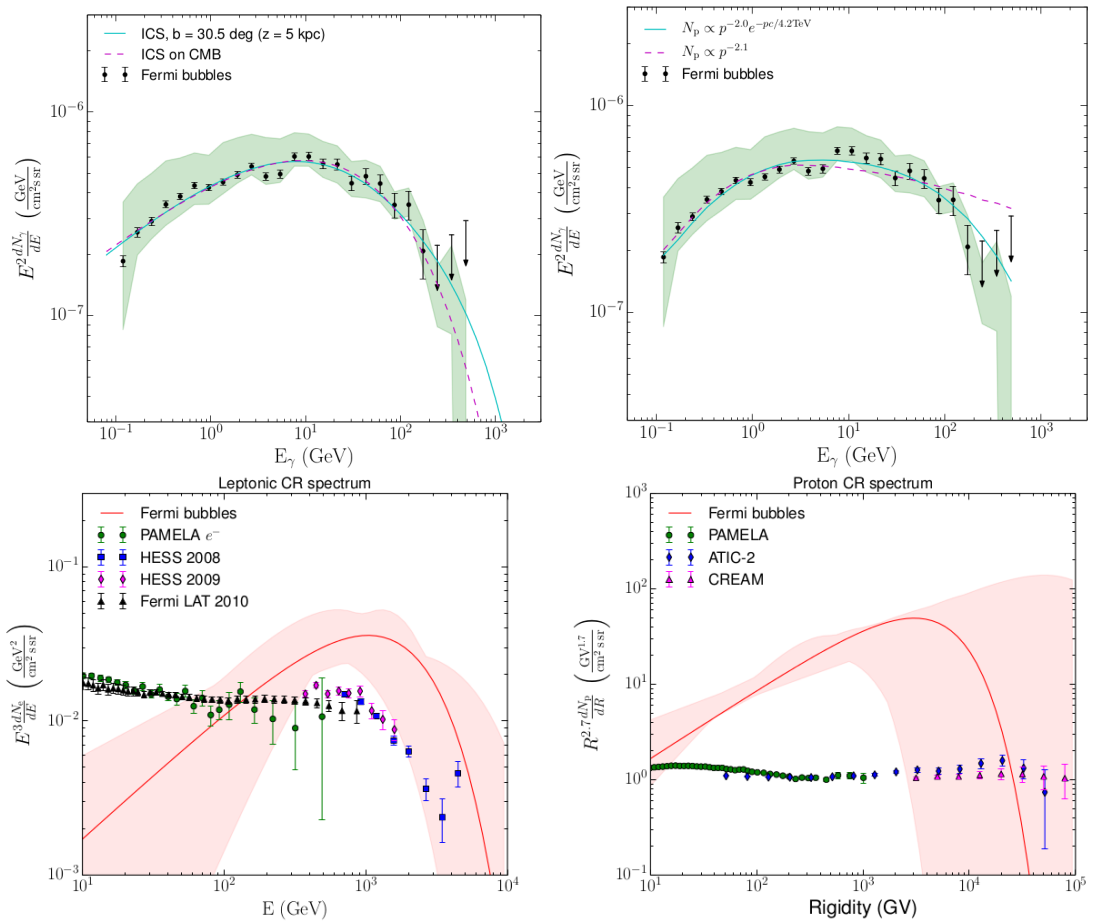

Figure 1.18: *Top*: Spectrum of the bubbles with a fit corresponding to the inverse Compton model (*left*) and the hadronic model including inverse Compton emission from secondary leptons assuming a 2μG magnetic field (*right*). Taking in consideration (*left*) also the inverse Compton on CMB photons changes the index from 2.2 to 2.3 and the cut-off energy from 1.25 TeV to 2.0 TeV. On the *right* the results of a fit with a simple power-law and a power-law with an exponential cut-off are shown [56]. *Bottom*: Comparison of leptonic cosmic-ray spectra in the inverse Compton model of the bubbles to the local cosmic-ray spectra (*left*) and the proton cosmic-ray spectra in the hadronic model compared to the local proton cosmic-ray spectrum. In both cases the band represents different fit to the gamma-ray spectra of the bubble using different models for the foreground and definitions for the bubbles template. The plots start at 10 GeV either because this is the energy range relevant for the production of gamma rays inside the bubbles and because at lower energy the spectra are affected by solar modulation [56].

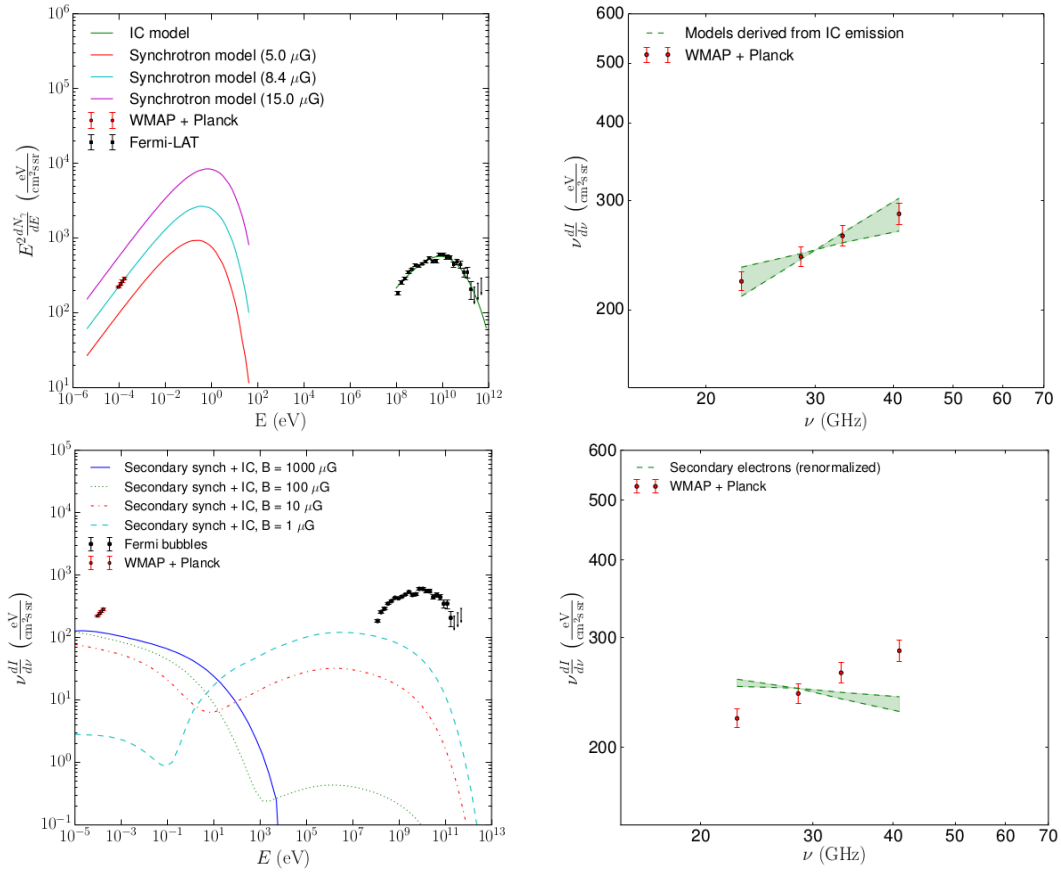

Figure 1.19: *Top - left*: Inverse Compton and synchrotron radiation from the same population of electrons. The electron energy density is derived by fitting the inverse Compton model to the gamma-ray data. Synchrotron emission from the same electron population is used to fit the WMAP and Planck data by optimizing the magnetic field value [56]. *Top - right*: Microwave haze spectrum compared to the synchrotron emission from electrons in the inverse Compton model. The green band shows systematic uncertainties related to systematic uncertainties in the gamma-ray spectrum of the bubbles [56]. *Bottom - left*: Synchrotron radiation produced by secondary leptons in the hadronic model emission in comparison with the microwave haze [56]. *Bottom - right*: Same as *top - right* but using synchrotron emission from secondary leptons in the hadronic model [56]

these structures are compatible with an energy injection of $\sim 10^{54} - 10^{55}$ erg and an estimated age of $\sim 10^6 - 10^7$ years. The Wilkinson Microwave Anisotropy Probe (WMAP [60]), after the subtraction of the contributions of known emission mechanisms, found, at tens of GHz, a microwave residual excess with spherical morphology about $\sim$4 kpc in radius towards the GC [61]. This haze presents a spectrum harder than the typical synchrotron but softer than free-free. The emission has been interpreted as due to synchrotron emission of a hard spectrum of cosmic-ray electrons. More recently, Planck [62] confirmed these results indicating an electron population with a spectrum $dN/dE \propto E^{-2.1}$ as the responsible of the emission [63]. However the haze polarization, predicted for this kind of emission, was not observed by WMAP, indicating either a highly tangled magnetic field or an alternative emission mechanism. In the case that the emission is truly related to synchrotron, the hardness of the associated electron spectrum and the extended nature of the emission make unlikely a SNR origin for the electrons, implying a different acceleration mechanism in the GC [57].
The Fermi bubbles were firstly revealed by subtracting to the Fermi-LAT all sky gamma-ray map the Fermi diffuse Galactic model [57]. The Fermi diffuse Galactic model is a comprehensive model of Galactic gamma-ray emission from π^0 decay produced by collisions of cosmic-ray with the interstellar medium and it serves as a background estimate from point source estimate. Similar results were obtained by subtracting several templates: a dust map to trace the dominant π^0 emission, a simple model of the disk and a template for the Loop I, a faint structure extending up to $b \sim 80°$ with l ranging from 0° to 40°. The bubbles are found to have a flat intensity for all of their extension, showing no significant variation of their spectrum across them. A comparison of the spectrum of the northern and southern bubbles is shown on the right of fig. 1.17. Their spectrum, shown on the left of fig. 1.17, is well described by either a log parabola or a power law with an index of 1.9 ± 0.2 and an exponential cut-off at 110 ± 50 GeV [56]. The simple power law hypothesis is excluded with a 7σ significance. The total gamma-ray luminosity of the bubbles is $\sim 4.4 \cdot 10^{37}$ erg·s^{-1}.
To explain the formation of the bubbles many models were proposed but neither of them is able to fully describe the complexity of the bubble morphology and emission. Some of these models predict: a jet emission from the central black hole [64], a spherical outflow from the black hole [65], a wind from supernova explosions [66] or a sequence of shocks from several accretion events onto the black hole [67]. The gamma-ray emission can be described as the result of the collisions between cosmic-ray protons with the diffuse gas [66] or as inverse Compton scattering of high energy electrons on radiation fields [57].
The inverse Compton model of the bubbles foresees an electron spectrum described

by a power law with an exponential cut-off $\propto E^{-n}e^{E/E_{cut}}$ [56]. The best fit parameters are $n \sim 2.17$ and $E_{cut} \sim 1.25$ TeV. The corresponding gamma-ray spectrum is shown on the top left of fig. 1.18. In this model the microwave haze can be produced by the same electron population by synchrotron emission, although a second population of electron can not be excluded. The best value for the magnetic field, derived by fit of the single electron population case, is $B \sim 8.4$ μG. A multiwavelength of the haze and the bubbles in the case of the inverse Compton is shown on the top of fig 1.19.
The hadronic model of the bubbles, taking in consideration only protons as responsible for the emission, can be described by a momentum-dependent spectrum in the form of a power law with an exponential cut-off [56]. Being p the momentum, the spectrum can be described as: $dn(p)/dp \propto p^{-n}e^{-pc/E_{cut}}$. The fitted values of the parameters are: $n \sim 2.13$ and $E_{cut} \sim 14$ TeV. The proton spectrum inside the bubbles must therefore be harder than the spectrum of cosmic-ray protons in the Galactic plane (see bottom of fig. 1.18 and sec. 1.2.3). This difference can be explained in terms of the energy-dependent escape time [66]. Supposing the proton injection spectrum, $\propto E^{-2.0-2.2}$, to be the same everywhere in the Galaxy, protons would escape from the Galactic plane before interaction. Instead, inside the bubbles, the protons would interact before escaping, remaining trapped inside the bubbles for several Gyr. Protons interactions inside the bubbles lead to the production not only of gamma rays but also electrons, positrons and neutrinos. Electrons produce synchrotron radiation but with a spectrum too soft and an intensity not high enough to account for the microwave haze, as shown on the bottom of fig. 1.19. Including emission from secondary leptons can improve the fit of the hadronic model (see top right of fig. 1.18) but, comparing the χ^2 of the fit of the two models, the inverse Compton model is found to better describe the bubbles spectrum. However, being the χ^2 of the two models compatible in some cases, it is still impossible to discriminate between hadronic and inverse Compton models.
The data on the Fermi bubbles in the gamma-ray band are not sufficient to draw a definitive conclusion on both their origin and emission mechanism. GAMMA-400 will be able to study the bubbles with an improved energy resolution ($\sim 1\%$ for energies higher than 10 GeV), closer to the Galactic center at high energies, thanks to the better angular resolution ($\sim 0.05^\circ$ at 100 GeV).

1.3 Time variability of the Gamma-ray sky

GAMMA-400 will be able to study also the transients in the gamma-ray sky. In this section temporally and spectrally variable emission from different sources

will be presented ordered as a function of the duration of the emission: flare from active galactic nuclei (AGN) will be presented in sec. 1.3.1, flares in pulsar wind nebulae (PWN) in sec. 1.3.2 and gamma-ray bursts (GRB) in sec. 1.3.3.
The time response of GAMMA-400 is still to be thoroughly analysed. Nonetheless, thanks to a pointing strategy without Earth occultation and the large field of view ensured by the calorimeter (see also sec. 4.2), GAMMA-400 could be able to study transients and trigger observations for other satellites and ground-based telescopes.

1.3.1 Active Galactic Nuclei Flares

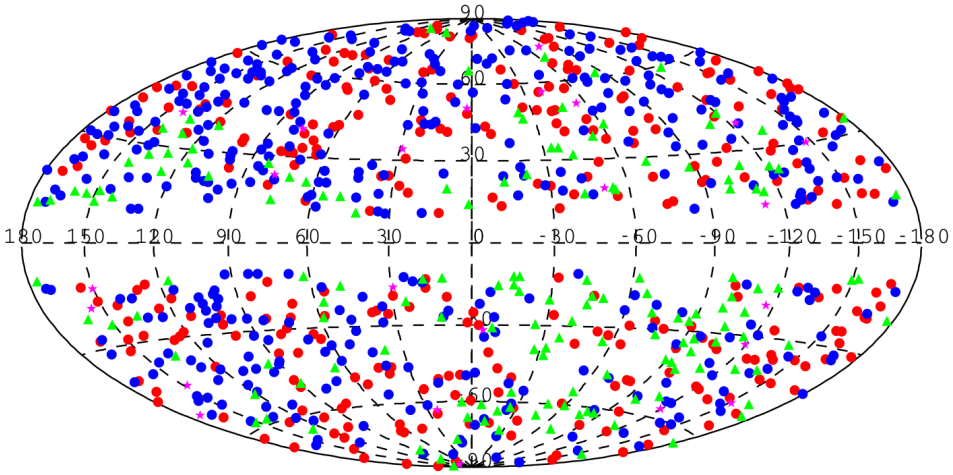

Figure 1.20: AGN locations in the sky. Red: FSRQs, blue: BL Lac objects, magenta: non-blazar AGN, green: AGN of unknown type [68].

Active Galactic Nuclei (AGN), whose gamma-ray map as seen by Fermi is shown in fig. 1.20, are galaxies that harbour an accreting supermassive black hole with a mass between 10^6 and 10^{10} solar masses [69]. Depending on the angle between the jet emission and our line of sight, AGN are classified using different names. This section will focus on blazars, AGN with viewing angles $< 10°$, for which the relativistically beamed non-thermal continuum from the jet dominates the emission, and that constitutes the larger fraction ($> 95\%$) of the AGNs visible in the gamma-ray energy band. BL Lac objects are a sub-class of blazars either without detected emission lines or with lines with a rest frame equivalent width smaller than 5Å. For slightly larger viewing angles the AGN can be seen as a Flat Spectrum Radio Quasar (FSRQs).

More than 50% of the observed AGN are found to be variable. Amplitude variations are larger for FSRQ and low/intermediate synchrotron frequency peaked

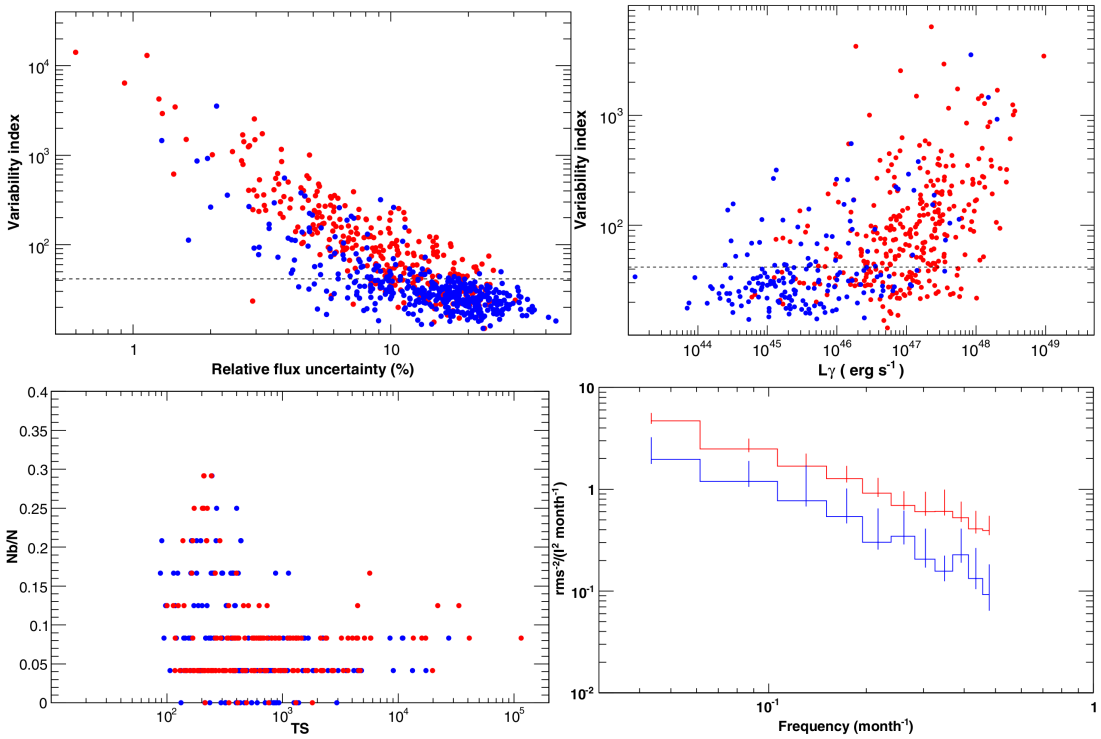

Figure 1.21: *Top*: Variability index vs relative flux uncertainty (*left*) and gamma-ray luminosity (*right*) for FSQRs (red) and BL Lac objects (blue). The dashed line corresponds to the 99% confidence level for a source to be variable [68]. *Bottom - left*: Duty cycle vs. TS (Test Statistic, a ratio between the maximum likelihood value for a model without or with an additional source. Large TS values indicate the presence of a source) for FSQRs (red) and BL Lac objects (blue) [68]. *Bottom - right*: Power density spectrum for bright FSQRs (red) and BL Lac objects (blue) [68].

(LSP/ISP) BL Lac objects [70]. Two kinds of variability arise from gamma-ray observations: one with a rather constant baseline with sporadic flares and one with a more complex temporal profile. The first type of variability is characterized by a flatter power density spectra resembling flickering and red noise with occasional intermittence. The other instead presents a structured temporal profile and a steeper power density spectrum. The average duration of the sporadic flares varies from 10 up to 100 days while the brighter flares can last as short as a fraction of a day. Defining a duty cycle N_b/N_{tot} as the fraction of monthly periods where the flux exceeds $\langle F \rangle + 1.5S + \sigma_i$, where $\langle F \rangle$ is the average flux, S is the total standard deviation and σ_i is the flux uncertainty of month i, it can be shown that

$N_b/N_{tot} \geqslant 0.05$ for bright sources, as visible in the bottom left of fig. 1.21, for both FSRQs and BL Lac [68]. The power density spectrum in the frequency range (0.033-0.5) month^{-1} for bright FSQR and bright BL Lac objects, shown in the bottom right of fig. 1.21, are described by a power law with mean index ~ 1.2. A variability index TS_{var} can be defined as follow [71]

$$TS_{var} = 2[log\mathcal{L}(\{F_i\}) - log\mathcal{L}(F_{const})] = 2\sum_i [log\mathcal{L}_i(\{F_i\}) - log\mathcal{L}_i(F_{const})], \quad (1.2)$$

where the log likelihood for the full time period $log\mathcal{L}(\{F_i\})$ can be expressed as a sum of terms for the individual time bands, $log\mathcal{L}_i$. A value of $TS_{var} > 41.6$ identifies a variable source at a 99% confidence level. On the top of fig. 1.21 the variability index described in eq. 1.2 is compared to the relative flux uncertainty and the gamma-ray luminosity of the sources. Brighter sources are found to be more variable than dimmer ones.
Information on the jet location and radiation mechanisms can be inferred from the differences in variability of FSQRs and BL Lac objects. Rapid variability is believed to be related to emission sites near the central nucleus while jets extended on a kpc scale can account only for weakly variable or quiescent emission [68].
The gamma-ray variability in blazars can be modelled either as an essentially steady source with perturbations or as a series of discrete, possibly overlapping, flares produced, for example, by travelling shock fronts [70]. The region of emission can be either homogeneous, with an acceleration of all the particles, or inhomogeneous, divided in multiple regions. Intermittent emission can be caused by stochastic processes such as instabilities and turbulence in the accretion disc or in the jet. Large number of randomly appearing weakly correlated elements with a limited lifetime, characterize such processes. Large flares are instead the product of sudden acceleration of relativistic electrons, related to bulk injections and strong internal shocks.
The study of gamma-ray variability is important both because it assists in discriminating faint sources from a fluctuating background and because, in the multiwavelength approach, it helps to identify the right counterparts within the gamma-ray position error box.

1.3.2 Pulsar Wind Nebulae Flares

The Crab pulsar was believed for long to be essentially constant in its emission, as far as that it is used as a standard candle in high energy astrophysics. However, AGILE (Astrorivelatore Gamma a Immagini LEggero [73]) observed in two different occasions strong gamma-ray flares from the Crab Nebula with energy between 100 MeV and 10 GeV [74]. These observations were confirmed by Fermi,

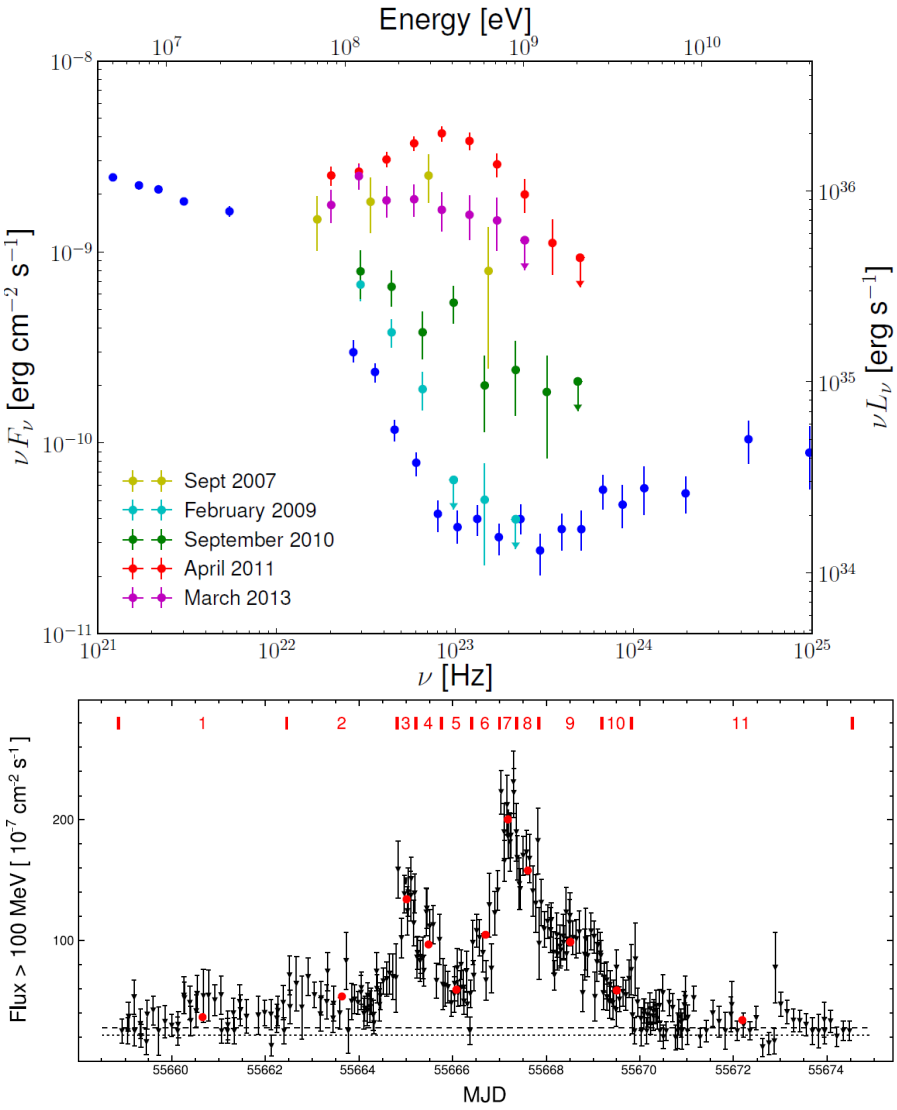

Figure 1.22: *Top*: Spectral energy distribution at the maximum flux level for five of the six Crab nebula flares detected as of September 2013. No spectrum has been published for the low intensity flare of July 2012. The blue points show the average nebula flux values [72]. *Bottom*: Integral flux above 100 MeV from the direction of the Crab as a function of time during the 2011 April flare. The points represent the sum of the nebula and pulsar fluxes. The dotted line indicates the sum of the 33-month average fluxes from the inverse-Compton nebula and the pulsar, which are stable over time. The dashed line shows the flux of the average synchrotron nebula summed to the pulsar. The red vertical lines indicate time intervals where the flux remains constant within statistical uncertainties. The time windows are enumerated at the top of the panel. The corresponding flux is shown by the red marker below each number. The spectral energy distribution for each of the time windows is shown in fig. 1.23 [72].

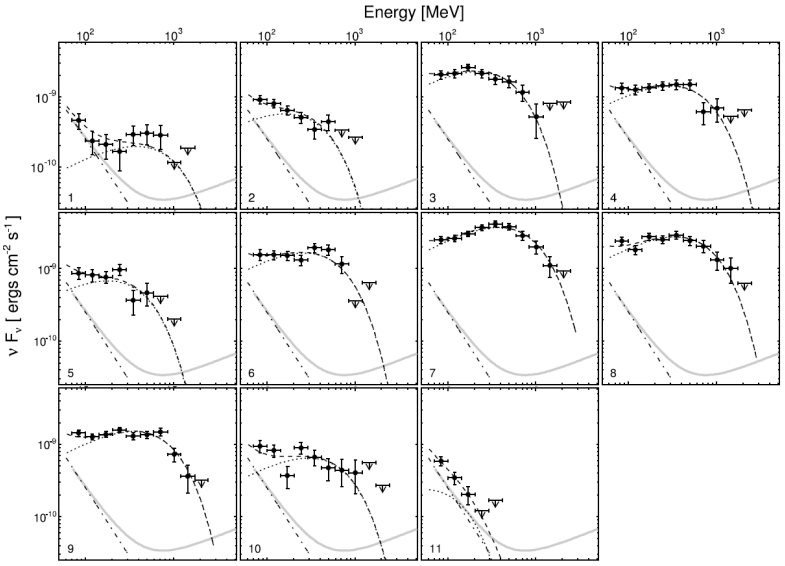

Figure 1.23: Spectral Energy Distribution evolution during the April 2011 Crab flare. The time windows are indicated in the bottom left corner of each panel and correspond to the ones indicated in fig. 1.22. The dotted line shows the Spectral Energy Distribution of the flaring component, the dot-dashed line the constant background from the synchrotron nebula, and the dashed line is the sum of both components. The average Crab nebular spectrum in the first 33 months of Fermi observations is also shown in gray. [72]

confirming the variability of the Crab [75].
As of today, six flares has been reported with an increase in the gamma-ray flux by a factor ~ 30 above 100 MeV on time scales down to ~ 6 hours [72]. The energy at which the flares occur is in the range between the synchrotron and inverse Compton component of the spectral energy distribution. While the synchrotron nebula is variable on all the time scales in which it can be resolved, the inverse Compton component and the pulsar flux are found to be constant in time. Typically the increase of the flux with respect to the monthly average lasts for ~ 1 week (e.g. bottom of fig. 1.22). The spectral behaviour is instead different for each flare, as visible in top of fig. 1.22. There can be no changes in the spectrum, e.g. the February 2009 flare, or a new spectrum component can be detected, as in the April 2011 flare and shown in fig. 1.23.
Although a multiwavelength campaign of observation was performed to study the flares at different energies, no increased emission was detected from radio to X-rays in any part of the nebula [72].
The presence of a more broad variety of variable emission in the Crab nebula has

been observed in both AGILE and Fermi data. Apart from the short flares, the presence of a longer (time scale of weeks, see e.g. the top of fig. 1.24) enhancement of the emission, called "wave", does not exclude an even broader variety (in flux and timescales) of enhanced gamma-ray emission [76]. Flares and waves share the same spectral properties (see bottom of fig. 1.24) and are more likely the result of the same class of plasma instabilities, responsible of the emission, acting on different intensities and timescales. Although the wave flux enhancement is smaller compared to the one in flares, the total emitted gamma-ray energy in the two cases are comparable, implying a larger region of emission.

Synchrotron emission is the only mechanism with an efficiency high enough to account for the enhanced emission [72]. However, in order for the emitted gamma ray to have an energy up to the GeV, a magnetic reconnection event is needed. Therefore, the gamma-ray flares are likely connected to explosive reconnection events triggered by current instabilities. In order to reproduce observations, or the lack of in other wavelengths, apart from a magnetic field higher with respect to the steady state, a population of accelerated electrons consistent with a monochromatic distribution is also needed [72].

The flares in the Crab nebula are recurring approximately once per year but they were not been detected in any other pulsar wind nebula [72]. The search of flares in other PWN as well as as the study of flares form the Crab nebula is still ongoing and it will be continued by GAMMA-400, trying to solve the remaining issues related to this kind of emission.

1.3.3 Gamma-ray bursts

Gamma-ray bursts (GRB, e.g. [78]) are sudden and violent emission of gamma rays most likely associated with the death of a massive star. The energy of the observed photons can reach several tens GeV. As an example, photons up to 95 GeV were detected from the GRB 130427A [79], and a photon of 24.7 GeV, which, given a redshift of the associated burst of $\approx$ 4.35, corresponds to an intrinsic energy in the cosmological rest frame of $\approx$ 147 GeV, from GRB 080916C [80]. The connection observed-rest frame energy for other high energy events is shown in the left of fig. 1.25. In order to produce such highly energetic gamma rays within the first few seconds of the burst, a highly efficient particle acceleration mechanism and large bulk Lorenz factors for the jet are required. Their prompt emission lasts for a variable time comprised between $\sim$1 s and $\sim$1000 s in the rest frame [77]. In the case of temporally extended emission, the flux at late times decays rather smoothly and can generally be fitted by a power-law $F_\nu \propto t^{-\alpha_L}$, α_L being the so-called late time index almost always close to 1, as visible on the right of fig. 1.25. This common decay behaviour is probably the indication of a common

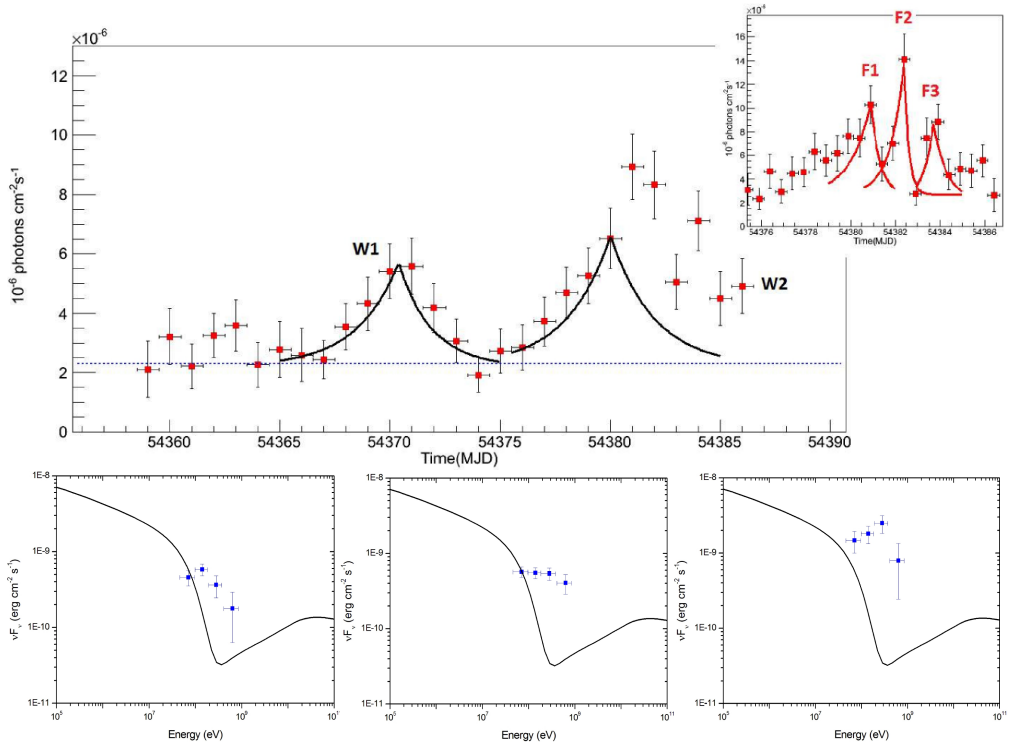

Figure 1.24: *Top*: Lightcurve (1 day bin) of the 2007 September-October Crab Nebula flare detected by AGILE. The inset corresponds to the 12 hr bin lightcurve around the flare. This episode is characterized by a very strong variability, with waves (black line, marked with a W) and flares (red line, marked with an F).[76]. *Bottom*: AGILE-GRID gamma-ray pulsar-subtracted spectrum of the Crab Nebula W1 (*left*), W2 (*centre*), and the flare F2 (*right*) [76].

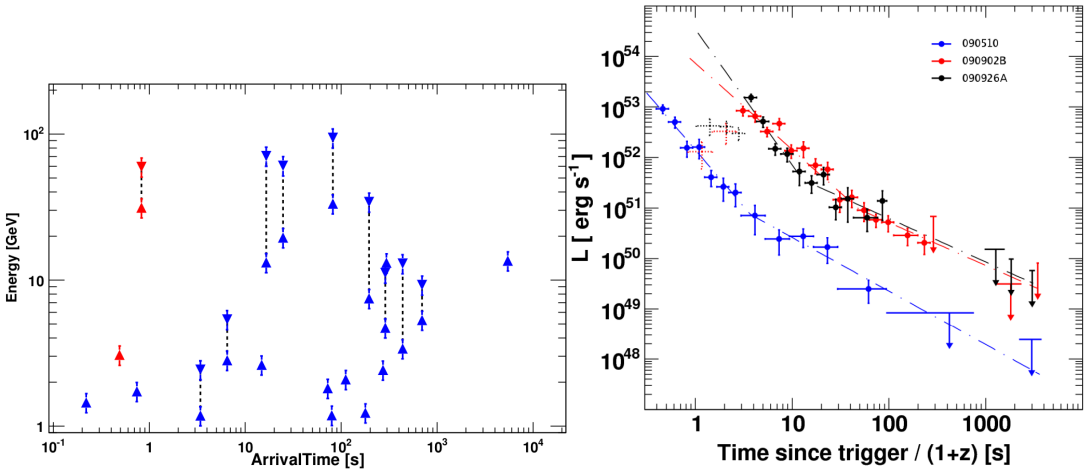

Figure 1.25: *Left*: Observed (upward triangles) and rest frame (downward triangles) energy and arrival time for highest-energy events associated with long (blue) and short (red) LAT detected GRBs. Vertical dashed lines connect the observed and the rest frame energy for the same burst [77]. *Right*: The decay of the luminosity L with time measured in the rest frame for the GRBs with detected extended emission. Dashed crosses are the luminosities before the peak times, which have not been used in the fits (see text in [77]).

emission mechanism. Hints on two different fluence classes were reported in the first Fermi LAT gamma-ray burst catalog: a hyper-fluent class, with few members and a fluence of $\sim (3-8)\cdot 10^{-5}$ erg cm^{-2}, and a more populated class with a lower fluence of $\sim (2-10)\cdot 10^{-6}$ erg cm^{-2}.
Fermi detected a lack of GRB high energy counterparts, possibly explained by an intrinsic cut-off in the GRB spectra. As an example of this deficiency, out of 730 detections made by Fermi Gamma-Ray Burst Monitor in the 8 keV - 40 MeV energy range, half of which occured in the LAT field-of-view, only 35 were detected at high energy ($>$ 20 MeV) by LAT. Of these 35, 28 have been detected above 100 MeV and 7 between $\sim$ 20 MeV and 100 MeV only [77].
Apart from the main apparatus, described in chap. 3, GAMMA-400 will mount six Konus-FG Gamma-ray burst monitor in order to study GRBs in a wider energy range and field-of-view (see also sec. 3.4). Four of these detectors will form a localization subsystem with a field-of-view of almost 2π sr, for GRB emitting photons in the 10 keV - 3 MeV energy range. The localization will be made in 1-2 s with an accuracy of $\sim 0.2-3°$, depending on the burst energy. The remaining two detectors will provide spectroscopic measure in the 10 keV - 15 MeV range while surveying the whole celestial sphere. A study on the feasibility of GRB study

with the main instrumentation aboard GAMMA-400 will be presented in chap. 6.

1.4 Cosmological Contents

Gamma-ray cosmology is an observational field related to the study of the intergalactic magnetic field, physics beyond the standard models of cosmology and particle physics and of the extragalactic background light. The next section is dedicated on this last item and on how gamma-ray observations provide constraints on models regarding the opacity of the Universe.

1.4.1 Extragalactic Background Light

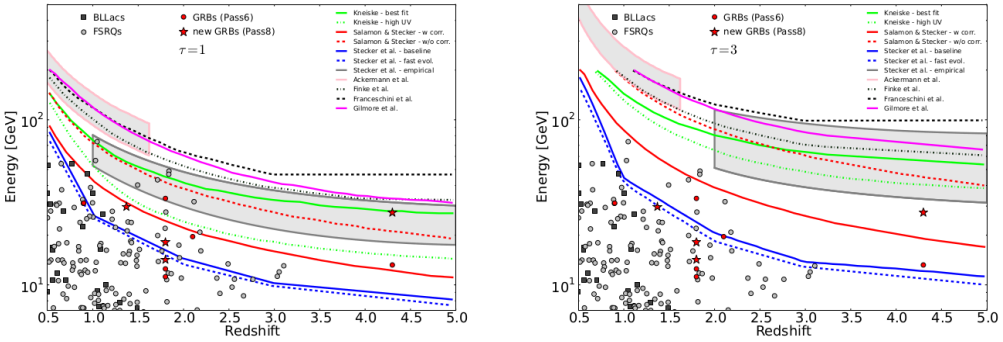

Figure 1.26: Highest-energy gamma rays from blazars and GRBs seen by the Fermi-LAT. Predictions of optical depth due to pair production, $\tau_{\gamma\gamma} = 1$ (*left*) and $\tau_{\gamma\gamma} = 3$ (*right*) from various EBL models are indicated by the lines and the shaded area outlined in grey. Gamma rays above model predictions in this figure traverse an EBL medium with a high gamma-ray opacity. The four new gamma rays reconstructed using the new event reconstruction are represented by the red stars.[80]

The Extragalactic Background Light (EBL) is a radiative component whose wavelength spans from ultraviolet to infrared [81]. The EBL, born with the emission from the first stars and increased ever since, represents one of the most intense cosmological background, second only to the CMB.
While usually the gamma rays can pass through inter-galactic space almost unimpeded, if their energy is high enough, they can interact with the EBL producing an electron-positron pair. This process leaves a feature in the spectrum of distant sources. The observations of these features can provide information on the time evolution of the density of the EBL, which is directly related to the star formation

rate. The measure of the EBL attenuation using gamma rays with energy above 10 GeV could give constraints on cosmological parameters as well as give the opportunity to discriminate between attenuation intrinsic to an observed source and EBL related attenuation.
Different models of gamma-ray opacity can be ruled out if a single photon at a given redshift is detected with an energy higher than predicted [82]. The higher the redshift the lower the allowed gamma-ray energy for a given model. Being stationary sources visible even at high energies and redshift, active galactic nuclei represent an ideal target to look for EBL related attenuation. Also gamma-ray bursts, which are visible up to high redshift, can be used to constraint the opacity of the universe. The problem of the gamma-ray burst is that they emits gamma rays for a limited time and rarely with energies greater than 10 GeV. Thanks to the reprocessing of the data with the new event reconstruction named Pass 8, Fermi-LAT has been able to reconstruct a 27.4 GeV gamma ray from a GRB at a redshift of ≈ 4.35 [80], the most constraining gamma ray from GRB up to date. It is in fact comparable to, or even slightly more constraining than, the Fermi-LAT from AGN, as visible in fig. 1.26.
GAMMA-400 will search for high energy gamma rays from cosmological distances thanks to its high energy ($\sim$ 1% for energies higher than 10 GeV) and angular resolution ($\sim 0.05^\circ$ at 100 GeV), which will help to identify the sources associated to the emission.

1.5 Summary

A summary of the scientific topics discussed in the chapter is presented in table 1.1 along with the requirements necessary to solve them with cosmic-ray or gamma-ray observations. A complete estimation of the performance of GAMMA-400, being part of the work done for this thesis, and a more thorough comparison with Fermi will be presented in chap. 4.
With the present configuration (see sec. 3.2) GAMMA-400 is able to satisfy all the requirements for cosmic-ray observation. As far as the gamma-ray observations are concerned, while having the required energy and angular resolution at high energy, it lacks in effective area and angular resolution at low energy. It should be noted that the different orbit and observational strategy between Fermi and GAMMA-400, even with a lower effective area of the latter, ensure a higher sensitivity of GAMMA-400 (see sec. 4.5.4). The angular resolution of GAMMA-400 at $\sim$ 1 GeV is presently of the same order of the one of Fermi. Some solutions to this problem, reducing the pitch of the Si strips or adding Si planes while reducing the tungsten in the tracker, are currently under study.

<table>
<tr><th></th><th>DM</th><th>CRs origin and propagation</th><th>Transients</th><th>EBL</th></tr>
<tr><td rowspan="2">γ</td><td>$\Delta E/E$
<5%</td><td>Ang. Res.
$< 0.3°$ @ 1 GeV
$< 0.04°$ @ 100 GeV</td><td>FOV
$\sim$ 2sr</td><td>A_{eff}
> 0.3 m^2 @100 GeV</td></tr>
<tr><td>A_{eff}
> 0.3 m^2</td><td>$\Delta E/E$
<5%</td><td>Timing
$\sim 100\mu$s</td><td>Ang. Res.
$< 0.04°$ @ 100 GeV
$\Delta E/E$
<5%</td></tr>
<tr><td rowspan="3">CR</td><td rowspan="2">GF
> 1 m^{2}sr</td><td>GF
>1 m^{2}sr</td><td rowspan="3">/</td><td rowspan="3">/</td></tr>
<tr><td>$\Delta E/E$
<45% nuclei
<5% e$^\pm$</td></tr>
<tr><td>$\Delta E/E$
<45%</td><td>Ang. Res.
$< 0.04°$ @ 100 GeV
Charge ID</td></tr>
</table>

Table 1.1: Summary of the scientific topics discussed in the chapter and the requirements to solve the remaining issues using both gamma-ray (γ) and cosmic-ray (CR) observation.

A first study on the GAMMA-400 timing capabilities will be presented in chap. 6.

1.6 Purpose of this analysis

The purpose of this analysis is to estimate the angular resolution, effective area and sensitivity of GAMMA-400, as well as designing a trigger for the observation of gamma rays using the tracker. Two possible geometries of the satellite, described in chap. 3, were analysed and reconstruction and trigger algorithms were developed. The results on the performance were applied to the simulation of a GRB in order to study the feasibility of GRB studies with the main instrumentation of GAMMA-400.

Chapter 2

Present Gamma-ray Space Missions

For the purpose of the analysis described in the next chapters it is useful to outline the present gamma-ray satellites: AGILE in sec. 2.1 and Fermi in sec. 2.2. The main structure of the different telescopes is similar: a tracker, a calorimeter and an anticoincidence, and the comparison of the performance can be made since the different instruments use similar detection techniques. As it will be shown in chap. 4 and chap. 5, some solutions that these missions found to problems related to both the reconstruction and the trigger can be applied to GAMMA-400 as well.

2.1 AGILE

AGILE (Astrorivelatore Gamma a Immagini LEggero) is a space mission designed to detect and study photons in the 30 MeV-50 GeV and 18-60 keV energy bands. Launched in April 2007, it is composed by three main detectors: GRID, Super-AGILE and a Mini-Calorimeter (MC) [83], shown in fig. 2.1.
The AGILE Gamma-Ray Imaging Detector (GRID) is sensitive in the energy range between 30 MeV and 50 GeV. It is characterized by a short deadtime for gamma-ray detection ($\lesssim 200\mu$s) and by a trigger based exclusively on Silicon plane detectors. GRID consists of a Silicon-Tungsten Tracker, a Cesium Iodide Mini-Calorimeter, an anticoincidence system made of plastic scintillators, and fast readout and processing units. The Silicon Tracker has the task to convert the gamma rays into an electron-positron pair. It is made by 12 planes, with two Si-layers per plane providing the X and Y coordinates of the interacting particles. In the first ten planes the two Si-layers are preceded by a tungsten layer (0.07 X_0) for gamma-ray conversion, absent in the last two since the GRID trigger requires at least three Si-planes to be activated. With this geometry GRID can achieve an angular resolution of $\sim 5' - 20'$ for intense sources, and a large field of view (~ 3 sr). The

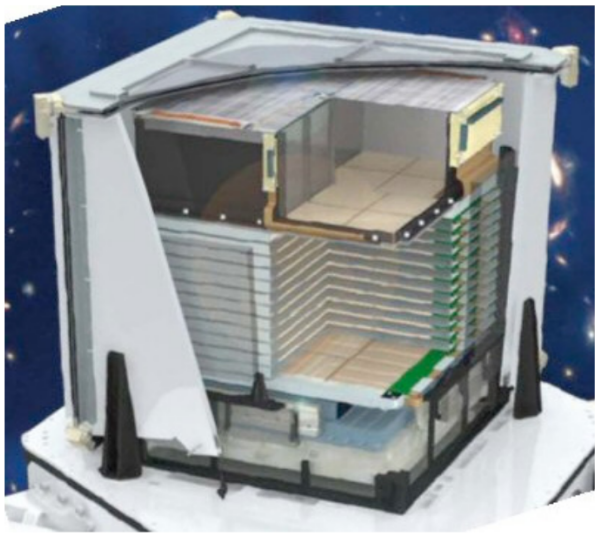

Figure 2.1: The AGILE scientific instrument showing the hard X-ray imager, the gamma-ray tracker, and calorimeter. The anticoincidence system is partially displayed, and no lateral electronic boards and harness are shown for simplicity. The AGILE instrument core is approximately a cube of about 60 cm size and of mass approximately equal to 100 kg. [83].

True energy (MeV)	PSF 68%
100	4.3°
400	1.4°
1000	0.7°

Table 2.1: AGILE monoenergetic PSF for three true energies [84].

anticoincidence system, completely surrounding all AGILE detectors, is designed to reject the charged particle background. Made by plastic scintillator layers, its segmentation together with the tracker trigger logic ensure the GRID large field of view.
The Super-AGILE detector is designed to operate in the hard X-ray range (18-60 keV). It consists of four Silicon square units arranged on a plane placed on-top of the GRID Silicon Tracker, and an ultra-light coded mask structure with a top Tungsten mask. Super-AGILE allows, together with GRID, the simultaneous gamma-ray and X-ray spectral study of high-energy sources as well as provides fast gamma-ray burst and transient alert and on-board trigger capability.
The MC is made of 30 Cesium Iodide (CsI) bars arranged in two planes, for a total (on-axis) radiation length of 1.5 X_0. Apart from obtaining additional information

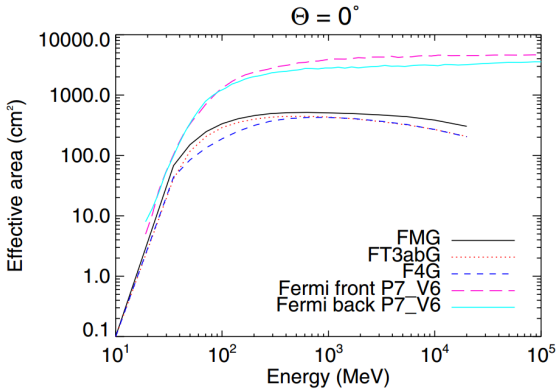

Figure 2.2: AGILE and Fermi effective area as a function of energy for normal incidence photons. AGILE curves are obtained for different filters, FM FT3ab and F4 (see reference for details) [84].

on the energy deposited in the CsI bars by particles produced in the Si-Tracker, the MC detects and collects events also independently. The energy range for this non-imaging detector is 0.25-200 MeV.
The AGILE effective area is shown in fig. 2.2 while its angular resolution is presented in table 2.1.

2.2 Fermi

The Fermi Gamma-ray Space Telescope, formerly known as GLAST (Gamma-ray Large Area Space Telescope) is a satellite observatory launched in 2008. Its primary instrument is LAT (Large Area Telescope), a wide field of view, high energy gamma-ray imaging telescope, covering the energy range from below 20 MeV to more than 300 GeV. The Gamma-ray Burst Monitor (GBM) is also present onboard [86]. Both instruments are shown in Fig. 2.3. Sensitive to X-rays and gamma rays with energies between 8 keV and 40 MeV, GBM could integrate the LAT observations of high-energies transient.
The LAT is designed to measure the directions, energies and arrival time of gamma rays incident over a large field of view, while rejecting background from cosmic rays. It is a pair-conversion telescope with a high precision tracker and calorimeter, each consisting of 16 modules arranged in a 4×4 array, an anticoincidence, made of plastic scintillator to reject the particle background, and a data acquisition system. Each tracker module is composed by 18 planes, with two layers of single-sided silicon each, to measure the X and Y coordinates similarly to AGILE. The first 12 planes have thin ($0.03X_0$) converter material (tungsten) before the silicon layer

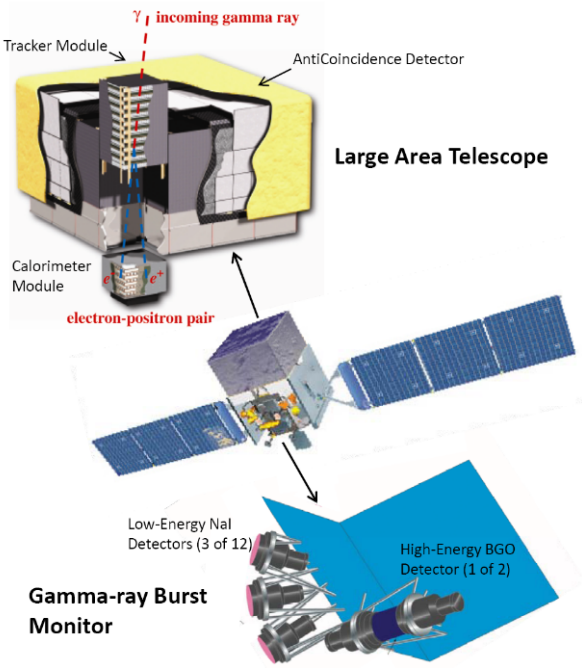

Figure 2.3: The Fermi Gamma-ray Space Telescope and its two instruments. The Large Area Telescope (LAT) images the sky in the energy band from 20 MeV to more than 300 GeV while the Gamma-ray Burst Monitor (GBM) complements the LAT for the study of GRBs and transients, providing spectral coverage from 8 keV to about 40 MeV [51].

in order to optimize the resolution at low energy. The tungsten in the following four planes is nearly six time thicker ($0.18X_0$) to maximize the effective area at the expense of less than a factor two in angular resolution (at 1 GeV) for photons converting in that region. The last two planes have no tungsten [5].
The purposes of the calorimeter are to measure the energy deposition due to electromagnetic showers and to image the shower development profile. Each calorimeter module has CsI crystals arranged in eight layers of 12 crystals each, optically isolated from each other. Each calorimeter module layer is aligned orthogonal with respect to its neighbors, forming an x,y (hodoscopic) array. Although the calorimeter is only 8.6 radiation length (for a total instrument depth of 10.1 X_0), the longitudinal segmentation enables energy measurements up to a TeV. From the longitudinal shower profile, an unbiased estimate of the initial electron energy is derived by fitting the measurements to an analytical description of the energy-dependent mean energy profile. Except at the low end of the energy range, the resulting energy resolution is limited by fluctuations in the shower leakage.

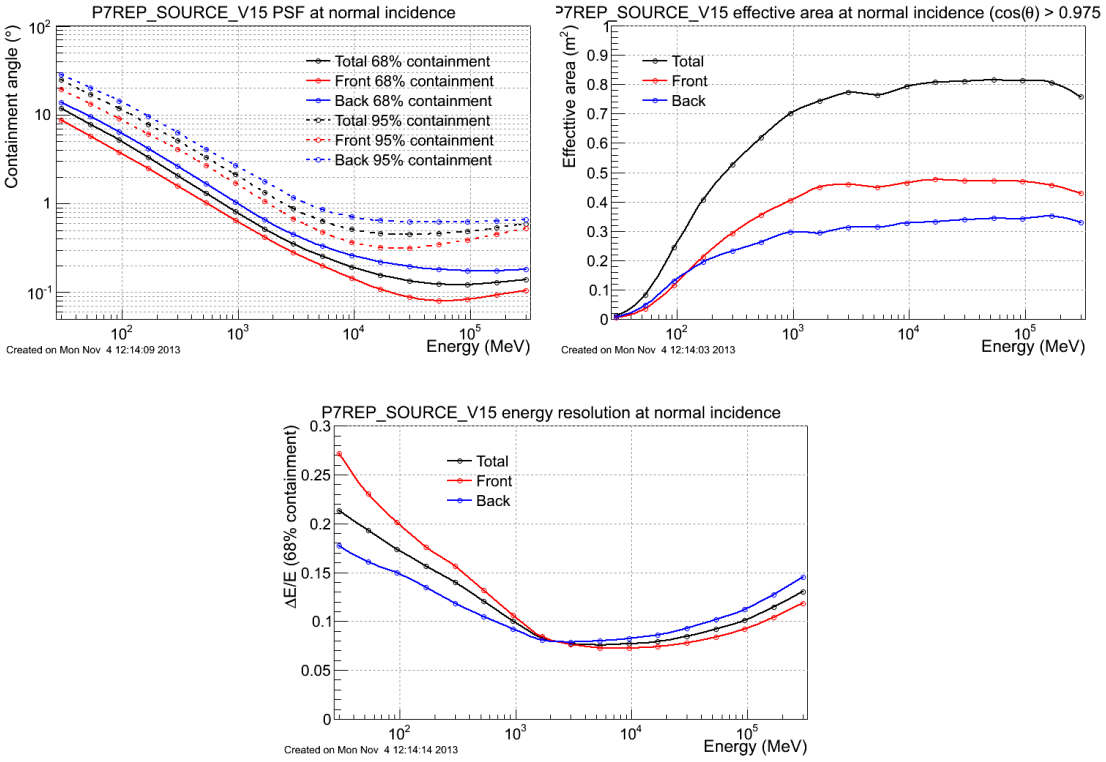

Figure 2.4: Fermi LAT performance: angular resolution (*top left*), effective area (*top right*) and energy resolution (*bottom*) [85].

The GBM consists of two sets of six low energy (8 keV to 1 MeV) NaI(Tl) (sodium iodide activated with thallium) detectors and a high energy (0.2 to 40 MeV) BGO detector mounted unshielded on opposite sides of the spacecraft. The GBM determines the direction of a burst by comparing the count rates of different detectors. If the count rate is higher than a certain threshold the spacecraft repoints automatically to allow the transient observation with the LAT [51].
The performance of the LAT corresponding to the status of the analysis known as Pass7 V15 and publicly released since October 2013 are shown in fig. 2.4. The results labelled as "front" are obtained using only the first 12 planes of the tracker, with the thinner tungsten layer, while "back" corresponds to the analysis made with the following four planes. Results marked as "total" are obtained with the overall instrument [85].

Chapter 3

GAMMA-400

The GAMMA-400 mission is being developed in order to achieve the scientific objectives discussed in the chapter 1 and answer some of the remaining questions in both cosmic-ray and gamma-ray physics. In this chapter the geometry of the instrumentation will be discussed. After a brief historical introduction (sec 3.1) the baseline will be presented in sec. 3.2. The last part of the chapter (sec. 3.3) is dedicated to the description of the enhanced configuration, developed by the Italian group and focused on the study of cosmic rays and both low (less than 1 GeV) and high energy gamma rays. An analysis of the performance of the two configurations will be presented in chap. 4 and chap. 5. Other detectors that will be mounted on the GAMMA-400 apparatus will be presented in sec. 3.4. The last section of the chapter, sec. 3.5, is dedicated to the comparison between the two configurations of GAMMA-400, Fermi and AGILE, the latter two described in chap. 2.

3.1 History

The GAMMA-400 experiment has a long history. The first concept for a satellite devoted to the study of high-energy gamma rays was developed in the late 80s [87], the post COS-B [90] era. At the time the 4 - 400 GeV energy range was largely unexplored. Originally, to cover this deficiency, the instrument should have detected gamma rays up to 400 GeV, from here the name GAMMA-400. As it can be seen in the top of fig. 3.1, to detect the high energy gamma rays a low number of greatly spaced scintillator planes was proposed. This kind of optimization, with changes to the implementation, is still used in the current baseline, as discussed in the following section.
During the years the energy range was extended up to several TeV [88], and the

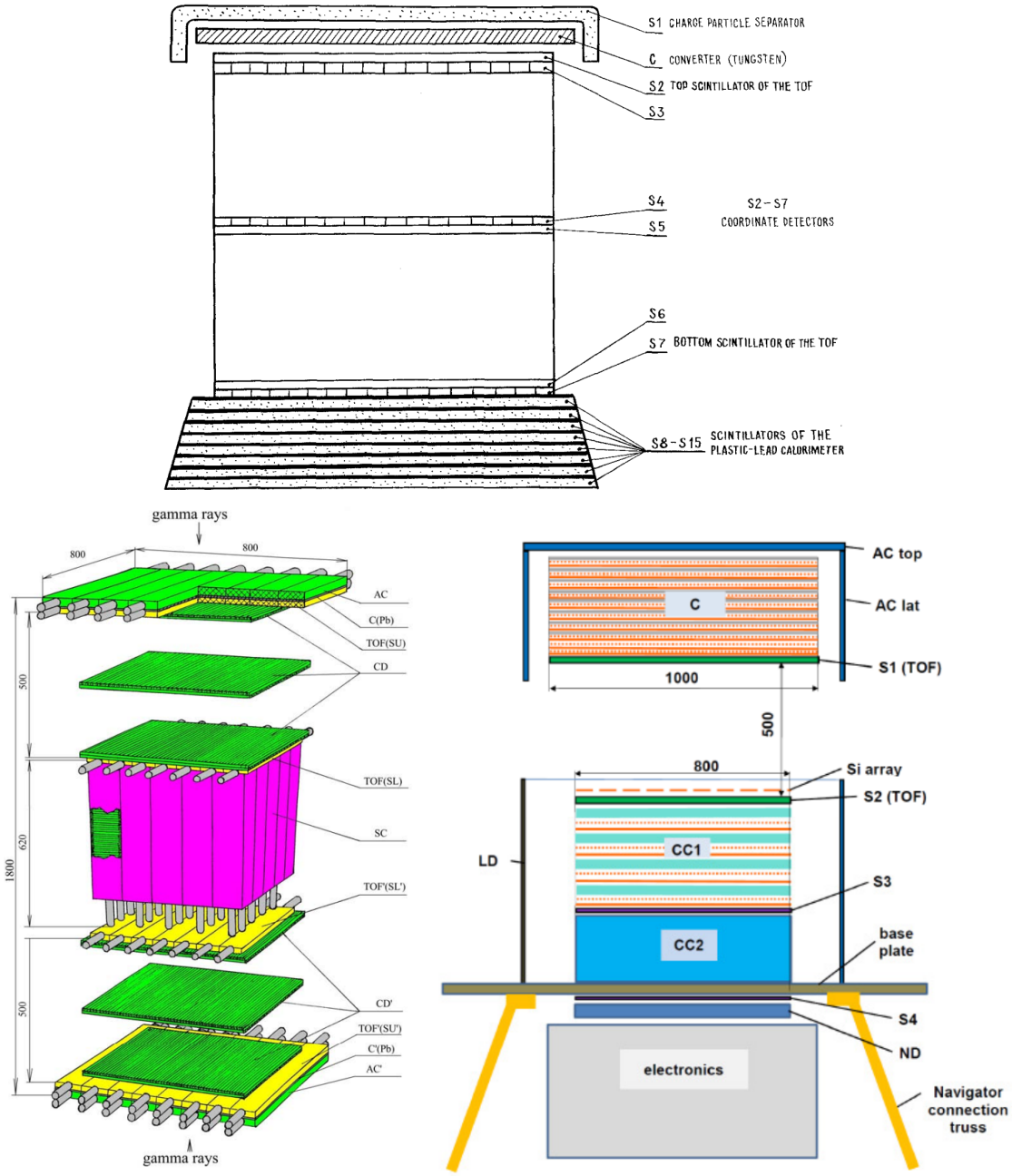

Figure 3.1: *Top*: First schematic of GAMMA-400 [87]. *Bottom left*: Baseline for the detection of gamma rays up to 10 TeV [88]. *Bottom right*: Last baseline before the collaboration with the Italian group [89].

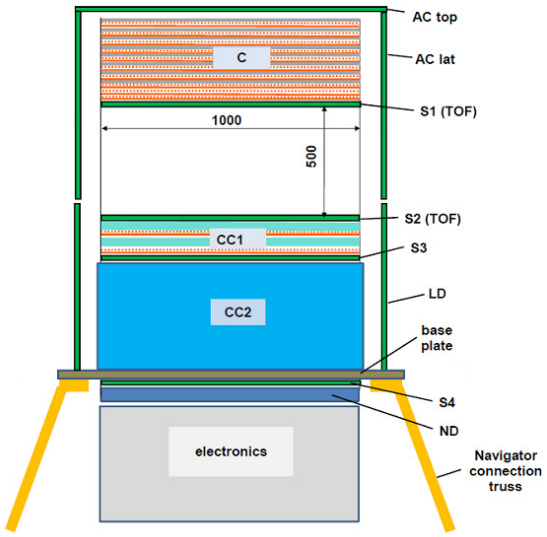

Figure 3.2: Schematic view of the baseline. From top to bottom: converter-tracker (C), anticoincidence system (AC top and lat), time-of-flight system (S 1 to 4), calorimeter (CC1 and CC2), charge identification system on the side of the calorimeter (LD) and neutron detector (ND). The dimensions values are in mm.

baseline changed accordingly (see bottom left of fig. 3.1). The project was officially approved by ROSCOSMOS, the Russian space agency, in 2009. The baseline at the time is shown in fig. 3.1 (bottom right) [89].
The last change in the baseline was the result of the collaboration with the Italian group. In the present baseline the pre-shower (CC1 in the bottom right of fig. 3.1) is composed by only two interleaved planes of Si and CsI(Tl), instead of four, and the CC2 is composed by an array of CsI(Tl) cubes instead of BGO bars. The present baseline will be described in the following. With this change the scientific objectives of the mission has broaden: GAMMA-400 will be able to study not only gamma rays and electrons but also protons and nuclei with energy up to $\sim 10^{15}$ eV.

3.2 Baseline

The latest [91] version of the baseline presents a different configuration of the calorimeter in order to achieve a larger effective area and improve the energy resolution and the geometrical factor. This change was made possible by the transition to a different launcher, with looser constraints on the mass of the payload, and the collaboration with the Italian group, who proposed a novel concept for the

Parameter	Tracker
Sensitive material	Si
Total dimensions (cm^3)	99.3 × 99.3 × 30.4
Towers	2×2
N planes	10
Single tower plane dimensions (cm^2)	48.9 × 48.9
First 8 planes height(cm)	2.794
Last planes height (cm)	2.772
Tiles per plane	5 × 5
Tiles dimensions (cm^2)	9.7 × 9.7
Strip per tile	768
W thickness first 8 planes (X_0)	0.1

Table 3.1: Specifics of the baseline Tracker

calorimeter. The baseline version of the instrument (see fig. 3.2) is now composed by:

- A Tracker (C) where the impinging gamma ray creates an electron-positron pair subsequently detected by Silicon layers (sec. 3.2.1);
- A calorimeter composed partially by CsI slabs and Silicon (CC1, sec. 3.2.2) and partly by CsI cubes (CC2, sec. 3.2.2);
- An Anticoincidence system covering both the sides and the top of the detector (AC top and lat, sec. 3.2.3);
- A Time-of-flight system composed by four layers of scintillating materials (S 1 to 4, sec. 3.2.4);
- A charge identification system (LD, sec. 3.2.5);
- A neutron detector (ND, sec. 3.2.6).

3.2.1 Tracker

The tracker has two purposes: one is to convert the photon into an electron-positron pair and the other is to detect the created pair in order to allow the reconstruction of the incoming direction of the photon. In order to fulfil these tasks Tungsten layers, to convert even the high energy photon, and Silicon microstrip detectors, to detect the passage of the particles, are used.

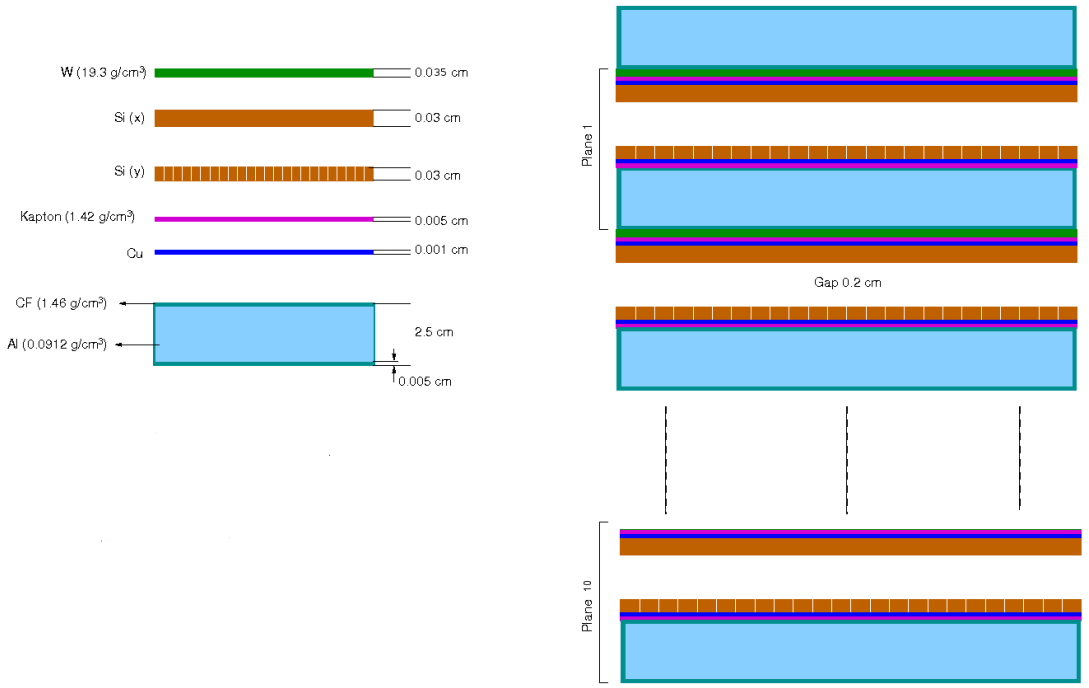

Figure 3.3: Schematic view of the baseline tracker.

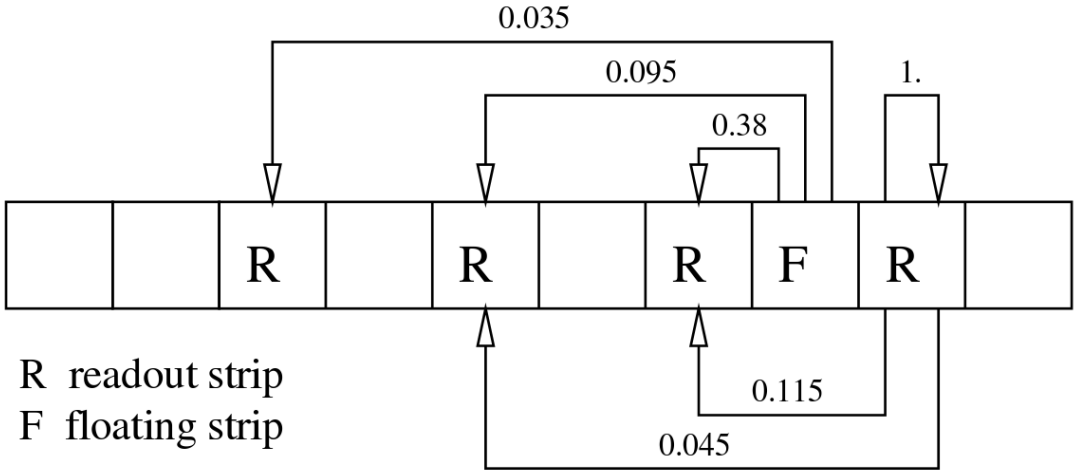

Figure 3.4: Schematic representation of the implementation of the capacitive coupling described in eq. 3.1. The symmetric couplings on the right are not represented. [92]

The tracker in the baseline is composed by 10 planes each of which comprise (see Fig. 3.3):

- The first eight planes have ~ 0.1 X_0 of tungsten, absent in the last two.
- A layer of Silicon strip coordinate detector (x view).
- A 2mm gap.
- A layer of Silicon strip coordinate detector (y view).

Each plane is completed with a honeycomb Aluminium support and the read-out system.
The tracker is organized in 4 towers with the electronics placed on their side. Each Silicon layer is divided into five 9.7×9.7 cm^2 tiles. The five tiles are wire-bonded together to form a ladder. The sensors are single-sided strip detectors with a strip pitch of 120 μm and a read-out pitch of 240 μm. Between each couple of read-out strips there is an intermediate floating strip and the capacitive charge division is exploited in a way similar to the AGILE read-out [92]. The total number of strips for one tile is 768 (384 read-out strips).
Using the capacitive charge division the total energy released in a read-out strip is equal to a weighted sum of the energy deposited in the nearby strips (see fig. 3.4)

$$\begin{aligned} E_k =& E_i + 0.38 \cdot (E_{i-1} + E_{i+1}) + 0.115 \cdot (E_{i-2} + E_{i+2}) + 0.095 \cdot (E_{i-3} + E_{i+3}) + \\ &+ 0.045 \cdot (E_{i-4} + E_{i+4}) + 0.035 \cdot (E_{i-5} + E_{i+5}), \end{aligned} \tag{3.1}$$

where k is the read-out strip index and i the index of any other strip (read-out or floating). These numbers, result of an AGILE test-beam [92], are used for the simulation until a test beam of the GAMMA-400 tracker provides the real values. It is under study the possibility to reduce the pitch to 80 μm while maintaining the same read-out pitch, resulting in the same number of read-out channels but better position resolution.
The read-out of the Silicon strips is analog, differently from the digital read-out of experiments such as Fermi. This state-of-the-art detector optimizes the signal to noise ratio (hence the achievable resolution as more thoroughly discussed in sec. 4.1) and offers a full information on the charge released in it, while maintaining the power consumption as low as possible. Moreover the tracker is planned to provide the main trigger to the instrument for the detection of gamma rays (see chap. 5). Currently some possible modifications, such as reducing the tungsten thickness, are under study. For this purpose, in the simulations used to estimate the performance, described in chap. 4, the total radiation length of a plane is ~ 0.08 X_0.

3.2.2 Calorimeter

The calorimeter of the baseline is divided into two parts. The first part, called CC1, is composed by CsI(Tl) (later referred to simply as CsI) and Silicon and it is specifically designed to help the reconstruction of the direction of the incoming gamma rays. The second part, called CC2, is composed of CsI cubes only and it has the task of analysing the development of the shower created by the incoming particles (protons, nuclei, electrons or gamma rays).

CC1

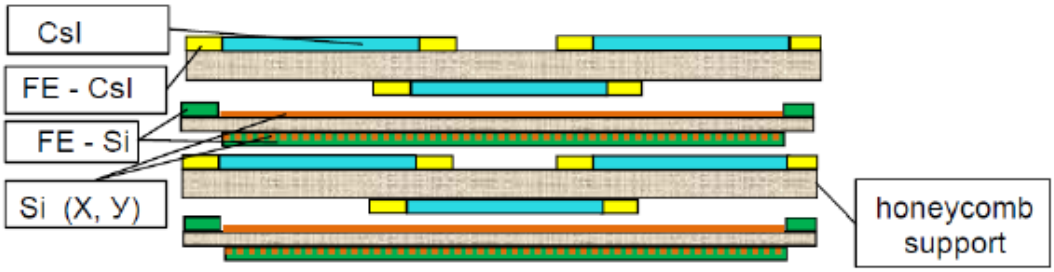

Figure 3.5: Schematic view of the CC1, complete of CsI and Si planes, support and Front-End (FE) electronics.

The CC1 (also referred to as pre-shower in the following) comprises two planes of CsI and two planes of Si, arranged as in fig. 3.5. The Si planes are composed by two layers of Si, for the x and y view, and a support, equivalently to the tracker planes.
Each CsI plane consists of 60 slabs arranged in a 3×20 array. The size of each slab is $33.3\times5\times2$ cm^3. The two planes differs only for the orientation of the CsI slabs array: the first one has 20 tiles along the x axis and 3 along the y, vice versa for the second one. The radiation length of one of these planes is $\sim$1 X_0, while the radiation length of the overall CC1 is $\sim$2 X_0.
The main purpose of the CC1 is helping the detection of gamma rays. Thanks to the long lever arm ($\sim$ 50 cm) between the tracker and the CC1 and the presence of the finely pitched Silicon, information from this detector helps the reconstruction of the direction of highly energetic gamma rays. The reconstruction can be also performed using information from the CC1 only. The results, even though worse than those obtained with the information from the tracker, help to increase the overall effective area and widen the field of view, using only the two Si planes, otherwise limited by the same long lever arm. A more detailed discussion on the

Parameter		CC2
Scintillating medium		CsI(Tl)
N×N×N		28×28×12
L(cm)		3.6
Crystal Volume (cm^3)		46.7
Gap (cm)		0.3
Total Mass (kg)		1981
N. crystal		9408
Overall size(cm^3)		109.2×109.2×46.8
Depth	$(X_0 \times X_0 \times X_0)$	54×54×23
	$(\lambda_I \times \lambda_I \times \lambda_I)$	2.6×2.6×1.1

Table 3.2: Specifics of the baseline CC2

reconstruction, both using information from the CC1 only and from the tracker and the CC1, can be found in sec. 4.4.

CC2

The CC2 calorimeter is composed by 28×28×12 CsI cubes of 3.6 cm of side ($\sim$ 1 Moliere radius). This novel concept, never used before in any space mission, was originally designed by the Italian INFN group and it is more thoroughly described in sec. 3.3.2. A summary of its specifics can be found in table 3.2.
This baseline version of the calorimeter has been optimized for the detection of gamma rays. The detection area has been enhanced with respect to the enhanced design described in sec. 3.3.2, from 78×78 cm^2 to 109.2×109.2 cm^2 at the expenses of the depth, reduced to 46.8 cm. In this configuration a greater number of gamma rays, the observation of which is triggered by the tracker, leave a signal in the calorimeter, ensuring a good energy resolution in all energy ranges, as seen in fig. 3.6.
This optimization for gamma-ray detection worsen the possibility of reconstructing the shower development for charged particles, especially hadrons for which the longitudinally development is significantly larger. While the planar geometrical acceptance on five surfaces is similar in the two cases (10.1 m^2sr for the baseline vs. 9.55 m^2sr for the enhanced configuration), when the containment selection criteria of the shower are applied, the baseline calorimeter suffers a reduction of the geometrical factor.

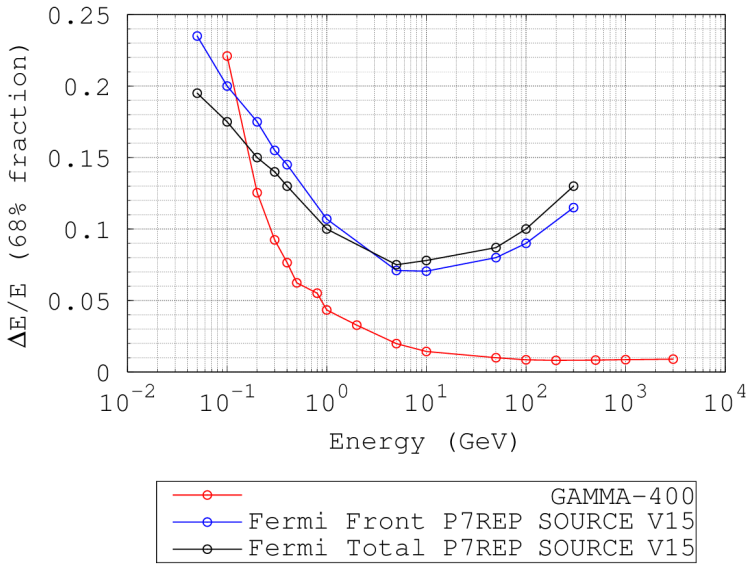

Figure 3.6: Comparison between the energy resolution of Fermi-LAT and GAMMA-400, using information from both calorimeter and tracker [91].

3.2.3 Anticoincidence

The anticoincidence system is a critical part of every gamma-ray space mission. The interaction of a charged particle or of a pair created by a gamma ray in the tracker are very similar. An anticoincidence, where a signal is related only to the passage of a charged particle, is necessary to discriminate between these two cases. Given the large particle background caused by the GAMMA-400 orbit, the anticoincidence is also used to provide a way to reduce the data downlink, as it will be discussed in chap. 5.
The anticoincidence of GAMMA-400 will be similar to the one of Fermi-LAT: a large number of plastic scintillator tiles will surround the instrument. The scintillators will be read out by Silicon PhotoMultipliers (SiPMs). Differently from Fermi-LAT, the system will have time-of-flight capabilities in order to help in the rejection of backscattering particles.
Given the critical importance of this part, a study of different configuration is undergoing. Two possible solutions are under study: one making use of bars and one using square tiles.

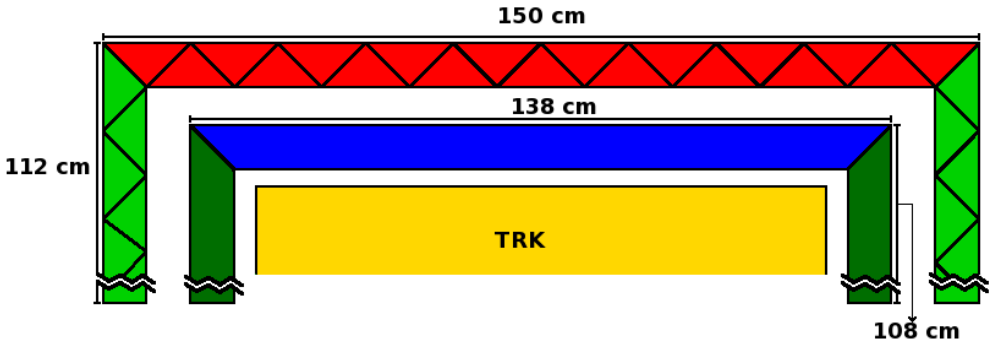

Figure 3.7: Side view of the anticoincidence system using bars: in red and blue the anticoincidence top, light and dark green side. The support, while present in the simulation, is not shown.

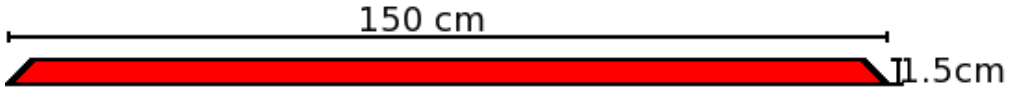

Figure 3.8: One of the bar forming the anticoincidence plane

Bars

The configuration using tiles (described later), while easier to implement, has a flaw: the connection between one tile and the other, in which there is the possibility for particles to pass without interaction. To ensure complete shielding a different segmentation is under study: instead of square tiles (like the one describe below), an array of prism-like bars are used.
Both the top (ACT) and the side (ACS) anticoicidence are composed by two planes with bars perpendicular to each other, for the x and y view respectively, as shown in fig. 3.7. Each of these bars has a height of 1.5 cm and, inside a plane, between the upper and lower layer a 0.02 cm layer of optical glue is positioned. The base of the bar is 3 cm wide and the total length of the bar can range from 138 cm, for the inner plane, up to 150 cm for the outer plane, as shown in fig. 3.8.
The downside of this configuration are the higher number of read-out channels needed and the higher radiation length of the system, which required two planes of scintillator also for the ACT. The radiation length of the anticoincidence should be kept as low as possible to avoid the conversion of the gamma ray inside the plane and before the tracker sensitive volume.

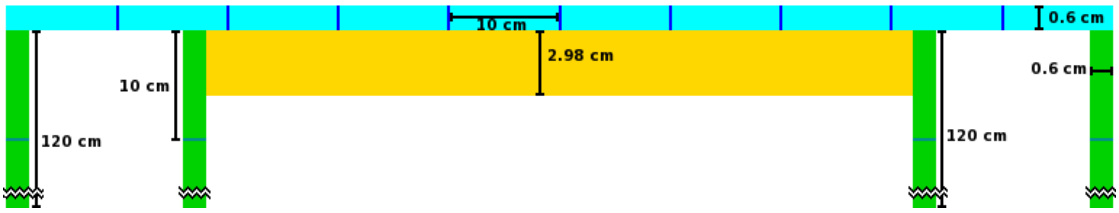

Figure 3.9: Side view of the anticoincidence system: in cyan the anticoincidence top, in green the side and in yellow the support of honeycomb Aluminium.

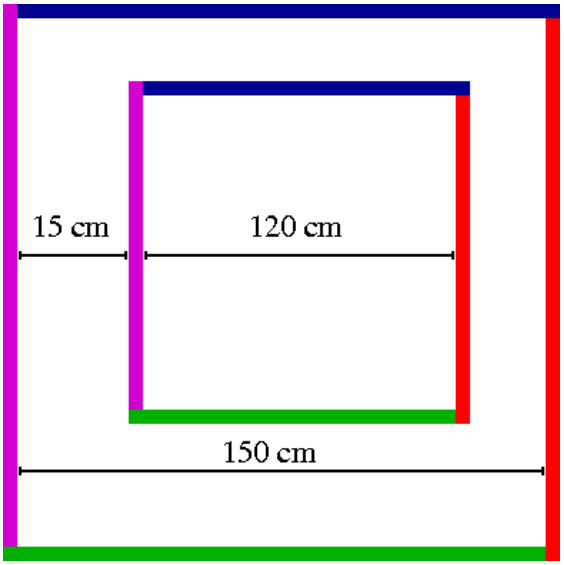

Figure 3.10: Upper view of the ACS: in different colors the different sides. It is visible the slight shift in order to minimize the gaps

Tiles

In this configuration the ACT is composed of only one plane while the ACS has still two different planes. Each of the planes is 0.6 cm thick and it is divided in tiles of area 10×10 cm^2. The ACT consists of an array of 15 × 15 of such tiles. The ACS, as said before, has two planes spaced by 15 cm: the inner one has 12×10 tiles while the outer one 12×15. A front view of the ACT and ACS is shown in fig.3.9. The great gap between the planes is necessary in order to try to exploit the timing information to discriminate between particles coming from the outside and particle escaping from the inside. In order to minimize the gaps between the planes, the different sides of the ACS are slightly shifted on the side as visible in fig. 3.10.
This configuration is the one used for the simulations and analysis of the simulated data presented in chap. 4, 5 and 6.

3.2.4 Time of flight

The time-of-flight system is necessary to discriminate bacsksplashed particles from the calorimeter from downgoing particles. The time-of-flight comprises four planes, each composed by two 100×100×0.5 cm^3 plastic scintillator layers:

- **S1**: a plane just under the tracker;
- **S2**: a plane just before the CC1;
- **S3**: a plane between the CC1 and the CC2;
- **S4**: a plane after the CC2 and the base plate and before the neutron detector.

A definitive configuration and segmentation for the time-of-flight has not yet been decided. In the simulation and analysis presented in chap. 4, 5 and 6 the segmentation described in the following has been used. Each layer inside a plane is divided in 10 tile (10×100×0.5 cm^3 each). Tiles on different layers in a same plane are positioned perpendicular to each other in order to provide the separate x and y views. The goal timing resolution for the system is 0.5 ns.
Given the high depth of the calorimeter, the number of backsplashed particles is expected to be large and the time-of-flight will be of great importance to discriminate these bacsksplashed particles from the calorimeter from downgoing particles. As explained in chap. 5, the time-of-flight is of help also in the trigger, thanks to its fine timing resolution and position.

3.2.5 Charge identification system

Because of the dual nature of the instrument, devoted not only to the detection of gamma rays but also of protons and nuclei, a charge identification system is necessary. The system is designed to measure the specific ionization (dE/dx) of the incident particle, proportional to the square of its charge, before the development of an electromagnetic or a hadronic cascade in the calorimeter. Two options are currently under study: a Silicon pixel array or a charge identifier system integrated with the calorimeter.
In the first option the calorimeter is surrounded by a Silicon array module at a standoff distance. Each side is composed by two layers of Silicon, with pixel of 1.125×1.125 cm^2. The pixels are arranged in 9.47×9.47 tiles. In order to achieve a seamless active region over the whole array, the tiles are overlapped in both dimensions of 3.2 mm. The overlapped tiles are arranged in ladders, the odd ones are positioned on the lower layer while the even ones are on the upper layer. This configuration, already extensively tested at CERN, provides incident particle identification and adequate charge resolution (better than 0.2e for light elements to $\sim$0.35e for Fe) [93].
The second option foresees to replace the cubes on the faces of the calorimeter with as many thinner scintillating square tiles. The output of such a configuration will be multiple measurement of dE/dx of the incident cosmic ray before the first inelastic interaction. Multiple measures can help into the identification of nuclei interacting in the detector material. The intrinsic pixel geometry of the tile array would allow to discriminate the ionization signal generated by the incoming particle from the one produced by back-scattered shower particles, thereby reducing the probability of misidentification. The main difficulty in designing this configuration is to minimize the considered albedo particles from the calorimeter and back-scattered particles. The advantages over the Silicon array are the easier and cheaper technology of a detector fully integrated with the calorimeter which still provide an adequate charge discrimination capability. The integration with the calorimeter would allow a common design of the sensors and the readout electronics [93].

3.2.6 Neutron Detector

The neutron detector, placed underneath the calorimeter, helps to reduce the background from charged particles. The neutron detector that will be mounted on GAMMA-400 is composed by two layers for a total size of $100 \times 100 \times 8.5$ cm^3 [94]. Each layer is composed by 10 10×100 cm^2 strips, each of which comprises a thin scintillator layer. The strips in the two layers are mounted perpendicular

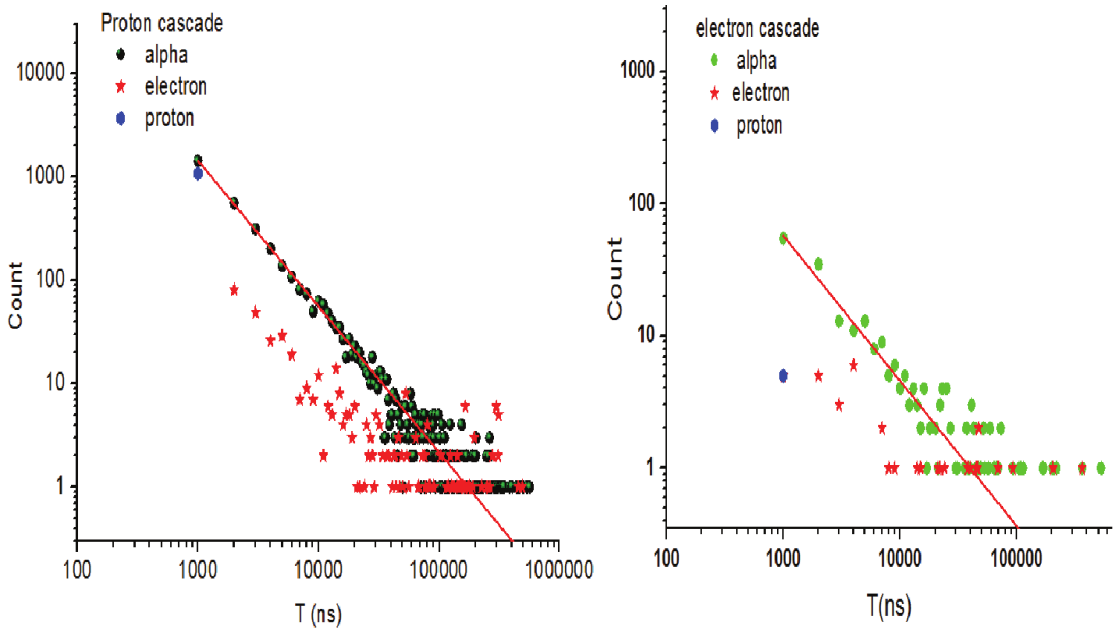

Figure 3.11: Number of particles in a shower created by a 1 TeV proton (*left*) and a 400 GeV electron (*right*) at a time T from the trigger [94]

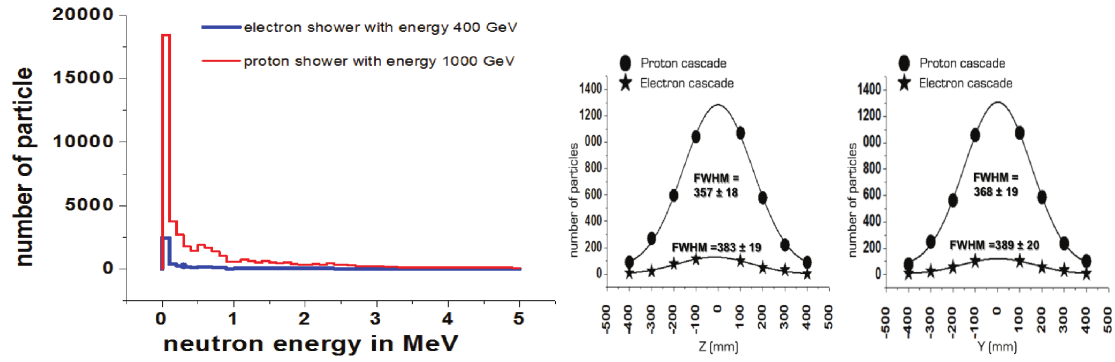

Figure 3.12: *Left*: Neutron spectra for proton and electron showers [94]. *Right*: Spatial distribution of events in the neutron detector approximated by a normal distribution (ten 1 TeV protons and ten 400 GeV electrons [94].

to one another to form the x and y view. The scintillating light is gathered to a photomultiplier by an optical fibers. The light is produced, together with α particles, by the interaction of a neutron with the scintillator material (ZnS(Tl)+^{6}LiF): ${}^6_3Li + {}^1_0n^4 \rightarrow_2 He + {}^3_1H + 4.8$ MeV. Each scintillating layer is alternated with a layer of organic moderator with the double function of increasing the neutron detection efficiency and setting a time threshold to separate neutrons from other particles.
The electron/hadron discrimination is achieved by the analysis of three characteristic of the shower: time development, number of particles and spatial distribution [94]. The time distribution of charged particles in a shower shows a difference whether the shower is produced by an electron or a proton, as shown in fig. 3.11. Fitting to the two distributions the function $N = a \cdot T^{-b}$, where N is the number of particles and T the time, lead to $a = (294 \pm 4) \cdot 10^5$ and $b = 1.410 \pm 0.002$ for protons and $a = (114 \pm 7) \cdot 10^3$ and $b = 1.09 \pm 0.01$ for electrons.
For two different events, one originated by an electron and another by a proton, with the same energy released in the neutron detector, the number of neutron differs by more than an order of magnitude, as shown on the left of fig. 3.12. The spatial distribution of the particles is also different for an electron or a hadron: the Full Width Half Maximum (FWHM) of the fit to the distribution appears wider for electrons than for protons, as shown on the right of fig. 3.12.

3.3 Enhanced configuration

When the Italian INFN group entered the GAMMA-400 collaboration, while working on the improvement of the baseline, it started to develop also a different configuration of the instrument. This configuration [95], while maintaining an optimal detection capability for high energy gamma rays, aims at improving the angular resolution at low energy (less than 1 GeV) as well as detecting also cosmic rays (electrons up to $\sim$ 1 TeV, protons and nuclei up to 10^{15}-10^{16} eV, the knee region).
This optimization for the cosmic-ray studies brought to the designing of a novel concept for the calorimeter (sec. 3.3.2), later accepted as part of the baseline (sec. 3.2.2). The other main difference with respect to the baseline is in the tracker, as it will be discussed in sec. 3.3.1.

3.3.1 Tracker

The necessity to improve the angular resolution at low energy, in a multiple scattering dominated regime, while maintaining the same performance at high energy, leads to the creation of a 25 planes tracker with thin tungsten foil.

Parameter	Tracker
Sensitive material	Si
Dimensions (cm^3)	$99.3 \times 99.3 \times 71.9$
Towers	2×2
N planes	25
Plane dimensions (cm^2)	$48.9 \times 48.9 \times 2.776$
Tiles per plane	5×5
Tiles dimensions (cm^2)	9.7×9.7
Strip per tile	768
W thickness (X_0)	0.03

Table 3.3: Specifics of the Tracker of the enhanced configuration

While the structure of a plane is equal to the structure of a tracker plane of the baseline, the tracker is now homogeneous. Each of the 25 planes has the same amount of tungsten in it, ~ 0.03 X_0, for a total of ~ 1 X_0 for the whole tracker. The goal is to achieve the best possible instrument by combining some of the characteristic of Fermi and AGILE. The analog read-out, already present in AGILE, ensures a good resolution at high energy while the thin tungsten, similar to the one of Fermi LAT front, and a size of the instrument closer to Fermi, assures a better resolution at low energy and a good effective area (see chap. 4 for a discussion and comparison of the performance).

3.3.2 Calorimeter

The calorimeter of the enhanced configuration is cubic, homogeneous, isotropic and finely segmented in three dimensions [93]. It is composed by an array of 20×20×20 cubes of CsI each of which has a side of 3.6 cm, the same as for the baseline CC2. Between two cubes a small gap of 0.3 cm allows larger size (thus a bigger acceptance) of the detector and the possibility to accomodate the support structure and photosensors. This geometry of novel concept ensures a large geometrical factor and effective area thanks to the possibility of detecting particles coming not only from above but also from the sides of the instrument. In addition it ensures an adequate electron/hadron rejection factor and a good energy resolution for the detection of electrons and high energy gamma rays.
The CsI has been chosen as the scintillating material instead of the BGO because of its lower density and higher radiation length. Having a tight mass constraint, a lower density material permits the construction of a larger detector. Thanks to a greater radiation length an excessive segmentation is not required and the total

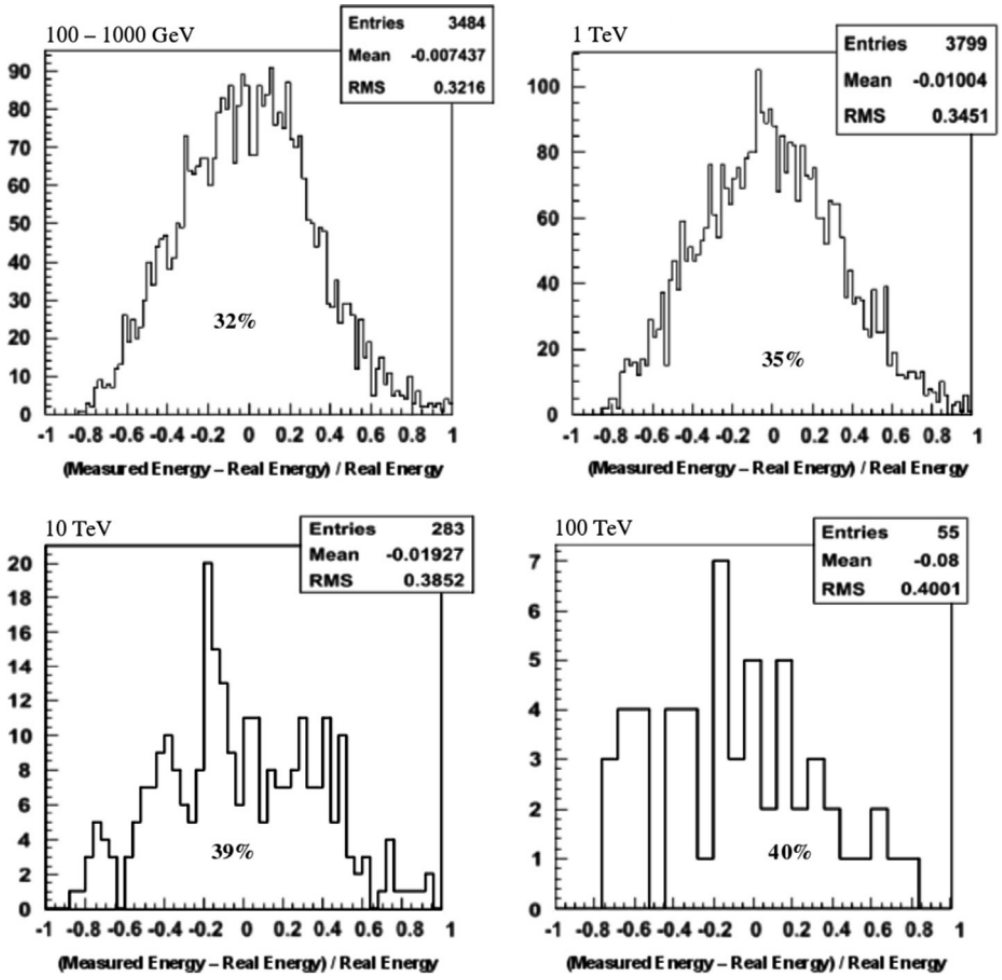

Figure 3.13: Energy resolution for protons at various energies [96].

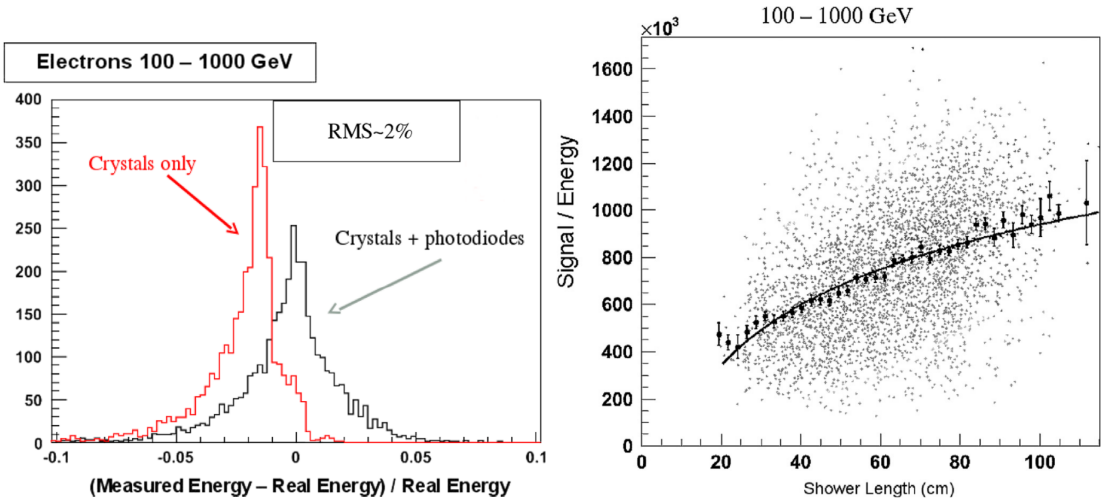

Figure 3.14: *Left:* Energy resolution for electrons in the 100-1000 GeV energy range. The effect of ionization on the photodiodes, resulting in a shift of the distribution towards higher values, is also shown. [96]. *Right:* Signal/(real energy) (in electrons/GeV) as function of shower length for protons. Small light dots are single events, while big dots are the mean values as a function of the shower length [96].

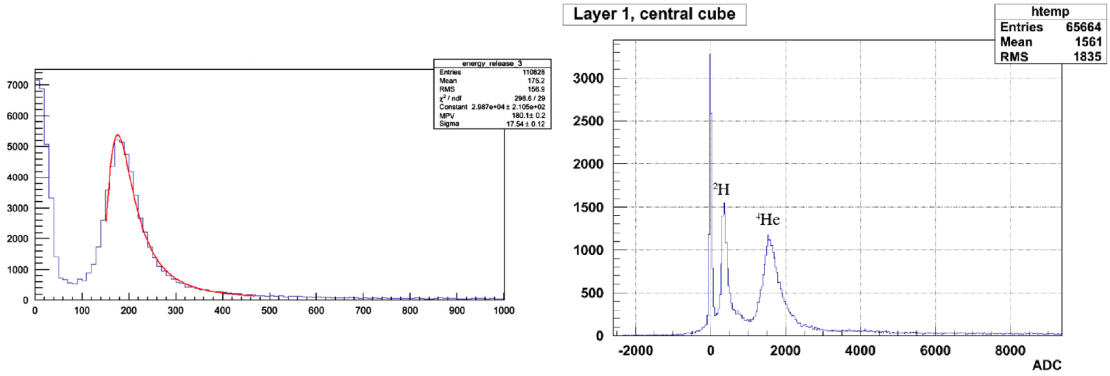

Figure 3.15: *Left:* Signal of 150 GeV/c muons in the calorimeter pre-prototype [96]. *Right:* Signal of Z/A= 2 ions at 30 GeV/c in the calorimeter prototype [96].

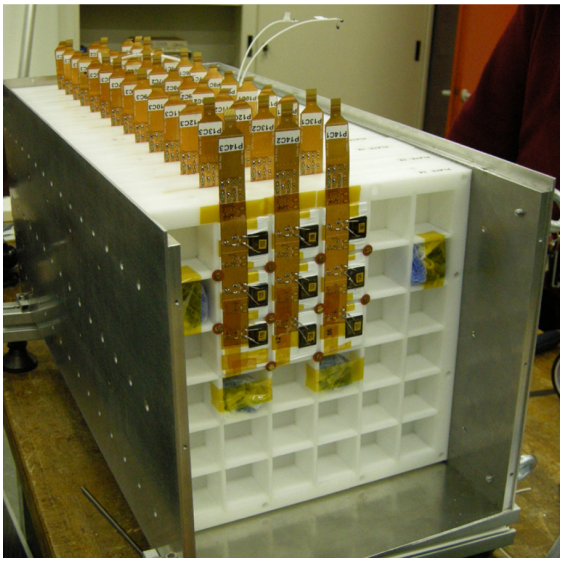

Figure 3.16: The 14 layers prototype inside the Al frame. The photodiodes are visible on the first layer as well as the kapton readout cables [96].

number of read-out channel is reduced.
Since up to 10% of a particle energy can be deposited in a single crystal, the dynamic range to be covered extends from 0.5 MIP (for non-interacting protons) up to 10^7 MIP. To ensure the coverage of this broad range two photodiodes are to be coupled to each crystal: a large ($\sim 9.2\times9.2$ mm^2) photodiode for small signals and a small ($\sim 0.5\times0.5$ mm^2) one for large signals. Each photodiode is then read by a high and a low gain amplification circuit, for a total of 4 channels per cube.
Simulations using FLUKA [97; 98] and Geant4 [99] were performed using electrons and protons. Different selection criteria were used in the two cases. Being the total Geometrical Factor GF equal to 9.55 m^2 sr, the efficiency of the selection, ϵ, defines the effective geometrical factor $\mathrm{GF}_{eff} = \epsilon \cdot 9.55$ m^{2}sr.
For electrons, the impact point is required to be at a distance of at least two crystals from the border and the shower to cross at least 21 X_0. The efficiency related to this selection is 36%, leading to a GF_{eff} of 3.4 m^{2}sr. The energy resolution for electrons up to 1 TeV is $\sim 2\%$, as shown in the left of fig. 3.14, but, using selective cuts, it can be improved while maintaining the efficiency above 30%.
For protons, no shower containment criteria are used but at least 50 crystals with a signal higher than 50 MIPs are required. To reconstruct the energy of the particle, the correlation between shower length and signal, whose fit is shown on the right of fig. 3.14, is used. The energy resolution varies between 30-40%, as reported in fig. 3.13, enough to detect a change in the proton spectrum slope. The possibility

of an improvement of the energy resolution down to 15-20% using hardware and software compensation is under study. One of these technique is the possibility to compensate hadronic showers by discriminating between the fast Cherenkov light emitted by shower particles and the slower scintillating light. The selection efficiency varies from 35% at 100 GeV to 47% at 10 TeV, which leads to a value of the effective geometric factor between 3.3 m^2sr and 4.5 m^2sr.
Using FLUKA simulations the calorimeter capability of electron-proton discrimination has been studied. The results indicate a rejection factor of $0.5 \cdot 10^6$ and a contamination of the electron spectrum due to bad-reconstructed protons around 1%.
As said before, the peculiar configuration of the calorimeter allows to detect particles coming also from the side of the detector. Thanks to its depth and segmentation, the calorimeter can be used to reconstruct the direction of the incoming particle, helping to refine the angular resolution in the tracker and increase the effective area. A detailed discussion on the reconstruction in the calorimeter is presented in sec. 4.2. In this section, the possibility to shift the planes in the x-y direction in order to improve the effective area and angular resolution at normal incidence will also be discussed.
Two test beams has already been performed at the CERN SPS accelerator facility [96]: the first using a smaller so-called "pre-prototype" and the second using a properly called prototype. The pre-prototype is made of 12 CsI(Tl) crystals of 2.5 cm side length, arranged in 4 layers of 3 crystals each; the prototype has 126 CsI(Tl) crystals of 3.6 cm side length, arranged in 14 layers of 9 cubes (Fig. 3.16). For both prototypes, one 9.2×9.2 mm^2 Excelitas VTH2090 photodiode per crystal has been used (no small photodiode was present). The two calorimeter prototypes were tested in October 2012 and February 2013, respectively. The pre-prototype was tested with a muon beam of 150 GeV/c (see left of fig. 3.15) showing a signal due to MIPs which is clearly visible with a signal-to-noise ratio of 16.5. Ions with A/Z=2 at 30 GeV/n and 12.8 GeV/n were used in the prototype test beam. The results shows a good linearity of the response and the well resolved peaks of ^{2}H and ^{4}He in the first layer, with a signal-to-noise ratio of 14 for the deuterium peak, as showed on the right of fig. 3.15.

3.4 Other detectors

Besides the detectors described above, the GAMMA-400 scientific apparatus will comprise also two star sensors, with $\sim$5" accuracy, two magnetometers, mounted on telescopic booms, and six Konus-FG gamma-ray burst monitor, as visible on the top of fig.3.17. The Konus-FG will detect and promptly (1-2 s)

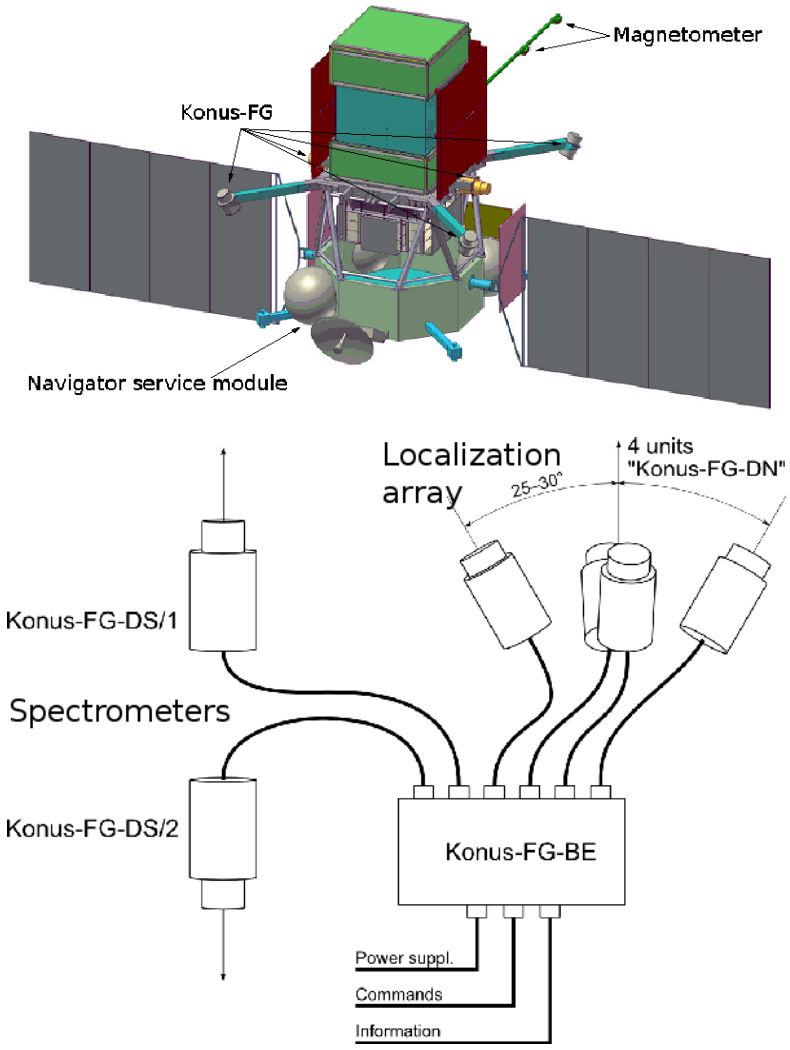

Figure 3.17: *Top:* GAMMA-400 mounted on the Navigator service module. The Konus-FG gamma-ray burst monitor (localization units on the corners of the apparatus, spectroscopic units on its sides), as well as the magnetometers, are shown. *Bottom:* schematic diagram of the Konus-FG instrument. Visible both the spectrometers and the localization array

localize gamma-ray burst (see sec. 1.3.3) with an accuracy of 0.5°-3° as well as study the temporal and spectral properties of the burst in the 10 keV - 15 MeV energy range. To achieve these goals four localization units and two spectrometric units, each with a 2π sr field-of-view, will be mounted on the satellite, arranged as shown on the bottom of fig. 3.17, ensuring an all-sky coverage.

3.5 Summary and comparison

In table 3.4 the characteristics of the GAMMA-400 tracker and calorimeter, in both configurations, are compared to the Fermi-LAT and AGILE ones. Fermi is bigger than both GAMMA-400 (of a factor 1.4) and AGILE (of a factor 3.7). This, together with the tungsten thickness that determines the ratio of converted gamma rays, affects directly the effective area, as shown in sec. 4.5.3. The tungsten thickness affects also, together with the pitch and readout method, the angular resolution, as presented in sec. 4.5.2. The calorimeter of GAMMA-400, regardless of the configuration, will be much deeper than the other two. The greater depth will help achieving a better energy resolution at high energy but also will produce a lot of backscattered particles that makes the direction reconstruction of highly energetic gamma rays more complex (see chap. 4.3).

		Fermi	AGILE	GAMMA-400	
				Baseline	Enhanced Configuration
Tracker	Dimension (cm^2)	~140×140	~38× 38	~97×97	~97×97
	Radiation Length	12 planes: 0.03 X_0 4 planes: 0.18 X_0 2 planes: no W	10 planes: 0.07 X_0 2 planes: no W	8 planes: 0.1 X_0 2 planes: no W	25 planes: 0.03 X_0
	Pitch (μm)	228	121	120	120
	Readout Pitch (μm)	228	242	240	240
	Readout	Digital	Analog	Analog	Analog
Calorimeter	Vertical R.L. (X_0)	8.6	1.5	23 (CC1 not included)	39
	Segmentation	96 Bars × Tower 2.7×2.0×32.6 cm^3	30 Bars 1.5×2.3×37.5 cm^3	9408 Cubes 3.6×3.6×3.6 cm^3	8000 Cubes 3.6×3.6×3.6 cm^3

Table 3.4: Comparison between the tracker and calorimeter of Fermi, AGILE and both versions of the geometry of GAMMA-400

Chapter 4

Direction Reconstruction and GAMMA-400 Performance Estimation

Differently from cosmic rays, charged particles deflected by magnetic fields, gamma rays arrive almost unimpeded to Earth. By analysing the direction and energy of a gamma ray, it is possible to study directly its source. The goodness of the study is thus directly proportional to the goodness of the reconstruction, which is a key feature to discriminate among different sources and to reveal different components inside extended sources. In this chapter the reconstruction algorithm for the two configurations (baseline and enhanced configuration) will be discussed and the results will be presented. The first part (sec. 4.1) will be dedicated to the Kalman filter, core of the reconstruction algorithm using information fro the tracker. Subsequently the calorimeter only track reconstruction will be presented in sec. 4.2 and how the obtained information are used in the overall, more precise reconstruction in sec. 4.3. The technique to exploit the long lever arm of the baseline will be presented in sec. 4.4, before the results and comparison (4.5) between both configurations and Fermi performance.

4.1 Kalman Filter

The track reconstruction in the tracker is performed by means of the Kalman filter technique, firstly proposed by Frühwirth [100]. The Kalman filter is an iterative method which uses a combination of prediction, filtering and smoothing to reconstruct the original direction of the incoming particle.
The impinging gamma ray, interacting with the tungsten in the tracker, creates

an electron-positron pair. The Kalman filter algorithm reconstructs the track of the two created particles and then infers the direction of the original photon. The multiple scattering as well as the distance of the planes and the uncertainty of the measurements, are taken in consideration in order to have a better reconstruction. The core of the distribution of the multiple scattering is approximately Gaussian with a projected width of [29]

$$\theta_{MS} = \frac{13.6\text{MeV}}{E[\text{MeV}]}\sqrt{z/X_0}[1 + 0.038\ln(z/X_0)] \tag{4.1}$$

where E is the energy of the particle (in MeV) and z is the thickness of the crossed material (in radiation length).
The important parameters for the measurement error are: the strip pitch, the readout method and the noise in the strips. The readout model greatly affects the error associated to the measure.
If the readout is analog the accuracy can be substantially improved if the signal charge is collected on more than one strip (due to charge diffusion) and the coordinate is determined by means of an interpolation method (e.g. center of gravity of the signal). The error depends on the noise in the strips through the equation [101]

$$\sigma = \frac{a_{cf} \cdot ENC \cdot p_a}{Q_s} \tag{4.2}$$

where a_{cf} is the so-called centroid finding constant, ENC is the Equivalent Noise Charge (amount of input charge that makes the signal-to-noise ratio equal to one), p_a is the amplifier pitch and Q_s is the signal charge. With a strip pitch of 120 μm, readout pitch of 240 μm, the error on the measure can be as little as 40 μm. The analog readout is presently used on the AGILE mission and, as stated in the previous chapter (sec. 3.2.1), it will be used also for the tracker of GAMMA-400.
In the case of a digital readout, such as the one used in the tracker of Fermi-LAT, no information are collected on the energy released in the Si and the error is always equal to $pitch/\sqrt{12}$ [101]. For Fermi-LAT the error on each measure is 228 μm$/\sqrt{12} \simeq 66$ μm.
At low energy the main contribution to the error in the reconstruction is related to the multiple scattering. As visible by eq. 4.1 the multiple scattering angle is large at low energy and the error is proportional to the radiation length of the material crossed. At high energies the multiple scattering becomes negligible and the measurement error starts to be dominant.
GAMMA-400 will not present a magnet and then the tracker will not provide a momentum measurement. The equations used by the Kalman filter are therefore simplified. Having a single-sided Silicon tracker, the two projections, in x and y,

are fitted separately. The formalism described in the following and in sec. 4.1.1 and 4.1.2, is based on the work by Frühwirth [100].
Information on the track at each layer are stored in a state vector. In this case the state vector for the i-th plane, $\boldsymbol{x}_i$ has two components: the position of the hit and the tangent of the angle of the track to the next layer. For each layer this system of equation is set:

$$\boldsymbol{x}_i = \boldsymbol{F}_{i-1}\boldsymbol{x}_{i-i} + \boldsymbol{w}_{i-1} \tag{4.3}$$

where $\boldsymbol{F}_{i-1}$ is the propagator from the plane i-1 to the plane i and $\boldsymbol{w}_{i-1}$ is a variable related to the multiple scattering. The propagator combines directional and position information to compute the position on the next level. Without a magnetic field it takes the form:

$$\boldsymbol{F}_{i-1} = \begin{pmatrix} 1 & d_{i-1,i} \\ 0 & 1 \end{pmatrix} \tag{4.4}$$

where $d_{i-1,i}$ is the distance between the plane i and the plane i-1. In the case of the configuration proposed by the Italian group, in which the tracker is homogeneous, the propagator is equal for each couple of planes. In the baseline the $\boldsymbol{F}$ matrix changes for the last planes which do not have any tungsten.
The measures performed on the i-th plane can be written as:

$$\boldsymbol{m}_i = \boldsymbol{H}_i\boldsymbol{x}_i + \delta_i \tag{4.5}$$

where $\boldsymbol{H}_i$ is the measurement matrix, in this case $\boldsymbol{H} = \begin{pmatrix} 1 & 0 \end{pmatrix}$ and δ_i is the measurement error.
The two uncertainties, multiple scattering and measurement, are described by as many covariance matrices. The covariance matrix related to the multiple scattering is:

$$\boldsymbol{Q} = cov(\boldsymbol{w}) = \begin{pmatrix} z^2\frac{\theta_{MS}^2}{3} & z\frac{\theta_{MS}^2}{2} \\ z\frac{\theta_{MS}^2}{2} & \theta_{MS}^2 \end{pmatrix} \tag{4.6}$$

where z is the thickness of the plane traversed and θ_{MS} is the multiple scattering angle, defined in 4.1. The measurement error is described by the matrix: $\boldsymbol{V} = \boldsymbol{G}^{-1} = cov(\delta_i) = (\sigma^2)$ where σ^2 is described, in the case of analog readout, by 4.2. A third covariance matrix is used to describe the uncertainty of the state vector: $\boldsymbol{C}_i = cov(\boldsymbol{x}_i - \boldsymbol{x}_i^{true})$.

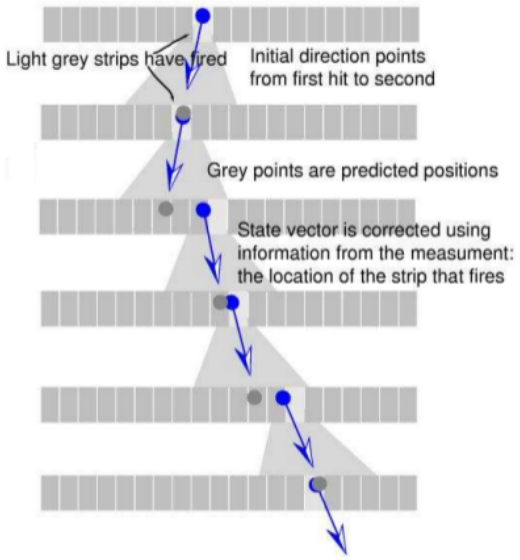

Figure 4.1: Filtering process of the Kalman filter [102].

4.1.1 Filtering Equations

The Kalman filter technique starts by predicting the position on the i-th plane based on the information of the previous plane. The predicted state vector is

$$\boldsymbol{x}_{i,proj} = \boldsymbol{F}_{i-1}\boldsymbol{x}_{i-i}, \tag{4.7}$$

to which an uncertainty, given by the sum of the predicted covariance and the effects of the multiple scattering, is associated in the form

$$\boldsymbol{C}_{i,proj} = \boldsymbol{F}\boldsymbol{C}_{i-1}\boldsymbol{F}^T + \boldsymbol{Q}_{i-1}. \tag{4.8}$$

Equation 4.7 and 4.8 describe an estimation of the state of the system at the plane i. If a measurement is present on the same plane, being it independent by the prediction, it can be used to refine the prediction. The filtered state vector will be

$$\boldsymbol{x}_i = \frac{(\boldsymbol{C}_{i,proj})^{-1}\boldsymbol{x}_{i,proj} + \boldsymbol{H}^T\boldsymbol{G}_i\boldsymbol{m}_i}{(\boldsymbol{C}_{i,proj})^{-1} + \boldsymbol{H}^T\boldsymbol{G}_i\boldsymbol{H}} = \boldsymbol{C}_i[(\boldsymbol{C}_{i,proj})^{-1}\boldsymbol{x}_{i,proj} + \boldsymbol{H}^T\boldsymbol{G}_i\boldsymbol{m}_i], \tag{4.9}$$

where the filtered covariance matrix for the i-th plane was defined as

$$\boldsymbol{C}_i = [(\boldsymbol{C}_{i,proj})^{-1} + \boldsymbol{H}^T\boldsymbol{G}_i\boldsymbol{H}]^{-1}. \tag{4.10}$$

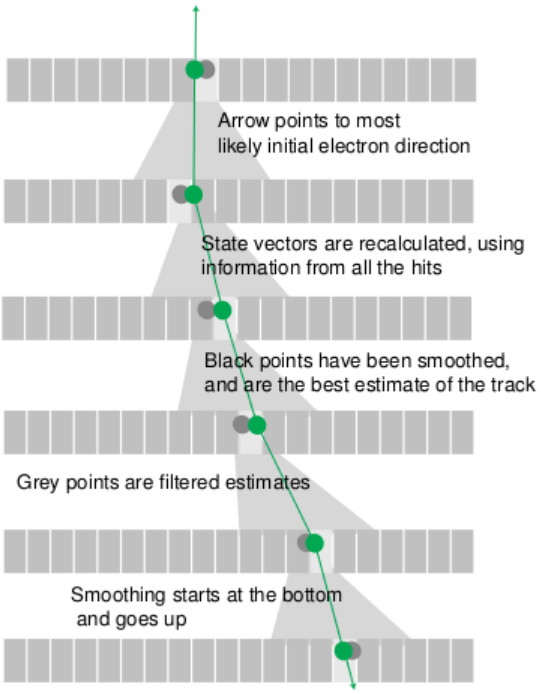

Figure 4.2: Smoothing process of the Kalman filter [102].

A weight for each measurement is defined as the distance between the measured hit and the predicted position. In the case of more than one hit on the same plane, the hit with the lowest weight value is chosen as the one belonging to the track.
As it can be seen by these equations, the extent to which a new measure adds more information to the reconstruction is weighted by the inverse of the measurement error. The error on the position of the hits on the Si planes of the tracker is $\sim 40\mu$m while the hits in the calorimeter are known with an accuracy comparable to half of the cube side (1.8 cm). This is one of the reasons why, as more thoroughly discussed in section 4.3, simply adding the hit position in the calorimeter to the Kalman filter does not improve the result.
The subsequent use of prediction and filtering can be used on all the consecutive planes. The state vector related to the last plane will inherit all the information from the previous planes. A schematic view of the process is presented in fig. 4.1.

4.1.2 Smoothing Equations

The smoothing phase brings the information from the last plane to the first, furtherly refining it, thus reconstructing the direction of the impinging particle.

First a gaining matrix is defined as

$$\boldsymbol{A}_i = \boldsymbol{C}_i \boldsymbol{F}_i^T (\boldsymbol{C}_{i+1,proj})^{-1} \tag{4.11}$$

The smoothed state vector for the plane i will be

$$\boldsymbol{x}_{i,smooth} = \boldsymbol{x}_i + \boldsymbol{A}_i(\boldsymbol{x}_{i+i,smooth} - \boldsymbol{x}_{i+i,proj}) \tag{4.12}$$

and its covariance matrix

$$\boldsymbol{C}_{i,smooth} = \boldsymbol{C}_i + \boldsymbol{A}_i(\boldsymbol{C}_{i+1,smooth} - \boldsymbol{C}_{i+1,proj})\boldsymbol{A}_i^T \tag{4.13}$$

Iterating the smoothing phase to the first plane it will give the initial inclination of the track, as seen in fig.4.2.
The Kalman filter also gives a parameter which indicates the quality of the fit by defining a residual and a weight for each plane. The residual vector for the plane i is

$$\boldsymbol{r}_i = \boldsymbol{m}_i - \boldsymbol{H}\boldsymbol{x}_{i,smooth} \tag{4.14}$$

The covariance matrix of the residuals, which again depends on both the multiple scattering and the measurement error, takes the form

$$\boldsymbol{R}_i = \boldsymbol{V}_i - \boldsymbol{H}\boldsymbol{C}_i\boldsymbol{H}^T \tag{4.15}$$

The χ^2 of a single plane is then $\chi_i^2 = \boldsymbol{r}_i^T \boldsymbol{R}_i^{-1} \boldsymbol{r}_i$. The total χ^2 of the track can be obtained by summing the χ^2 of all the planes. The χ^2 value is used to reject tracks results of a bad reconstruction (see for example fig. 4.3).

4.1.3 Implementation

The Kalman filter in GAMMA-400 is implemented in the framework code in the same way it is used for the reconstruction algorithm of AGILE [103].
One of the most important, and most difficult, task of the track reconstruction is the identification of the vertex, the first hit of the electron-positron pair created by the gamma ray. This duty is particularly difficult at high energies where the number of hits produced by backsplash particles is considerable. In GAMMA-400 this task is accomplished using the very same Kalman filter later used to reconstruct the track itself.
The Kalman filter is used on every possible combination of hits on the first two planes, an example of the possible combinations is shown in fig. 4.4. The couple of hits whose track has the least χ^2 is chosen as the vertex. At high energy the process is helped by information from the calorimeter as more thoroughly discussed

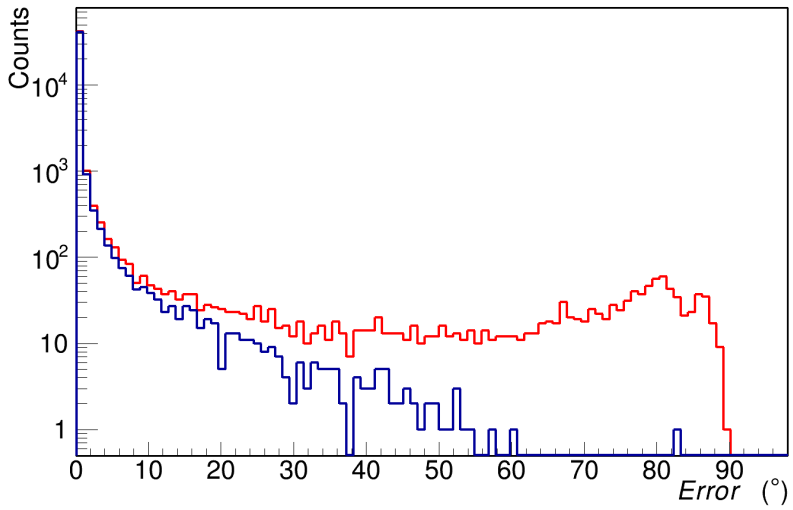

Figure 4.3: Dependence of the error from the χ^2 of the reconstructed track. In red the error of all the reconstructed events for a 5 GeV gamma ray interacting with the baseline, in blue only the events that passes a cut on the χ^2 (χ^2 of each track less than 100)

in section 4.3.
Once the vertex is identified, the Kalman filter is again used to reconstruct a total of two, one per particle, tracks per view. The choice of the same hit for two different tracks is disfavoured by applying a weight. During this process the energy of the particle is estimated using the multiple scattering. As stated in the previous chapter, and visible in eq. 4.6, the goodness of the track reconstruction depends on the knowledge of the multiple scattering which in turn depends on the estimation of the particle energy. Once a first iteration, with a fixed energy, of the track reconstruction is performed, the variation of the inclination of the track is computed. This variation provides an indication of the intensity of the multiple scattering. Knowing the radiation length of a plane and reversing eq 4.1, it is possible to estimate the energy of the particle. If this estimation is a factor of 3 different, bigger or smaller, from the energy used in the iteration to reconstruct the track, a new reconstruction is performed using the energy just estimated.

The results of the aforementioned process are four tracks: one for each particle, e^- and e^+, for each view. It is necessary to combine the tracks corresponding to the same particle in different views. Geometrically an ambiguity arises in which, as seen on the left of fig. 4.5, two possible combinations, and consequently two possible three dimensional tracks, are both solution of the combination of the two views. The energy estimation described above is used to discriminate between

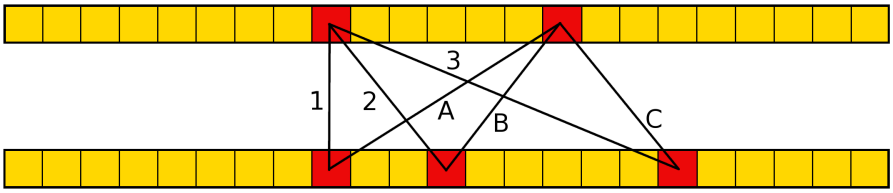

Figure 4.4: Two Si planes with hit strips (in red). The possible combination first-second plane used at the beginning of the implementation of the Kalman filter are shown. For two hits on the first plane and three for the second the combinations are six: three (1,2,3) for the first hit on the first plane and three (A,B,C) for the second hit of the first plane

these two cases: the most energetic track in one view is associated to the most energetic track in the other view in order to obtain the right solution [104].

Once the three-dimensional tracks of the e^- / e^+ pair are computed, the original gamma-ray direction is obtained as the bisector of the tracks, using a simple sum of the components of the two, weighted on their corresponding energy. Using for the reconstruction the bisectors of the two tracks in the separate views instead, could lead to an error for all the off-axis events, as seen on the right of fig. 4.5 [104]. The weighting on the energy is necessary, particularly at very high energy where the probability of an uneven division of the energy in the pair is not negligible, as visible in fig. 4.6.

4.2 Calorimeter reconstruction

Information from the calorimeter alone can be used to reconstruct the original direction of the incoming gamma ray. Thanks to its novel configuration (see sec. 3.2.2 and 3.3.2), the calorimeter of GAMMA-400, in both the presented configurations, is capable to reconstruct the track of gamma rays coming both from the top and from the side of the detector. This capability increases greatly the effective area and the geometrical factor of the instrument. As it will be seen in the following, the angular resolution of the calorimeter only reconstruction is worse than the reconstruction performed using the tracker, mainly because of the larger pitch. The inferred information can nonetheless be useful as a trigger for a repointing of the instrument, a trigger for further observations from telescopes on the ground or as a help to refine the reconstruction in the tracker, as it will be discussed in the next section.

The reconstruction in the calorimeter does not use a Kalman filter, as the one in the tracker, but uses a least square weighted fit. At least three hit planes are

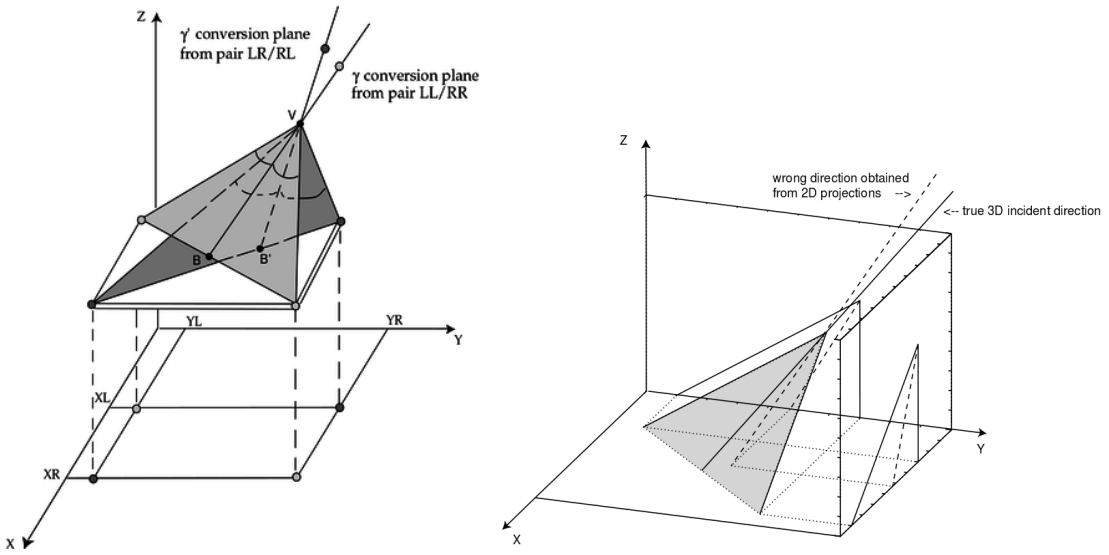

Figure 4.5: *Left*: Ambiguity related to the lack of knowledge of the corresponding track in each view [104]. *Right*: difference between the bisector of the two three dimensional tracks and the reconstructed bisector [104].

required in order for the fit to converge. This constraint leads to a need of a lot of energy release and thus a better reconstruction at high energies. In this analysis an energy deposit in the calorimeter of at least 8 GeV is used as condition for the reconstruction in order to ensure a good angular resolution and effective area. Since the calorimeter is able to reconstruct the incident direction also for particles coming from the sides of the detector, an initial estimation of the track is needed in order to define the inclination of the planes. As an example, if the gamma ray is coming from the top, the planes used in the fit will be horizontal, while if the gamma ray is coming from the side ($\theta = 90°$ for the sake of the example) the planes will be vertical. The inclination of the planes is defined as perpendicular to the line result of the fit using the three cubes with the highest energy release. The wrong choice of the inclination of the planes could lead to a large error in the reconstruction. The inclination of the planes varies with $\pi/4$ steps, as shown in fig. 4.7.

Once the inclination of the planes is found, the barycenter is calculated for each plane. A separate fit for each view of the function $x = Az + B$ is then performed. A and B are respectively

$$A = \frac{\sum_i x_i z_i \omega_i - \sum_i x_i \omega_i \sum_j z_j \omega_j}{\sum_i z_i^2 \omega_i - \left(\sum_i z_i \omega_i\right)^2} \qquad B = \frac{\sum_i x_i \omega_i \sum_j z_j^2 \omega_j - \sum_i z_i \omega_i \sum_j x_j z_j \omega_j}{\sum_i z_i^2 \omega_i - \left(\sum_i z_i \omega_i\right)^2}, \tag{4.16}$$

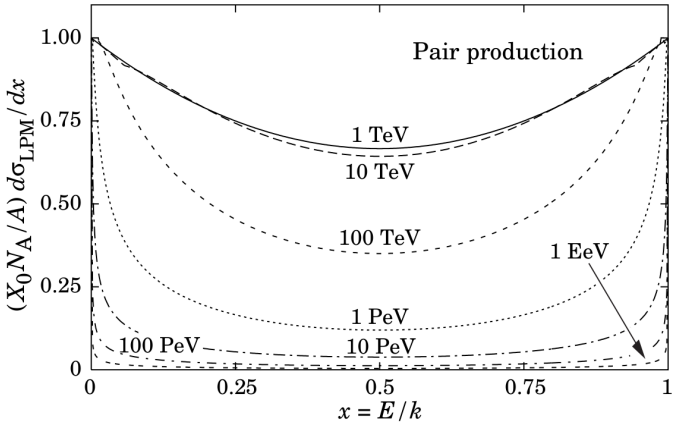

Figure 4.6: The normalized pair production cross section versus fractional electron energy [29]

where, for the i-th layer, x_i and z_i are the coordinates of the hit cubes and the weight ω_i is the energy release in the layer divided by the total energy release in all the layers in that view ($\omega_i = E_i/E_{tot,view}$).
The above procedure is iterated several times excluding the farthest points from the computed track. Each time the center of gravity on a plane is recalculated using only the five cubes closest to the track previously estimated. The weight in this case is $\omega_i = E_i/\sum_i E_i$ to maintain $\sum_i \omega_i = 1$. This process leads to the calculation of the track projection in the two views. The three dimensional angles are given by: $\theta = \arctan(\sqrt{A_x^2 + A_y^2})$ and $\phi = \arctan(A_y/A_x)$ where A_x and A_y are the inclinations found in the x and y view respectively. If the plane used is not horizontal, a counter-rotation is then operated in order to retrieve the original incoming direction of the particle. Various information on the development of the shower, e.g. its centroid position and the length of its semi-axis, are also calculated in order to be used to refine the reconstruction in the tracker. The different procedure eliminates the ambiguity in the track reconstruction, described in sec. 4.1.3, because the reconstructed track is directly the one associated to the gamma ray and not the one associated to the produced pair. Indeed, the high energies required for the procedure, which results in low multiple scattering and large showers, lead to an impossibility to discriminate between the shower created by the electron and positron.
If the particle is coming from above the detector, the information from the vertex in the tracker can be use to further refine the reconstruction. The resulting angular error will be still worse than the one calculated using the Kalman filter, but the newly, more finely computed shower information are useful in the joint reconstruction (see chap. 4.3). The vertex is added in each view with a weight

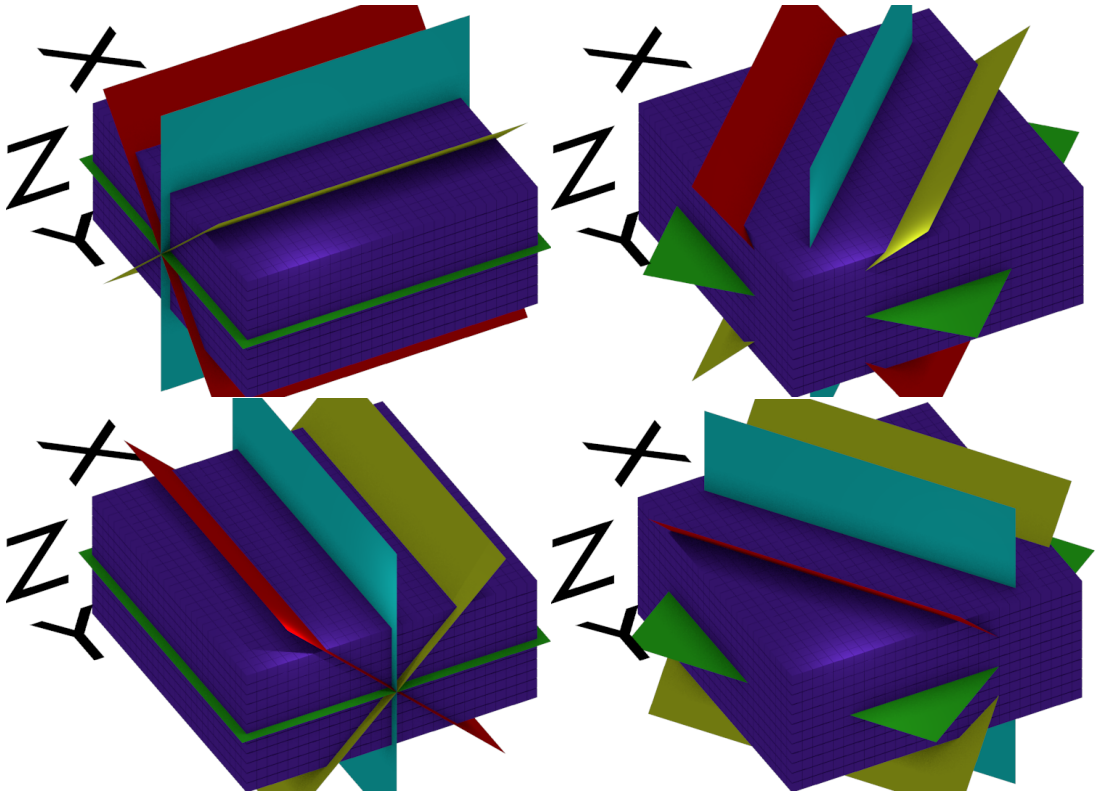

Figure 4.7: Inclination of the planes defined to allow the reconstruction of the shower from particles coming also from the side of the calorimeter. In purple the calorimeter of the baseline. Depending on the gamma-ray incoming direction, the planes can be: horizontal (in green, for gamma rays with $\theta = 0°$), inclined with an angle θ of $\pi/4$ or $3\pi/4$ (yellow or red) or vertical (cyan). The ϕ of the plane can also vary with $\pi/4$ steps: 0 (*top left*), $\pi/4$ (*top right*), $\pi/2$ (*bottom left*), $3\pi/4$ (*bottom right*).

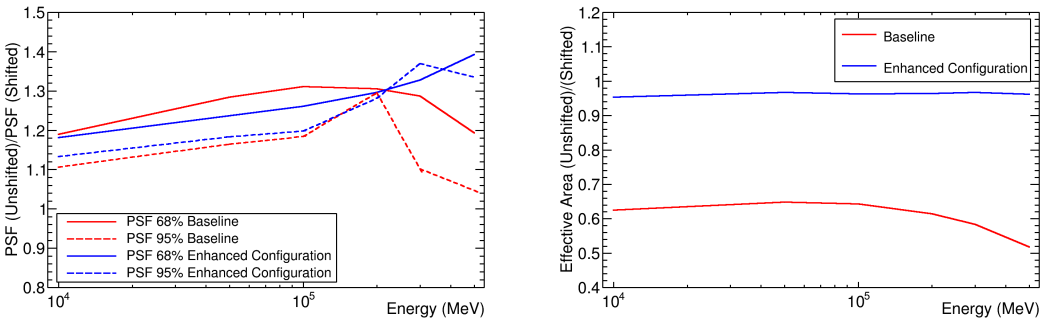

Figure 4.8: Ratio between the values of the PSF (*left*) and effective area (*right*) of the calorimeter with unshifted planes and with an horizontal shift between different planes for both the baseline (in red) and the enhanced configuration (in blue). The solid lines refer to the PSF 68% while the dashed lines to the PSF 95%

defined as

$$\omega_{TRK} = \sqrt{\frac{P_c}{P_s}\frac{H_{CAL}}{H}} \cdot \frac{1}{N}, \tag{4.17}$$

where P_c is the side of one of the calorimeter cubes (3.6 cm), P_s is the pitch of the strip in the tracker (120 μm), H_{CAL} is the total height of the calorimeter, H is the distance between the vertex and the bottom of the calorimeter and N is the number of points used (number of planes hit in the calorimeter plus the vertex in the tracker). In order to maintain $\omega_{TRK} + \sum_i \omega_i = 1$, the weight on the point in the calorimeter is now defined as $\omega_i = (1 - \omega_{TRK})E_i / \sum_i E_i$. The process is then identical to the one described before.
As mentioned in chap. 3.3.2, it is possible to horizontally shift the planes of the calorimeter to increase the angular resolution and effective area for normally incident particles. Without the shift the shower produced by particles with normal incidence would be poorly mapped by the calorimeter because of the lined up gaps. Some of the particles could also escape the detector without interacting. A slight shift of the planes in the x-y direction can close the gaps, allowing a better reconstruction of the shower, and consequently of the direction, and an improvement in the number of detected particles. As shown on the left of fig. 4.8, the improvement of the PSF (Point Spread Function, PSF N% is defined as the angle in which the N% of the events coming from a point source are enclosed) is of the order of ~ 1.2 for both geometries. The improvement of the effective area, shown on the right of fig. 4.8 is instead moderate for the enhaced configuration, a factor ~ 1.05, while more substantial, a factor of 2, in the case of the baseline.

4.3 Joint reconstruction

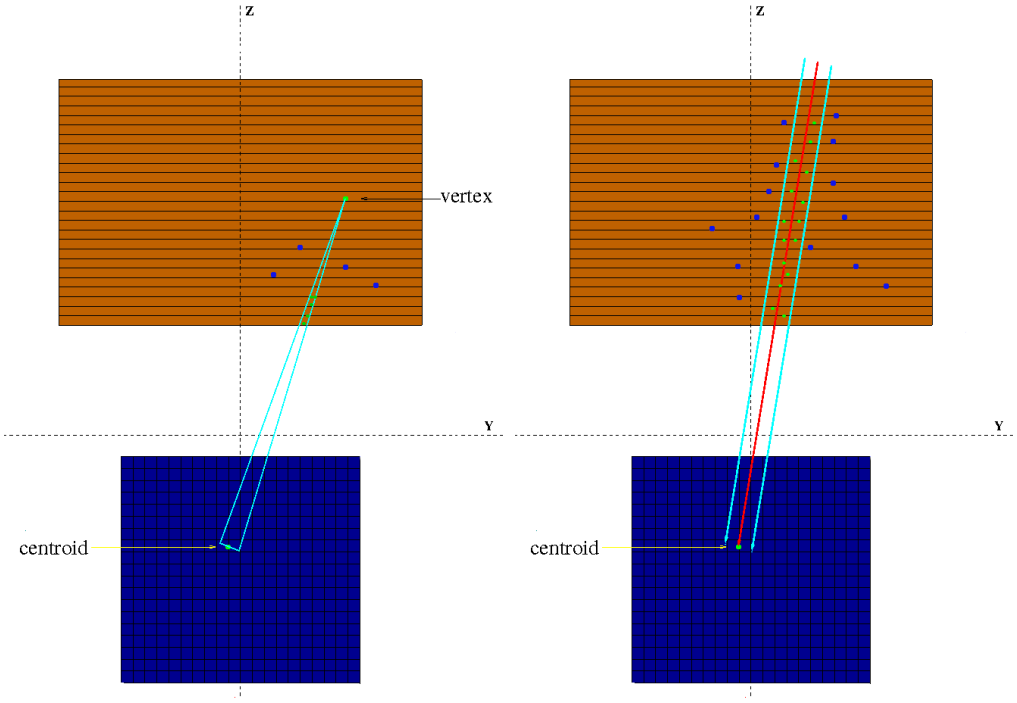

Figure 4.9: Calorimeter seeded selection of hits for track reconstruction. *Left:* The base of the triangle, whose height is the vertex-centroid connector, is equal to the side of one of the cube in the calorimeter. A penalty is applied to the blue hits outside the triangle, no penalty to the green hit inside the triangle. *Right:* The red line is the direction reconstructed using only information from the calorimeter, the two cyan lines are parallel to it. The distance between the two cyan lines is equal to the side of one cube in the calorimeter. A penalty is applied to the blue hit outside the two lines, no penalty to the green hit inside the lines.

For energies greater than 10 GeV the use of the Kalman filter with information from the tracker alone to reconstruct the track is made difficult by the large amount of backscattered particles. Additional information are then needed in order to select more efficiently the right hits to use. Since at high energies the multiple scattering is negligible, the information in the calorimeter can be used to help this selection.
Information from the calorimeter are used in different part of the implementation of the Kalman filter:

- As said in chapter 4.1, the Kalman filter relies on an estimation of the energy

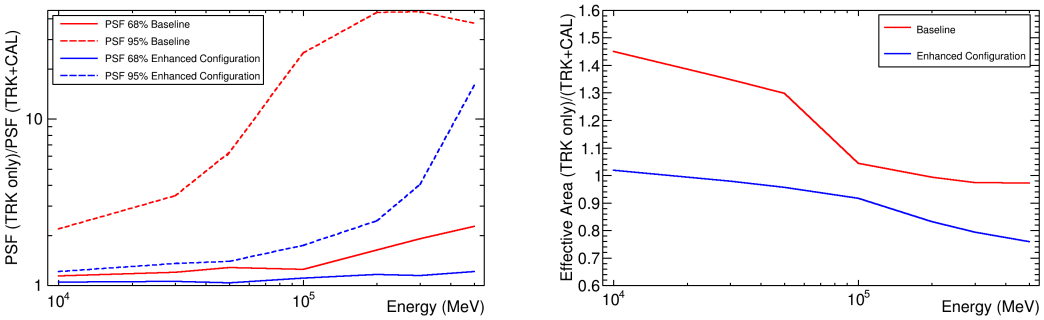

Figure 4.10: Ratio between the values of the PSF (*left*) and effective area (*right*) computed using only information from the tracker and the joint reconstruction (tracker plus calorimeter) for both the baseline (in red) and the enhanced configuration (in blue). The solid lines refer to the PSF 68% while the dashed lines to the PSF 95%

of the particle for the goodness of the fit. The information on the energy released in the calorimeter is used both in the search of the vertex and in the subsequent fit.

- An energy release in the calorimeter means that at least one of the particles created by the gamma ray in the tracker has reached the calorimeter itself. Once the vertex is found, the number of planes used to fit the tracks is set up to the last plane before the calorimeter. Usually this number is at most seven because at low energy, in a multiple scattering dominated regime, the use of more planes in the fit does not help the reconstruction, it rather worsen it.

- The position of the centroid of the shower can be used, together with the vertex in the tracker, in order to help the selection of the right hits for the reconstruction (see fig. 4.9 left). A triangle is built in each view, the base of which is equal to the side of one of the cubes of the calorimeter. A weight is given to hits outside the triangle, proportional to the distance from the boreder of the triangle itself. The weight is then used in the Kalman filter, summed to the distance between the measured and projected hit (see sec. 4.1.1), in order to disfavour the choice of hit outside of the triangle. The reconstructed direction in the calorimeter is not used at this point since its error is considerable and the error on the position of the vertex is much less than the error on the position of the calorimeter (40 μm for the tracker, 1.8 cm for the calorimeter), given for granted that the vertex is found correctly.

- If a considerable (more than 100 GeV) amount of energy is released in the

calorimeter from a gamma ray, then one can presume that at least one of the reconstructed tracks should cross the reconstructed shower in the calorimeter. If none of the tracks cross the shower then a new iteration of the Kalman filter is used, if that fails then the event is considered not reconstructed. Before this new iteration a weight is applied to all the clusters, potential vertexes included, similarly to what mentioned before. Here the weight is given not by the distance from a triangle but from two parallel lines (see right of fig. 4.9). The distance between these two lines is the side of a cube and the inclination is given by the direction reconstructed by the calorimeter alone.
For energies between 10 and 100 GeV the reconstruction of the shower in the calorimeter could be imprecise. At these energies the condition applies to the crossing of the calorimeter in its entirety rather than the shower. The calorimeter of the baseline, being wider, provides a less effective cut on the error than the one in the enhanced configuration but allows the reconstruction of more events.

The improvement in the angular resolution (PSF) are shown on the left of fig. 4.10. The joint reconstruction is particularly effective in the suppression of the tails of the error distribution, which are included in the PSF 95%. The rising at higher energies is related to the increase of the number of events with backsplashed particles from the calorimeter. To the improvement on the angular resolution corresponds a worsening of the effective area, as shown on the right of fig. 4.10. While some events are better reconstructed using also the calorimeter, others are lost because related to gamma rays converting in the calorimeter or in the last planes of the tracker. In this case the reconstruction using only information from the tracker can mistake the hits from backsplashed particles as hits from the e^+/e^- pair, leading to a great error on the direction. The loss in effective area is in any case modest compared to the gain in angular resolution.
This reconstruction using information from both the tracker and the calorimeter is found to be the best for the enhanced configuration but not for the baseline, as it will be discussed in the next section.

4.4 Pre-shower reconstruction

At low energies (less than 10 GeV) the reconstruction in the baseline uses the same approach described in the previous chapters, a combination of the Kalman filter and information from the calorimeter. At higher energies the information from the pre-shower can be used to improve the results of the reconstruction. The idea is to exploit the long lever-arm between the tracker and the Silicon planes

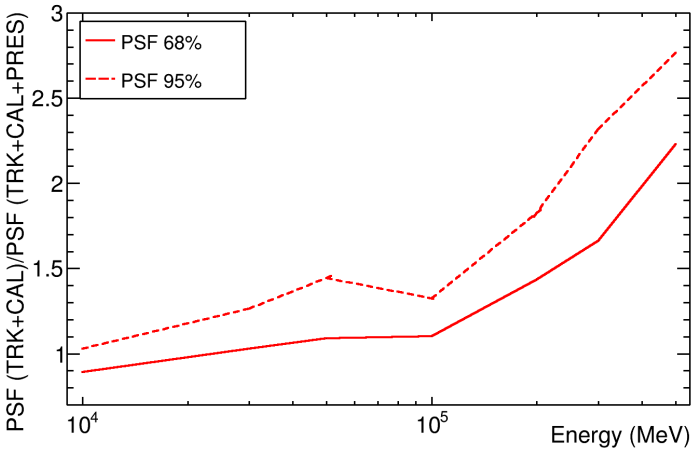

Figure 4.11: Ratio between the values of the PSF computed using the joint reconstruction described in chap. 4.3 and the reconstruction using also the pre-shower.

inside the CC1. Having the CsI before the Silicon and being so close to the CC2, the problem is to find the right hit, ruling out the noise derived from backsplashed particles and from particles created by the start of the shower. A particularly effective, and simple, way to identify the cluster where the particles passed is to compute a median weighted on the energy released in the clusters of few adjacent strips. Once the points on the two planes of the CC1 in each view and the vertex, using the Kalman filter, are found, a simple fit of a straight line of the form $x = mz + q$ is performed. In this case, having all the points the same weight, m and q are defined as:

$$\begin{aligned} m &= \frac{3\sum_i(x_i z_i) - \sum_i x_i \sum_i z_i}{3\sum_i z_i^2 - (\sum_i z_i)^2}, \\ q &= \frac{\sum_i x_i (z_i)^2 - \sum_i z_i \sum_i (x_i z_i)}{3\sum_i z_i^2 - (\sum_i z_i)^2}, \end{aligned} \tag{4.18}$$

3 being the number of points used: the vertex in the Tracker plus the two points in the CC1. Once the track is fit the calculation is iterated excluding the clusters outside a cylinder centered on the computed track, similarly to the process used in the calorimeter only reconstruction.
The higher the energy, the greater is the improvement of this technique related to the Kalman filter, as seen in fig. 4.11. The reason for this behaviour is that at high energies the identification of the hit in the pre-shower is more efficient thanks to the higher energy of the pair. This method reconstructs one single direction,

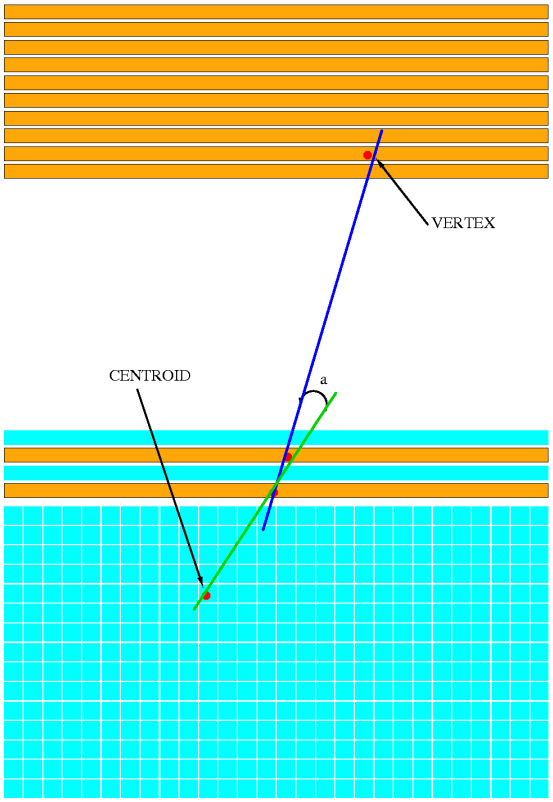

Figure 4.12: The blue line is the direction reconstructed using the vertex in the tracker and the two planes of the CC1. The green line is the direction reconstructed using the centroid in the calorimeter and the two planes of the CC1. a is the angle between the two.

the direction of the gamma ray, rather than reconstructing primarily the direction of the pair. A χ^2, calculated as

$$\chi^2 = \frac{\sum_i (x_i - (mz_i + q))^2}{3}, \tag{4.19}$$

is associated to the reconstruction in each view, giving an estimation of the goodness of the fit. There is the possibility that the reconstruction using the Kalman filter is more precise than the result of this fit. Using the value of the χ^2 it is possible to identify such events. The cases in which the results of the Kalman are used are not the results of theoretical calculations but of studies on the output of the reconstruction. These cases are:

- The χ^2 in eq. 4.19 of the track in either view is higher than 1.7.

- The χ^2 in eq. 4.19 is higher than the χ^2 related to the tracks found using the Kalman filter.
- The angular distance between the fitted line and the line results of the fit between the two points in the pre-shower and the centroid of the shower in the calorimeter is higher than 5° (angle "a" in fig. 4.12). This is the case in which one between vertex and the points in the pre-shower are found wrongly.

The difference between the error result of the application of the Kalman filter and the result of the pre-shower reconstruction after applying these conditions are shown in fig. 4.13. The distributions tending to negative numbers represent the improvements achieved by applying these conditions. The reconstruction for the baseline at high energy is therefore a hybrid between the Kalman filter and a fit, depending on the case.
Even without the vertex, a straight line passing through the two points in the CC1 is a good approximation to the original direction of the gamma ray. This kind of events, in which the Kalman filter fails to provide the position of the vertex and thus the reconstruction, can be used to improve the effective area of the instrument.

4.5 Results and comparison of the geometries

In this section an estimate of the GAMMA-400 performance obtained using the methods explained above will be presented. The angular resolution will be presented in chap. 4.5.2, the effective area in chap. 4.5.3 and the sensitivity in chap. 4.5.4. In each part the results for both configurations, baseline and enhanced, and a comparison between the two, will be presented.

4.5.1 Simulation set-up

Simulations of the apparatus and its response to the passage of gamma rays are performed by means of Geant4 [99]. Geant4 is a toolkit to simulate the passage of particles through matter. After a description of the apparatus, including sensitive parts as well as dead areas and supports, is provided, the gamma rays are simulated as a mono-energetic beam (50, 100, 200, 300 and 400 MeV and 1, 5, 10, 30, 50, 100, 200, 300, 500 GeV) with all the particles having the same direction (theta, the polar angle, equal to 1°, 10°, 30° and 45° and phi, the azimuthal angle, equal to 0°, 30° and 45°). The sources are distributed above the detector on a rectangle just big enough to illuminate uniformly the overall apparatus in order to optimize the

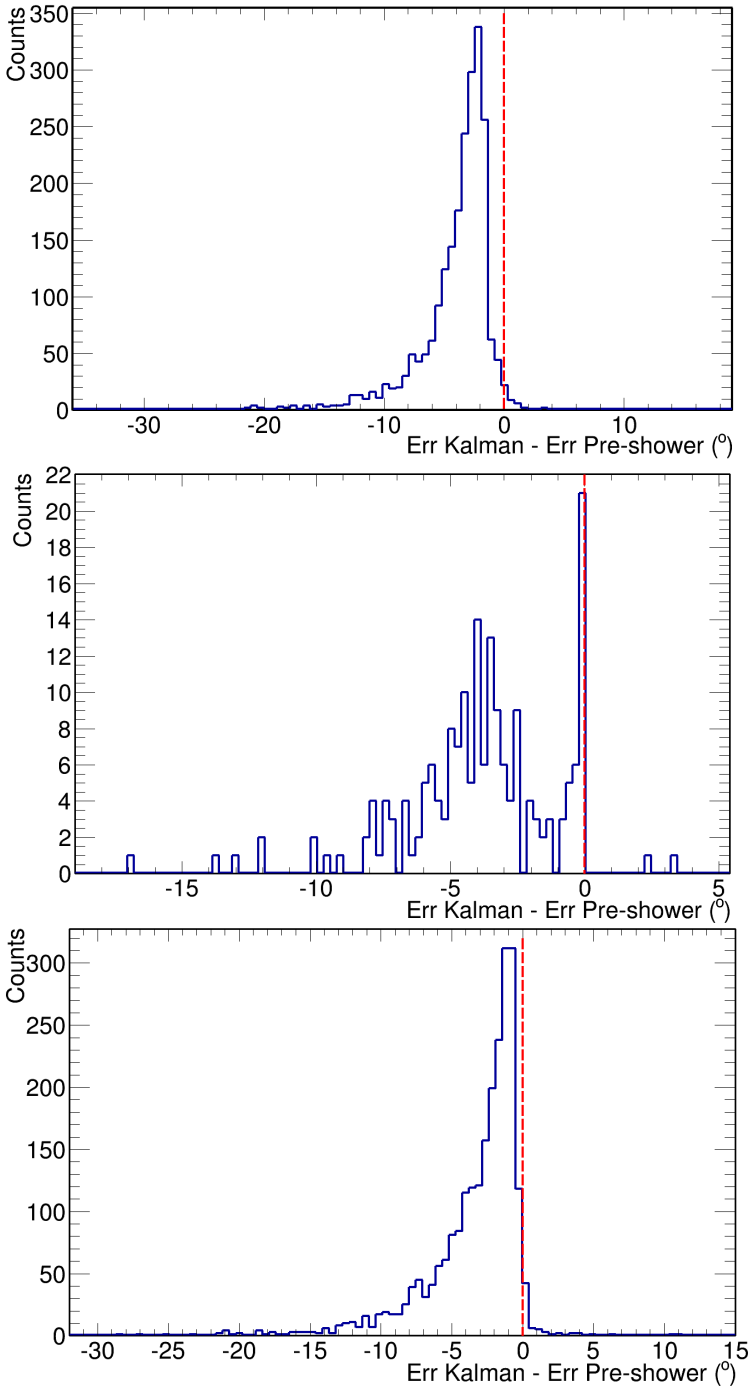

Figure 4.13: Difference between the error result of the application of the Kalman filter and the result of the pre-shower reconstruction after applying the conditions described in the bulleted list in chap. 4.4 for a 10 GeV gamma ray. From top to bottom: χ^2 greater than 1.7 in either view, χ^2 in eq. 4.19 is higher of the χ^2 related to the tracks found using the Kalman filter, angle "a" in fig. 4.12 greater than 5°. The dashed line corresponds to the zero.

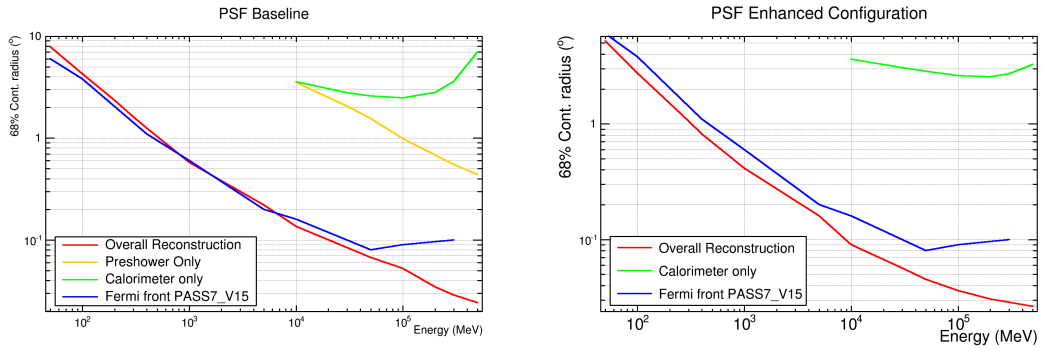

Figure 4.14: Comparison between the PSF 68% of the baseline (*left*) and enhanced configuration (*right*) and the PSF 68% of Fermi front (in blue). In red the PSF results of the overall reconstruction (using the combination of information from the tracker and the other instruments), in yellow the results of the pre-shower only reconstruction and in green the results of the calorimeter only reconstruction. These last two type of reconstruction are performed only in the case of a failed overall reconstruction.

simulation time. For each energy-angle combination, 300000 events are simulated. This number of events provides a sufficient statistic for the performance estimation, even when the reconstruction efficiency is taken in consideration. In the following, unless stated otherwise, all the results are obtained from simulation of gamma rays arriving with an angle theta equal to 1° and phi equal to 0°.

4.5.2 PSF

The Point Spread Function (PSF) describes the response of a system to the signal generated by a point source. It provides an estimation of the angular resolution of the instrument. Two point sources are indistinguishable if their distance is less than the PSF. The PSF N% is defined as the angle in which the N% of the events coming from a point source are enclosed. The PSF 68% and 95% will be presented.
The results of the best possible reconstruction for each geometry is shown in fig. 4.14 labelled as overall reconstruction. The results of GAMMA-400 are compared with the performance of Fermi front. At low energy the enhanced configuration has a better angular resolution than the baseline thanks to the thinner tungsten, and consequently less multiple scattering. Thanks to the different readout, the enhanced configuration has also a better PSF at low energy than Fermi. Thanks to the analog readout the baseline has an angular resolution comparable with Fermi front at low energy, even with a tungsten thickness more than doubled with re-

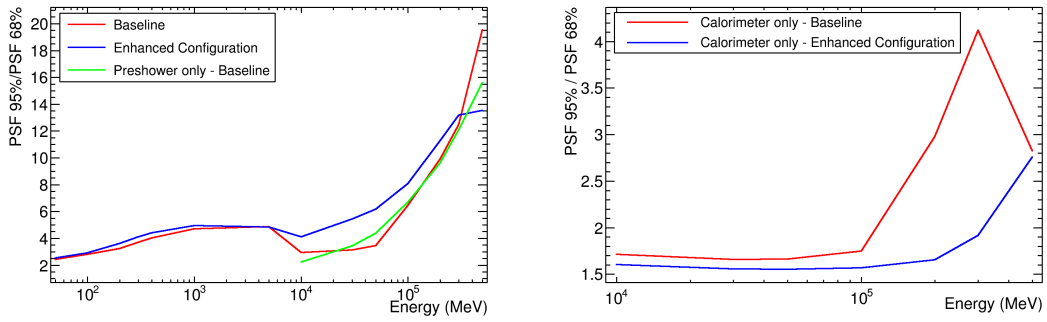

Figure 4.15: Ratio between the PSF 95% and the PSF 68% at 1° in theta and 0° in phi for the overall reconstruction and the pre-shower (*left*) and the calorimeter (*right*) of the two configurations.

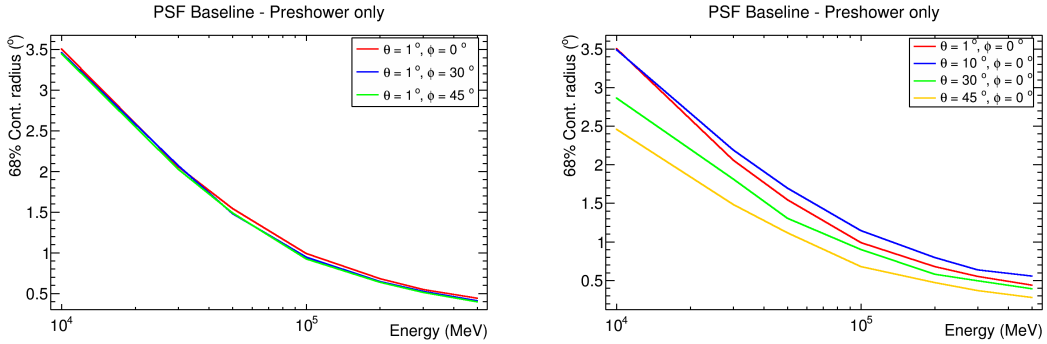

Figure 4.16: Comparison between the pre-shower PSF 68% at various phi (*left*) and theta (*right*). The reconstruction is performed only in the case of a failed overall reconstruction.

spect to it. At high energies both configurations show an improvement over the Fermi angular resolution thanks to both the analog readout and the use of information from the calorimeter and the pre-shower. The enhanced configuration has a PSF comparable to the baseline at high energy (0.026° against 0.024° at 500 GeV) thanks to the smaller calorimeter, and consequently less contribution from backsplashed particles. As an example, out of the total number of reconstructed events at 500 GeV (theta 1°, phi 0°), 99.98% cross the calorimeter in the baseline whereas only 53.6% cross the calorimeter of the enhanced configuration. The PSF 68% and 95% using only the events that cross the calorimeter in the enhanced configuration are 0.032° and 0.548° respectively, while they are 0.019° and 0.157° for events that do not cross the calorimeter. Another consequence of the smaller calorimeter of the enhanced configuration is that for 46.4% (at 500 GeV, theta 1°,

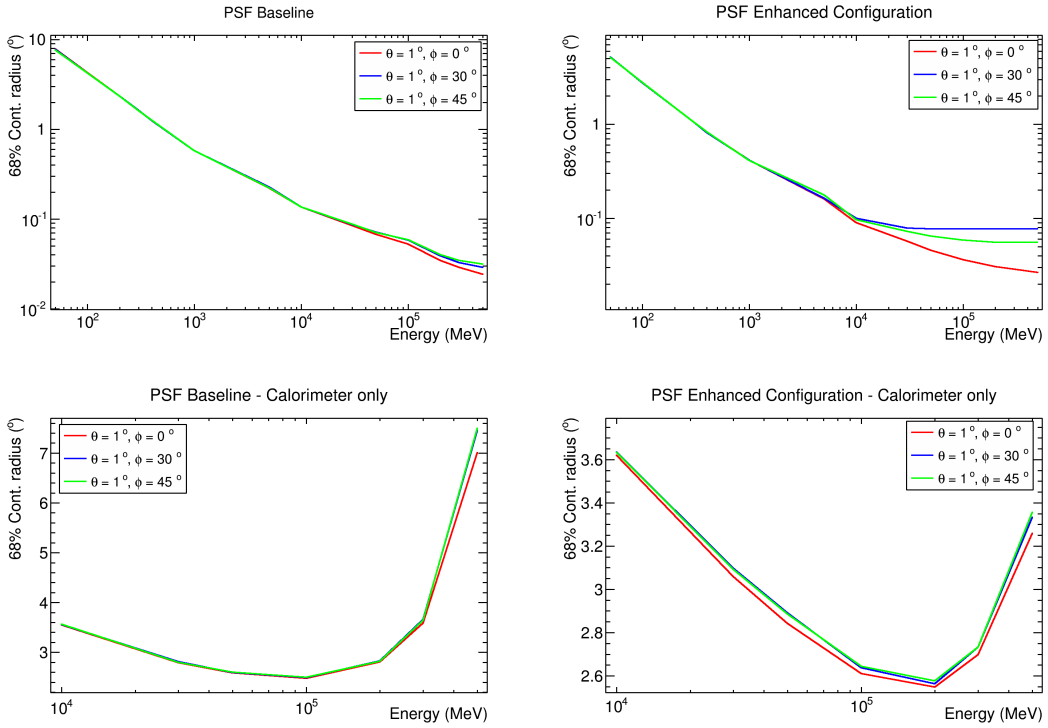

Figure 4.17: Comparison between the PSF 68% of the baseline (*left*) and enhanced configuration (*right*) for the overall reconstruction (*top*) and the calorimeter only reconstruction (*bottom*) for different phi and theta equal 1°. The calorimeter only reconstruction is performed only in the case of a failed overall reconstruction.

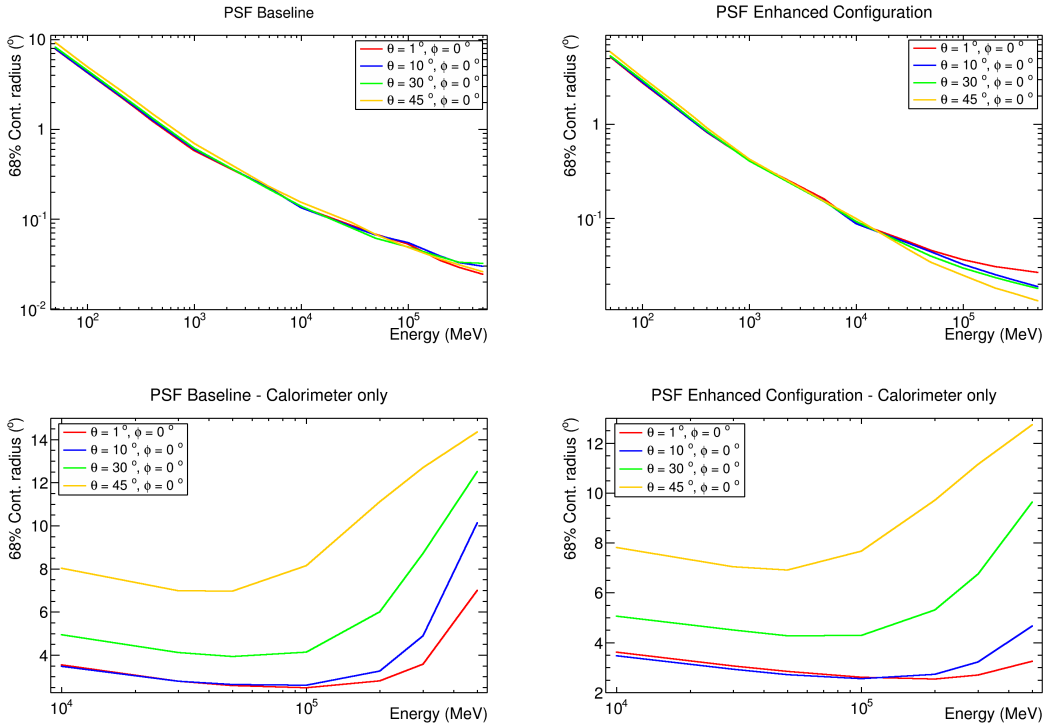

Figure 4.18: Comparison between the PSF 68% of the baseline (*left*) and enhanced configuration (*right*) for the overall reconstruction (*top*) and the calorimeter only reconstruction (*bottom*) for different theta and phi equal 0°. These calorimeter only reconstruction is performed only in the case of a failed overall reconstruction.

phi 0°) of the events the estimation of the energy has to rely only on the tracker. The events that contributes to the calorimeter only and pre-shower only PSF are the events lacking of an overall reconstruction. The overall reconstruction is indeed better and these other events are used to improve the effective area rather than the angular resolution.
The PSF calculated using only information from the calorimeter is of the order of 3° for both configuration, as shown in fig. 4.14. The different depth of the two detectors starts to have an effect at energies higher than 300 GeV for which the calorimeter of the baseline starts to have difficulty in containing the shower, thus leading to a worsening of the PSF.
The ratio of the PSF 95% and the PSF 68% for both configurations and all the different detectors is presented in fig. 4.15. The ratio increases at higher energies for all the detectors because of the bigger tails of the distribution at high energies. The drop at 10 GeV for the overall reconstruction is related to the use of the information from the pre-shower and the calorimeter. The fact that it is more prominent for the baseline is related to a better suppression of the tails of the distribution (see also fig. 4.10 and 4.11) but it is accompanied by a more significant drop of the effective area as discussed in the next section. With a ratio comprised between ∼1.5 and 4, the tails of the distribution are smaller at all energies in the case of the reconstruction using only calorimeter.
The PSF of the pre-shower improves with the energy because, as stated before, the identification of the hit in the pre-shower is made easier by the higher energy of the pair. Fig. 4.16 shows the trend of the pre-shower only PSF with changing phi, on the left, and theta, on the right. Only slight changes are visible in the case of different phi, as expected. The variations of the PSF with theta is more substantial, with a worsening up to theta $\sim 10°$ and then an improvement. This tendency is caused by the large gap between the tracker and the pre-shower. For such high angles, in most of the reconstructed events the gamma ray does not previously interact in the tracker but converts directly in the CsI inside the pre-shower, leading to a cleaner reconstruction but a considerable loss in effective area, as shown in the following.
The overall PSF, as well as the calorimeter only PSF, of both baseline and enhanced configuration are almost constant at the change of phi, as shown in fig. 4.17. A worsening of the PSF with an increase of theta is expected, mainly because of the higher crossed radiation length. This trend is visible in the calorimeter only PSF (bottom of fig. 4.18) and for the low energy (less than 30 GeV) part of the overall reconstruction. At high energy the understanding of the situation is complicated by the simultaneous use of information from the tracker and the calorimeter at low angle and the lack of these joint information at high angles,

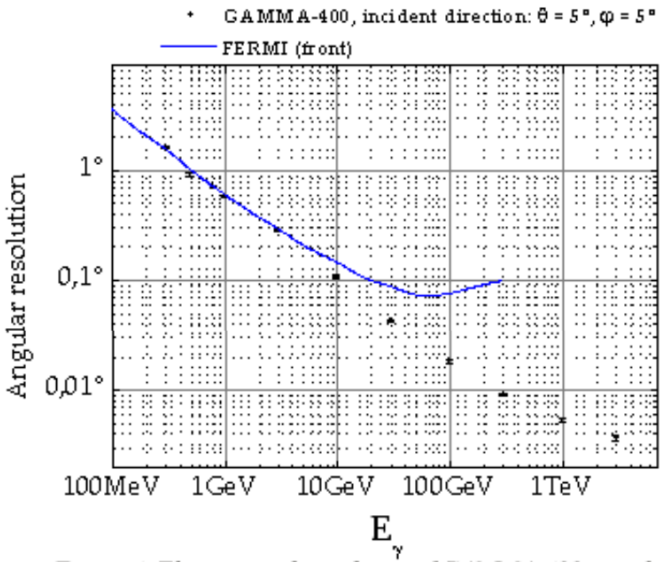

Figure 4.19: Energy dependence of the GAMMA-400 angular resolution as calculated in [105].

due to the long lever arm in the baseline and the limited width of the calorimeter in the enhanced configuration. Combining these effects, the overall PSF of both configurations at high energies has an improvement at high angles at the expense of the energy evaluation.
It has been demonstrated [105] that the angular resolution of the baseline can be increased, at high energy, reaching 0.01° at 300 GeV , as shown in fig. 4.19. The effective area related to this type of reconstruction has not been evaluated.

4.5.3 Effective area

The effective area A_{eff} gives an estimate of the ability of the instrument to detect the incoming photons. It is proportional not only to the geometrical area of the detector but also to the possibility of the gamma ray to convert inside the instrument and to the tracks of the created pair to be reconstructed.
The simulations were performed with a number of events high enough to consider a uniform distribution of the point on the starting surface. Defining ϵ as the detection efficiency, the effective area can be written as

$$A_{eff} = A_{det} \cdot \epsilon = A_{det} \cdot \frac{N_{riv}}{N_{cross}} = A_{det} \cdot \frac{A_{gen} \cdot N_{riv}}{N_{gen} \cdot A_{cross,det}} = \frac{A_{gen} \cdot N_{riv}}{N_{gen}}, \qquad (4.20)$$

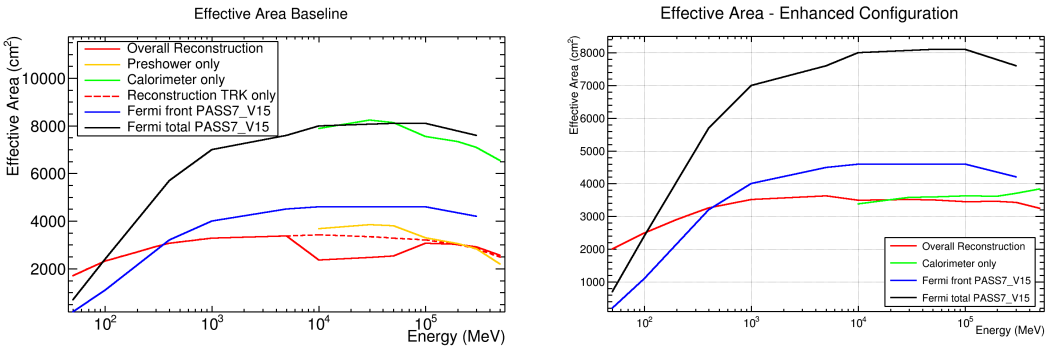

Figure 4.20: Comparison between the effective area of the baseline (*left*) and enhanced configuration (*right*) and the effective area of Fermi front and total. In red the effective area results of the overall reconstruction (using the combination of information from the tracker and the other instruments), in yellow the results of the pre-shower only reconstruction and in green the results of the calorimeter only reconstruction. These last two type of reconstruction are performed only in the case of a failed overall reconstruction. The dashed line is obtained without the use of information from the calorimeter and pre-shower.

where A_{det} is the geometrical area of the sensitive part of each detector (e.g. the Silicon in the Tracker or the CsI in the calorimeter), N_{riv} is the number of events for which a reconstruction of the original direction of the gamma ray is available, N_{cross} is the total number of events which cross the detector, N_{gen} is the total number of events, A_{gen} is the area of the surface from which the particle are generated, $A_{cross,det}$ is the illuminated area of the detector. In this case $A_{det}/A_{cross,det} = 1$ because the detector is homogeneously illuminated.
The results of the best possible reconstruction for each geometry is shown in fig. 4.20 labelled as overall reconstruction. The results of GAMMA-400 are compared with the performance of Fermi front and total. The difference between GAMMA-400 and Fermi is due not only to the different reconstruction algorithm but also to the difference in the geometrical area of the two instrument, of the order of $\sim$ 19500 cm^2 for Fermi and $\sim$ 9500 cm^2 for GAMMA-400. At very low energy ($<$ 100 MeV) the effective area of both configurations is higher than Fermi total, because of the preliminary version of the reconstruction algorithm not taking in consideration the rejection of charged particles, and Fermi front, thanks to the thicker tungsten of the baseline. The better angular resolution of the enhanced configuration with respect to the baseline is also followed by a better effective area in all energy ranges. The drop at 10 GeV, experienced by both configurations, but more pronounced for the baseline, is related to the quality cuts used in the joint reconstruction, as explained in chap. 4.3.

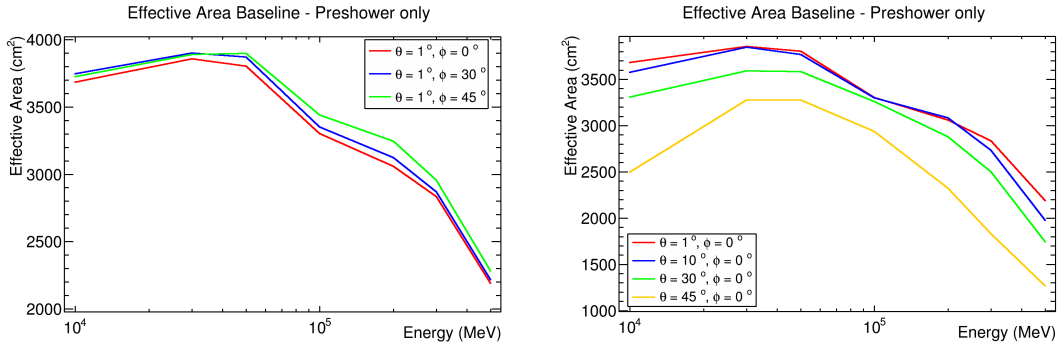

Figure 4.21: Comparison between the pre-shower effective area at various phi (*left*) and theta (*right*). The reconstruction is performed only in the case of a failed overall reconstruction.

In the case in which the overall reconstruction fails to provide a direction of the incoming particle, the calorimeter, or pre-shower, only reconstruction is performed and the resulting effective area is showed in fig. 4.20. The sum of the three different effective areas gives an estimation of the total effective area of the instrument, shown in fig. 4.24. The big difference between the effective area of the calorimeter in the two configuration is due to the bigger geometrical area and the less efficient overall reconstruction of the baseline that both result in a higher number of events reconstructed with the calorimeter.
While constant at the change of phi (see left of fig. 4.21), the effective area of the pre-shower only decreases at the increase of the angle (see right of fig. 4.21). As stated before, for such high angles the gamma ray does not cross both the tracker and the pre-shower but only one of the two, crossing less radiation length, even taking in consideration the different angles. As an example, the radiation length crossed by a gamma ray coming with a 45° angle is ~ 1.4 X_0, while for a 1° is ~ 2 X_0. The ratio between the crossed radiation length and the effective area in the two cases is indeed similar (~ 0.7).
The overall effective area, as well as the calorimeter only effective area, of both baseline and enhanced configuration are almost constant at the change of phi, as shown in fig. 4.22, but change considerably with a change of theta (see fig. 4.23). The rise of the calorimeter only effective area with the increase of the angle is due to the calculation of the effective area itself. At low angles a lot of events are reconstructed also in the tracker and, consequently, do not contribute to the calorimeter only effective area. The different trend between the calorimeter only and pre-shower only effective area is due to the different reconstruction algorithm and geometry of the detectors. While for the pre-shower the gamma ray has to convert in the first CsI plane in order to hit both the Si planes, in the calorimeter

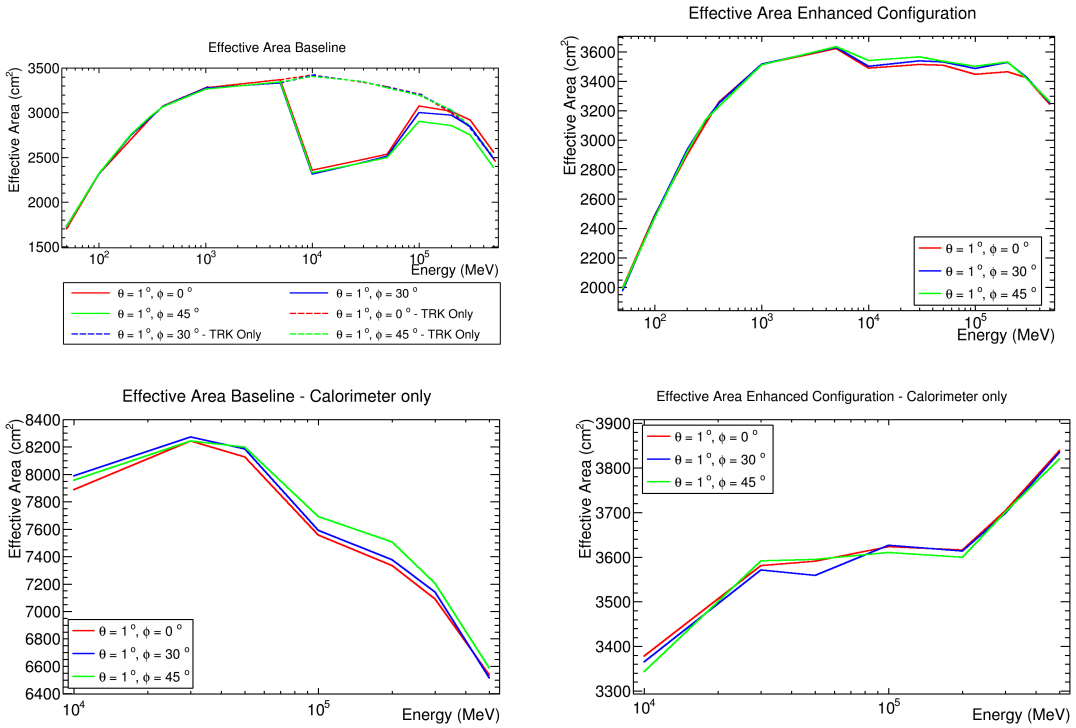

Figure 4.22: Comparison between the effective area of the baseline (*left*) and enhanced configuration (*right*) for the overall reconstruction (*top*) and the calorimeter only reconstruction (*bottom*) for different phi and theta equal 1°. The dashed lines are obtained without the use of information from the calorimeter and preshower. The calorimeter only reconstruction is performed only in the case of a failed overall reconstruction.

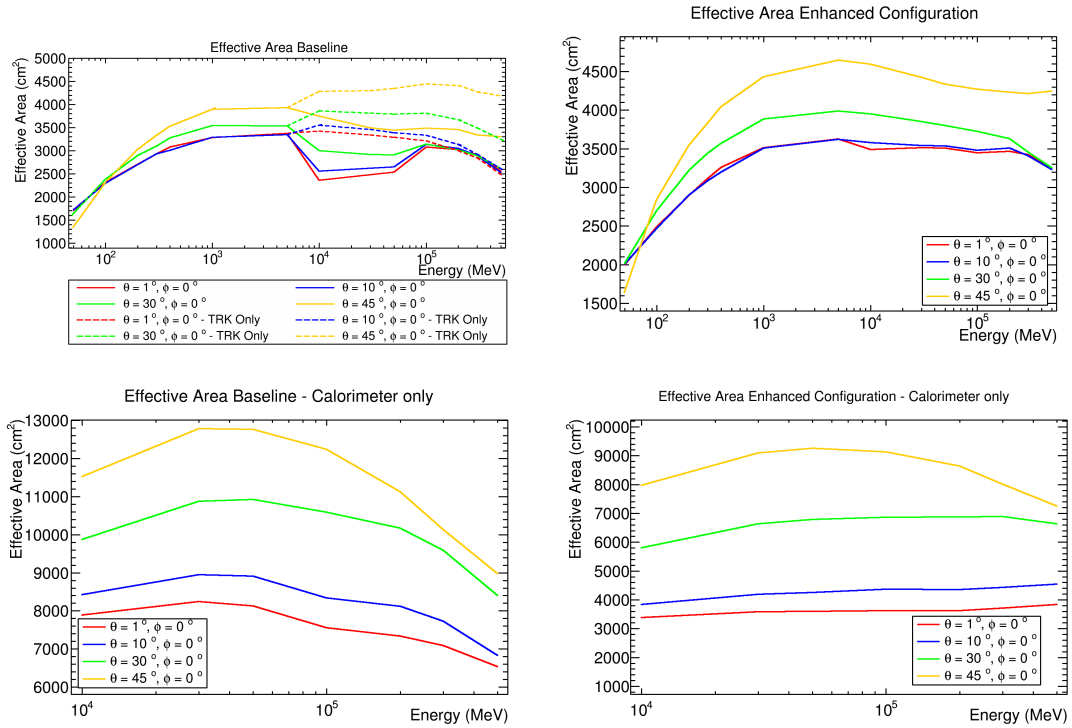

Figure 4.23: Comparison between the effective area of the baseline (*left*) and enhanced configuration (*right*) for the overall reconstruction (*top*) and the calorimeter only reconstruction (*bottom*) for different theta and phi equal 0°. The dashed lines are obtained without the use of information from the calorimeter and preshower. These calorimeter only reconstruction is performed only in the case of a failed overall reconstruction.

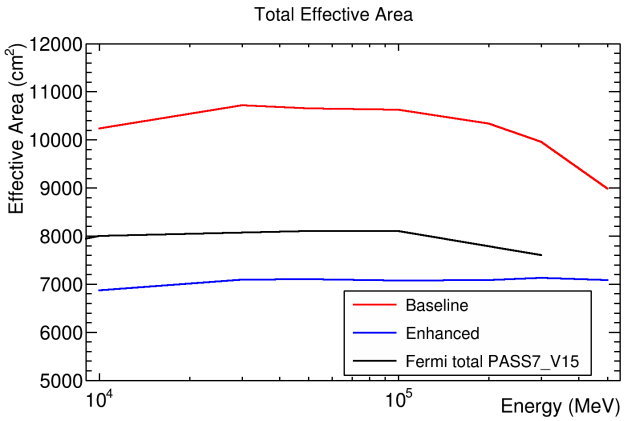

Figure 4.24: Comparison between the total effective area of the baseline, enhanced configuration and of Fermi total. Below 10 GeV the total effective area is equal to the effective area of the overall reconstruction of fig. 4.20.

the conversion can happen in any of the planes, except the last two, effectively eliminating the problem of not enough radiation lengths crossed. Less events interacting both in the tracker and in the calorimeter means also less backsplashed particles for the overall reconstruction and, consequently, a cleaner and more effective reconstruction that increases the effective area as well. It should be noted that, without the interaction in the calorimeter, the energy resolution at high energy (> 10 GeV) for large angles, is severely worsen, counting only on the estimation by the tracker.

4.5.4 Sensitivity

The results on the PSF and the effective area, as well as the pointing strategy of the instrument, all contribute to the sensitivity of the satellite. A study on the point source sensitivity of GAMMA-400 has been made for two regimes: flux and background dominated.
Since the arrival of photons from the background follows a Poisson distribution, the variance of the distribution can be expressed as $\sqrt{N_b}$, with N_b the number of photons from the background. The 5-sigma sensitivity can be then estimated as the flux of the point source for which

$$N_s = 5\sqrt{N_b}, \tag{4.21}$$

with N_s the number of photons from the source. The number of photons from the background N_b can be expressed as a function of the angular resolution and the

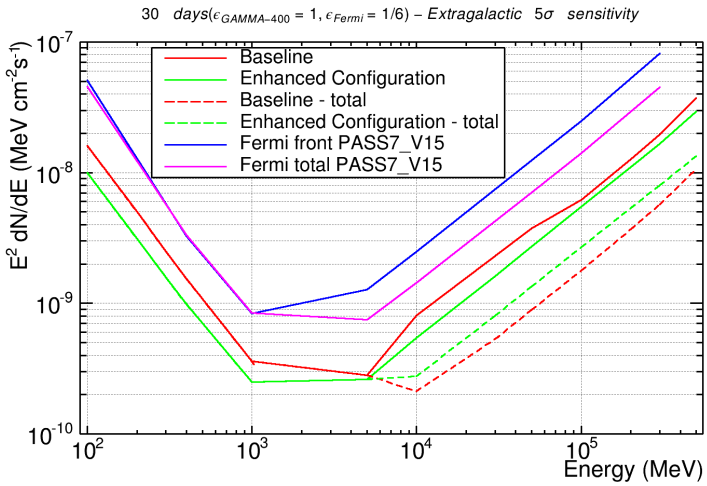

Figure 4.25: Point source (5σ) sensitivity of both configuration of GAMMA-400, Fermi front and Fermi total, derived using the same method. An extragalactic background is assumed for an observation time of 1 month. The dashed lines are computed using the total PSF and effective area, result of the reconstruction using, in order: the tracker, only the pre-shower, in the case of the baseline, and only the calorimeter.

exposure exp

$$N_b = F_b \cdot E \cdot exp \cdot \Omega, \tag{4.22}$$

where E is the energy, F_b is the background flux and Ω is the solid angle of the PSF in sr. The value of the background flux is derived from [54]. The total flux of the isotropic gamma-ray background above 100 MeV is equal to $F_{100} = 1.03 \pm 0.17 \cdot 10^{-5}$ cm^{-2}s^{-1}sr^{-1} and the spectrum can be fit by a power-law with index $g = -2.41 \pm 0.05$ (see also chap. 1.2.6). The total flux can then be written as

$$F_{100} = \int_{100}^{\infty} F_b dE = \int_{100}^{\infty} F_0 \left(\frac{E}{E_0}\right)^g dE = \frac{F_0}{E_0^g} \int_{100}^{\infty} E^g dE, \tag{4.23}$$

where $F_b = F_0(E/E_0)^g$, with F_0 and E_0 constant. Solving the equation 4.23 for F_0 it follows that $F_b \simeq (E[\text{MeV}])^g \cdot 959.5 \cdot 10^{-5}$ MeV^{-1}cm^{-2}s^{-1}sr^{-1}.
The pointing strategy has an effect on the exposure through an efficiency ϵ, which is the fraction of an orbit during which the instrument can observe the source. For satellites in pointing mode in a high altitude orbit, like GAMMA-400, $\epsilon = 1$ while $\epsilon = 1/6$ for satellites on lower orbit and survey mode, such as Fermi, due to the Earth occultation and different pointing strategy. The exposure can be written as $exp = A_{eff} \cdot T_{obs} \cdot \epsilon$ where A_{eff} is the effective area and T_{obs} is the total time of

observation.
Since the number of photons from the source at a given energy E can be written as $N_s = F_s \cdot E \cdot exp$, the 5-sigma sensitivity can be found inserting eq. 4.22 in eq. 4.21

$$F_s = 5 \cdot \frac{\sqrt{F_b \cdot E \cdot exp \cdot \Omega}}{E \cdot exp} = 5 \cdot \sqrt{\frac{F_b \cdot \Omega}{exp \cdot E}}. \tag{4.24}$$

At high energy it is possible that, while the condition in eq. 4.21 is satisfied, the number of photons from the source is insufficient to claim a detection. A minimum of five photons is set as a requirement to claim a detection. In this regime, referred to as flux dominated, the 5-sigma sensitivity to a point source with spectral index equal to -2 is defined as the flux for which

$$N_s = 5 = exp \int_E^\infty F_s \left(\frac{E}{E_0}\right)^{-2} dE = exp \cdot F_s \frac{E_0^2}{E}. \tag{4.25}$$

The 5-sigma sensitivity is then simply $F_s = 5 \cdot E/(E_0^2 \cdot exp)$.
The greater value of F_s between the results in the background and flux dominated regimes for each energy is plotted in fig. 4.25, multiplied by E^2 in the case of the flux dominated to match the units (MeV·cm^{-2}·s^{-1}). The results for both configurations are compared to the results obtained for Fermi front and total. The passage from the background dominated regime to the flux dominated regime happens at 5 GeV for each instrument and configuration.
Both configurations are better than Fermi thanks to the observation technique and, in the background dominated regime, the improvement in angular resolution of the enhanced configuration. The enhanced configuration has a better sensitivity because of the better angular resolution, in the background dominated regime, and the higher effective area in the flux dominated regime. The results labelled as total in fig. 4.25 are obtained estimating the PSF and effective area using, in order, the events reconstructed by the overall reconstruction plus the events reconstructed using only the pre-shower and only the calorimeter (see fig. 4.20). In this case the baseline has a better total sensitivity from 5 GeV up thanks to the joint contributions from the wider calorimeter and the pre-shower.

Chapter 5

Trigger System for Gamma-ray Observations

Due to a limited downlink capability ($\sim$ 100 GB/day) and a very high background from charged particles, mainly protons, an efficient trigger system is needed in order to effectively study gamma-ray sources. With a rate of $\sim 10^6$ incoming charged particle for each gamma ray, the cosmic-ray contamination may indeed, without an effective trigger system, blind the instrument for gamma-ray observations. This chapter will present a preliminary work for the GAMMA-400 trigger system for gamma-ray observations using information from the tracker. The study tries to exploit the characteristic of each detector to reject as many protons as possible while keeping the highest number of gamma rays, in order to not lower the effective area, especially at high energy where the number of photons is limited. This work is based on the trigger system of similar experiments: AGILE [106; 107] and Fermi [108].
The analysis is divided into two parts: conditions that can be applied on-board (chap. 5.2), before the downlink, and methods to be applied after the transmission of the data to ground (chap. 5.3). Discriminating between these two parts is the reconstruction of the direction of the incoming particle. The trigger on board must be fast in order to avoid the loss of events during the time necessary to discriminate between photons and charged particles. Being the reconstruction a slow process, each condition applied after that, including the reconstruction itself, must be applied on ground. The results obtained by means of the conditions described below will be presented in sec. 5.4. Possible further improvements will be discussed in sec. 5.5.

5.1 Simulations set-up

The simulation set-up is studied in order to describe as closely as possible the possible on-orbit events. In order to be able to simulate the correct source distribution and spectrum the G4GeneralParticleSource (GPS) class of the Geant4 [99] toolkit is chosen as the particle generator.
The proton background is simulated by means of a hemispherical distribution of sources, as shown in fig. 5.1. The center of the hemisphere is located at the bottom of the satellite and it encloses all the satellite. The particles generation points are equally distributed on the surface of the hemisphere and, thanks to a bias on the angle, they are all directed to the inside the hemisphere with a random angle. The on-orbit spectrum is simulated thanks to the Space Environment Information System (SPENVIS), an ESA (European Space Agency) interface to model the space environment and its effects. After inputting the orbit parameters, SPENVIS is able to provide the expected particle spectrum along the orbit and a datacard for simulations as well. The expected proton spectrum along the GAMMA-400 orbit, as simulated by SPENVIS using the model CREME96, is shown in fig. 5.2.
The same gamma-ray simulations used in the reconstruction analysis, and described in chap. 4.5.1, are also used in the trigger analysis. These simulations offers a good enough coverage in energy and angles to bypass the necessity of additional simulations.

5.2 Trigger on-board

		R				
		1.05	1.1	1.2	1.25	1.5
Baseline	γ	92.3%	89.3%	82.6%	79.2%	60.8 %
	p	32.7%	21%	12.7%	11%	7.2%
Enhanced	γ	91.6%	88.4%	82.6%	79.6%	62.7%
	p	31.6%	21%	12.9%	11%	6.4%

Table 5.1: Events that passes two trigger conditions: at least three planes hit in a row for each view and a ratio R between the total number of clusters and the number of hit views greater than the value in table.

The on-board trigger has the main purpose to lower the event rate in order to comply with the datalink limit. It differs from the trigger on the ground mainly for two reasons: timing and complexity. The trigger on-board has to be fast, in

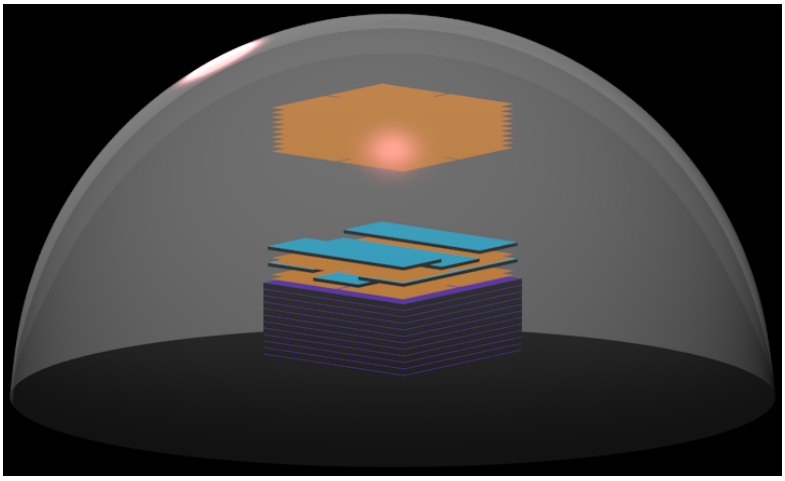

Figure 5.1: Source distribution used for the simulation of the background of GAMMA-400. The starting points of all the protons are uniformly distributed on the glass-like hemisphere centered at the bottom of the instrument and encompassing it all. All the particles are directed inside the hemisphere with random theta and phi.

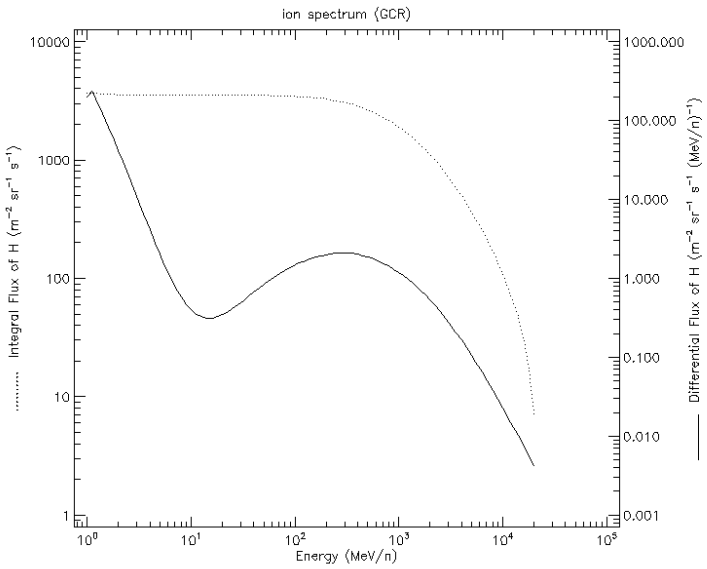

Figure 5.2: On orbit proton spectrum simulated using a model CREME96 with SPENVIS and used for the simulation of the background of GAMMA-400.

order not to miss events during the dead time and avoid pile-up, but it has to be based on a simple, mainly hardware based, architecture.
Since this is a study for a trigger system for gamma-ray observations, events that can not be reconstructed can be discarded beforehand. The only a priori condition for the reconstruction is that at least three planes are subsequently hit in each view in the tracker. This condition is also the main condition of the trigger and it will be referred to as TRK in the following.
A lower number of hits in the tracker planes is expected for protons compared to gamma rays, which are actually two particles, the e^-/e^+ pair. Defining the ratio R as the ratio between the total number of clusters and the number of hit views, a lower limit on R can be used to discriminate between protons and gamma rays. Different values of R were tested, as reported in tab. 5.1 and fig. 5.3. The chosen value of 1.1 is the lowest number that allows the passage of $\sim 90\%$ of the gamma rays while rejecting more than 70% protons. To ensure that the proton rejection is not limited to a particular energy bin, the percentage of events per energy bin that passes the condition is computed. As shown in tab. 5.2 the percentage is stable for protons in both configurations while there is a difference of $\sim 10\%$ between the minimum and the maximum for gamma rays. The rise of the percentage of gamma rays with energy greater than 30 GeV that passes the condition is more prominent in the case of the baseline. This different behaviour can be explained by the width of the calorimeter, wider in the baseline, and consequently the number of gamma rays that interact in the calorimeter itself. Having more highly energetic particles interacting in the calorimeter results in a higher amount of backsplashed particles that contributes to increase R.
If an event passes both the TRK and R conditions a check on the timing of the interactions with the detector is made. Under study is the possibility to obtain timing information not only from the time-of-flight (with a 0.5 ns resolution) but also from the anticoincidence (with 1 ns resolution). By looking to the first interaction it is possible to reconstruct the morphology of the event. Different situations can arise:

- The time given by the time-of-flight (TOF) is lower than the time of the top (ACT) and side (ACS) anticoincidence. This is the case of protons interacting in the calorimeter and creating backsplashed particles that interact firstly in the TOF and then in the TRK, or of gamma rays, converting in the tracker and then interacting in the TOF. To discriminate these two types of events, upgoing from downgoing particles, a check on the timing of the different TOF planes is made. Events with an interaction in the highest TOF plane at a later time than other planes are marked as upgoing and rejected. Since this study is related to gamma-ray observations using the tracker, also

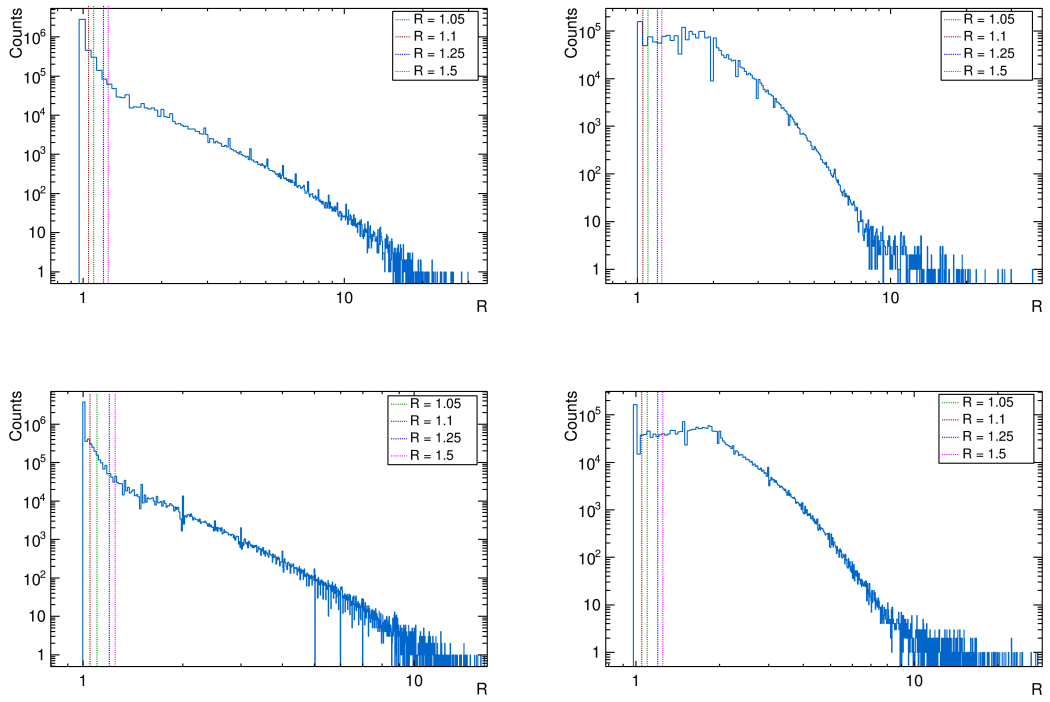

Figure 5.3: Ratio between the total number of clusters and the number of hit views for the baseline (*upper row*) and the enhanced configuration (*lower row*) in the case of incoming protons (*left column*) or gamma rays (*right column*).

		R = 1.1				
		E⩽ 50 MeV	50 MeV<E⩽ 100 MeV	100 MeV<E⩽ 200 MeV	200 MeV<E⩽ 300 MeV	300 MeV<E⩽ 400 MeV
Baseline	γ	83%	92%	96%	97%	97%
	p	21%	21%	21%	21%	21%
Enhanced	γ	84%	92%	96%	96%	97%
	p	21%	21%	20%	21%	20%

		R = 1.1				
		400 MeV<E⩽ 1 GeV	1 GeV<E⩽ 5 GeV	5 GeV<E⩽ 10 GeV	10 GeV<E⩽ 30 GeV	30 GeV<E⩽ 50 GeV
Baseline	γ	97%	86%	82%	80%	83%
	p	21%	21%	21%	21%	21%
Enhanced	γ	97%	90%	87%	83%	84%
	p	20%	20%	20%	20%	20%

		R = 1.1			
		50 GeV<E⩽ 100 GeV	100 GeV<E⩽ 200 GeV	200 GeV<E⩽ 300 GeV	300 GeV<E⩽ 500 GeV
Baseline	γ	89%	94%	89%	92%
	p	21%	21%	21%	21%
Enhanced	γ	84%	85%	85%	86%
	p	20%	20%	20%	20%

Table 5.2: Percentage of events per energy bin that passes the condition on the ratio between the total number of clusters and the number of hit views for the baseline and the enhanced configuration in the case of incoming protons or gamma rays. The 100% is the total number of events with at least three planes hit in a row in both views.

the events with no interaction in the first TOF but with an energy deposit in the subsequent TOF planes are rejected. These events are indeed associated to charged particles or to gamma rays not converting into the tracker but into the pre-shower or in the calorimeter.

- The ACT is the first hit detector. This kind of event can be associated both with a proton coming from above or a gamma ray converting in the tracker and creating an upgoing particle. Three different approaches were considered: rejecting all the events with a signal in the ACT, rejecting all the events with the ACT as the first detector hit (based on the timing of interaction with the TOF and ACS) or let all the events pass. These different approaches are necessary because it is possible for a gamma ray to indirectly leave a signal in the ACT, mainly through backsplash from the calorimeter.

- The ACS is the first hit detector. Having the ACS two layers spaced 15 cm, a check on the two subsequent layers is performed. If the time of the hit on the internal layer is higher than the time of the hit on the external layer, the event is associated to charged particles coming from outside and rejected. If instead the time of the hit on the internal layer is lower than the time of the hit on the external layer, the event is associated to a gamma ray converting inside the detector and escaping from the side. The last case is the one in which the particle hits only one of the two layers, either because it stops in one of them or it passes through a gap between the tiles, or it has the same time of interaction, within the timing resolution, in the two layers. In this case the event passes the trigger as the morphology is unclear.

- It is also possible that no AC or TOF are hit. This is the case e.g. of a low energy gamma ray that creates a pair in the tracker which stops before hitting any other detectors. These events are generally associated with gamma rays and consequently pass the trigger.

In the case that the ACS is the first hit detector and the check on the two layers on the same side is already passed, a check on the distance between the cluster in the tracker and the tile hit is performed. A downgoing charged particle coming from the side is expected to hit the tracker planes at an increasing distance from the hit tile. An electron or positron escaping from the side of the detector is instead expected to leave hit on the tracker planes higher than the hit tile and at a decreasing distance. If the first hit tile of the ACS is positioned below the first TOF, located just below the tracker, the event is rejected. This condition is useful to reject upgoing (theta greater than 90°) charged particles entering from the side and interacting only in the first TOF and the tracker. This kind of event can be

		Ren			
		0.4	0.5	0.6	0.7
Baseline	γ	93.3%	97.1%	98.9%	99.6%
	p	78%	81.3%	84.7%	87.3%
Enhanced	γ	96.7%	98.6%	99.5%	99.8%
	p	74.6%	78.3%	82%	84.9%

Table 5.3: Events that passes two trigger conditions: at least three planes hit in a row for each view and a ratio Ren between the number of clusters with an energy deposit greater than 3 MIP and the total number of clusters lower than the value in table.

more frequent in the baseline because of the great gap between the tracker and the pre-shower.
Interacting nuclei are expected to release a higher amount of energy inside the Si planes of the tracker with respect to gamma rays. Defining the ratio Ren as the ratio between the number of cluster with an energy deposit greater than 3 MIP (Minimum Ionizing Particle, $\sim$116 keV for the tracker Silicon planes) and the total number of clusters, an upper limit on Ren can be used to discriminate between protons and gamma rays. Different values of Ren were tested, as shown in tab. 5.3 and fig. 5.4, and the value 0.6, which allows to keep $\sim$99% gamma rays and reject $\sim$17%, is chosen. This condition is thought more to reject nuclei, due to the dependence of the energy release by the square of the charge, hence the low rejection for protons. Considering different energy bins or instrument configuration, no significant difference between the percentage of events that passes the condition can be found, as shown in tab. 5.4.
To sum-up, events that pass the on-board trigger are the ones with at least three planes hit in a row in the tracker with a ratio R greater than 1.1, with the correct timing characteristic, satisfying the conditions on the AC and with a ratio Ren smaller than 0.6.

5.3 Trigger on the ground

The events that pass the on-board trigger are to be sent on the ground. Here a more refined trigger can further reject charged particles in favour of gamma rays. Differently from the on-board trigger, the trigger on the ground can be slower and this allows a more polished process.

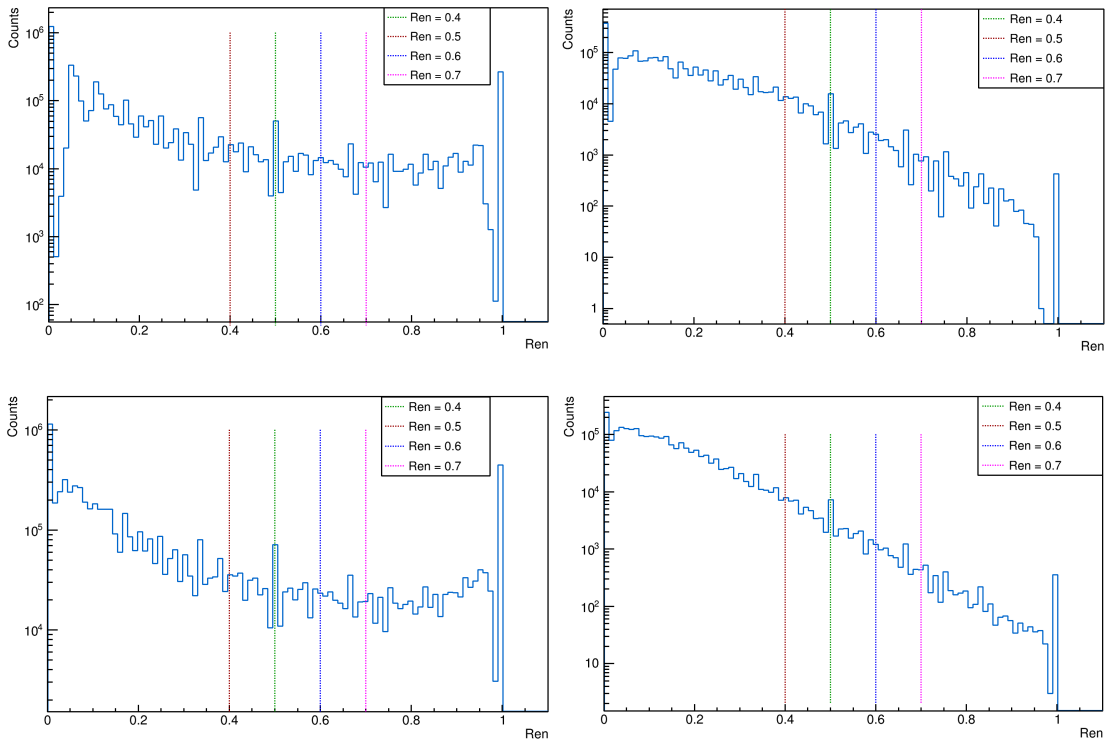

Figure 5.4: Ratio between the number of cluster with an energy deposit greater than 3 MIP and the total number of cluster for the baseline (*upper row*) and the enhanced configuration (*lower row*) in the case of incoming protons (*left column*) or gamma rays (*right column*).

		Ren = 0.6				
		E⩽ 50 MeV	50 MeV<E⩽ 100 MeV	100 MeV<E⩽ 200 MeV	200 MeV<E⩽ 300 MeV	300 MeV<E⩽ 400 MeV
Baseline	γ	99%	99%	99%	99%	99%
	p	84%	84%	84%	84%	84%
Enhanced	γ	100%	100%	99%	99%	99%
	p	81%	81%	81%	81%	81%

		Ren = 0.6				
		400 MeV<E⩽ 1 GeV	1 GeV<E⩽ 5 GeV	5 GeV<E⩽ 10 GeV	10 GeV<E⩽ 30 GeV	30 GeV<E⩽ 50 GeV
Baseline	γ	99%	99%	99%	98%	99%
	p	84%	84%	84%	84%	84%
Enhanced	γ	99%	99%	99%	99%	99%
	p	81%	81%	81%	81%	81%

		Ren = 0.6			
		50 GeV<E⩽ 100 GeV	100 GeV<E⩽ 200 GeV	200 GeV<E⩽ 300 GeV	300 GeV<E⩽ 500 GeV
Baseline	γ	99%	99%	97%	97%
	p	84%	84%	84%	84%
Enhanced	γ	99%	99%	99%	98%
	p	81%	81%	80%	81%

Table 5.4: Percentage of events per energy bin that passes the condition on the ratio between the number of hits with an energy deposit greater than 3 MIP and the total number of clusters, for the baseline and the enhanced configuration in the case of incoming protons or gamma rays. The 100% is the total number of events with at least three planes hit in a row in both views.

At this point the reconstruction of the direction of the particle is performed as described in the previous chapter. This passage leads to a significant loss of events in both cases, charged particles or gamma rays, due to the intrinsic efficiency of the reconstruction itself and not to trigger-related causes.
If an event is reconstructed and the top anticoincidence is not the first hit detector, the particle is then identified as a gamma ray. Instead, if the ACT has the lowest timing between all detectors, a check on the position of the reconstructed track on the ACT is performed. If the first hit tile on the ACT lays along the track than the event is related to a proton coming from above the apparatus and thus rejected. If instead the reconstructed track does not cross the first hit tile in the ACT, then the particle is labelled as a gamma ray. This last condition is bypassed using the approach in which all the events with signal in the ACT, being it first or otherwise, are already rejected on-board.

5.4 Results

The results of the subsequent application of the trigger conditions are shown in fig. 5.5. All the percentage refers to the total number of events that pass the first trigger condition on the number of planes hit in the tracker. As stated before, a study on different rejection conditions for the anticoincidence is performed.
For gamma rays, the ratio of the remaining events after the trigger is similar for each different condition in both geometries. For the baseline the difference between the percentage of events to be sent to ground considering the most loose and strict conditions is 5.5%. These conditions, summarized in the flow charts in fig. 5.6 and fig. 5.7 respectively, correspond to the rejection of all the events with a signal on the AC and the passing of all the events with the ACT as first detector hit. The same difference for the enhanced configuration is 10.3%. Considering instead the events that passes the on the ground conditions, this difference is further lowered: only 0.028% for the baseline and 0.023% for the enhanced configuration.
Differently from the gamma rays, the protons show a larger spread between the results of the different cases. After the on-board trigger the difference is of 12% for the baseline and 13.5% for the enhanced configuration. The same difference is lowered to 0.7% for the baseline and 1.8% for the enhanced configuration after applying the conditions on the ground.
Since the main issue for the space mission is to reduce the information to be sent to ground and the difference between the application of the overall trigger condition is negligible in the gamma-ray case and considerable in the case of protons, it is possible to use a strict condition on the anticoincidences. The best choice is then the rejection of all the events with a signal in the ACT or in which the first

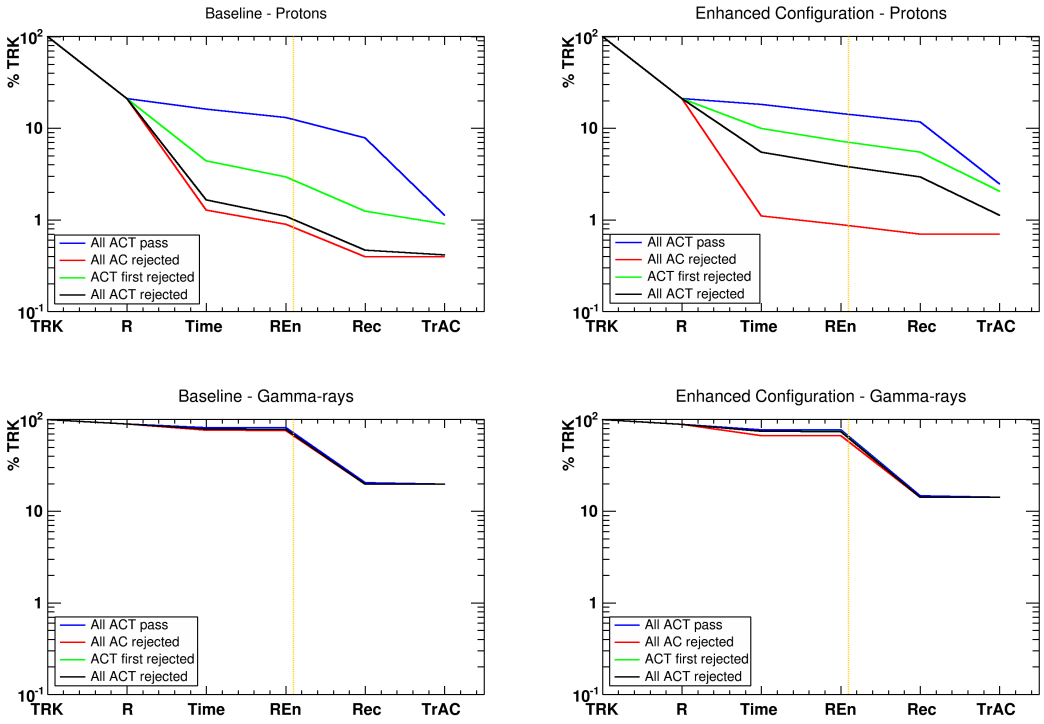

Figure 5.5: Events that passes the trigger conditions for the baseline (*left*) and enhanced configuration (*right*) in the case of incoming protons (*top*) or gamma rays (*bottom*). The different conditions on the anticoincidence are presented. The vertical orange line discriminates the on-board conditions (on its left) from the conditions to be applied on the ground (on its right). The results are presented as the percentage over the total number of events that passes the first condition (TRK).

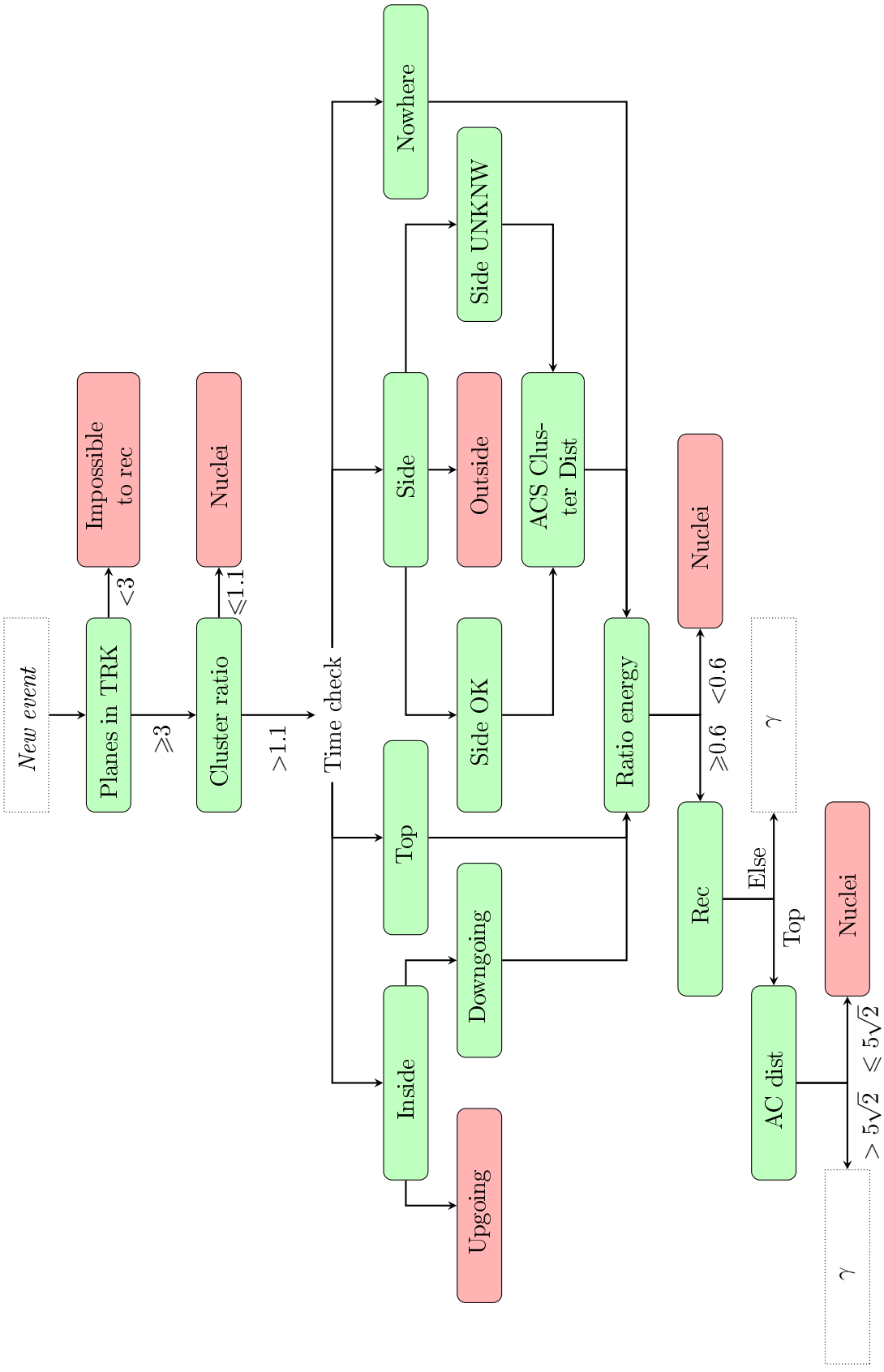

Figure 5.6: Intermediate trigger flow chart with the more loose timing conditions.

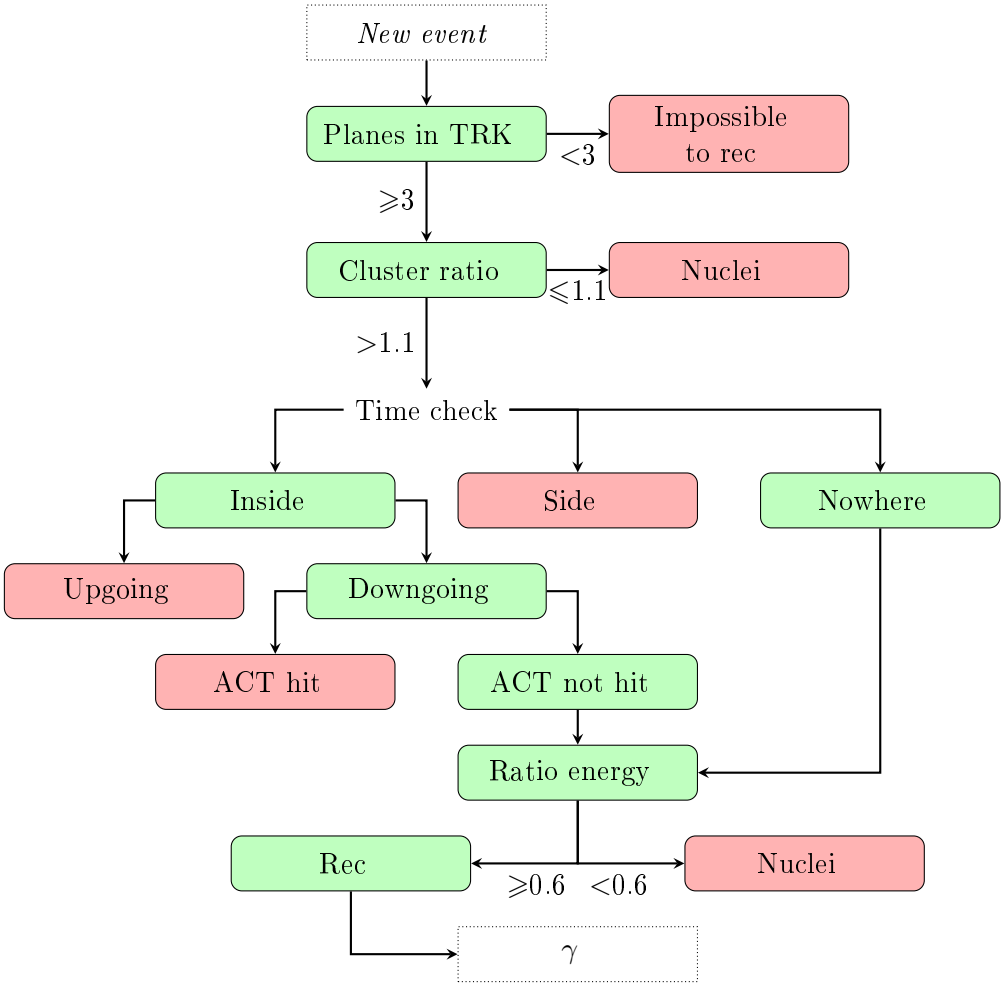

Figure 5.7: Final trigger flow chart with the more strict timing conditions.

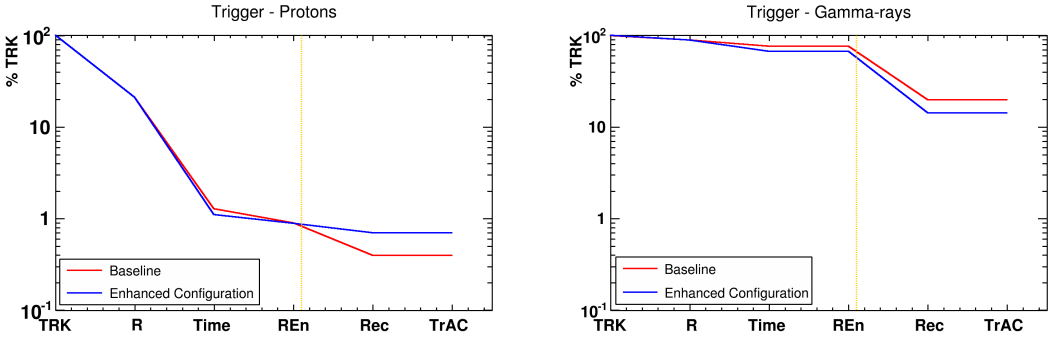

Figure 5.8: Final results of the trigger algorithm for protons (*left*) and gamma rays (*right*) for both configuration. The vertical orange line discriminates the on-board conditions (on its left) from the conditions to be applied on the ground (on its right). The results are presented as the percentage over the total number of events that passes the first condition (TRK).

interaction is in the ACS. The results and comparison between the two geometries are shown in fig. 5.8. There are some minor differences between the two configurations, of the order of 1% for protons and 5% for gamma rays, that are related to the reconstruction of the events with the two different geometries. The intrinsic efficiency of the reconstruction is also responsible of the drop in the percentage of events that passes the trigger, especially for the gamma rays. By looking at the number of events reconstructed without any trigger condition (except for the TRK which is necessary for the reconstruction itself) it is possible to disentangle the contribution of the reconstruction efficiency, seeing more effectively how the trigger algorithm operates. In the case of the gamma rays the trigger results in a loss of reconstructed events of 2.8% for the baseline and 1% for the enhanced configuration. For the protons the rejection is considerably higher: 57.8% for the baseline and 91.9% for the enhanced configuration. Therefore the trigger system works properly by not affecting much the gamma-ray observation but allowing a great reduction of the proton rate.
The total number of remaining proton events both after the on-board (0.892% for the baseline and 0.885% for the enhanced configuration) and the on the ground (0.397% for the baseline and 0.701% for the enhanced configuration) trigger is still too elevated. Possible further improvements, also related to the observation using different detectors or of different particles, are discussed in the next section.

5.5 Further Improvements

As said at the beginning of the chapter, the study reported here is dedicated to the observation of gamma rays with the tracker. GAMMA-400 will be able to reconstruct the direction of the incoming gamma rays using information coming only from the calorimeter, a possibility not yet included in the study. Being a dual instrument, GAMMA-400 will also collect information on electrons, protons and nuclei, thus a complete charged particle rejection is not foreseen and a development of different triggers is needed. In this section some possible ideas on how to implement a complete trigger algorithm will be described for each particle type.

- **Gamma rays:** While promising, the study of a trigger system for the observation of gamma rays with the tracker must be continued in order to achieve a better rejection of charged particles. In particular the on-board trigger has to further reduce the rate of information to be sent to ground. A simple reconstruction algorithm to be performed on-board can be implemented, similarly to what has been done for AGILE. A different trigger for the observation using only the calorimeter or the preshower shall be developed. This trigger system can be linked to the energy released in the CsI. In the results

on the performance presented in chap. 4.5, the direction is reconstructed for an energy deposit of at least 8 GeV. At lower energy both the angular resolution and the effective area degrade. For the study of transients a trigger based on the rate of events inside the calorimeter can also be defined in order to allow a more complete study of the source. The calorimeter, as well as the neutron detector in the baseline, can also be used to further reject hadrons by looking at the shape of the created shower.

- **Protons:** Since GAMMA-400 will be able to study protons and nuclei up to the knee, it is necessary to withhold the information of highly energetic charged particle. Since some of the on-board trigger conditions could reject such events, a bypass of all the conditions in the case of a sufficiently high energy release in the calorimeter is foreseen. Since the bulk of the proton distribution is at low energy, most of the particle would be rejected in any case.

- **Electrons:** Similarly to what said before, a condition on the energy released in the calorimeter will allow to study the all electron spectrum up to the TeV energy region. The shape of the shower will allow to reject the hadron contribution in the same energy range.

- **Nuclei:** Since the design of the charge identification system around the calorimeter is not yet definitely confirmed, a threshold on the energy release in the calorimeter, already added for the protons, can help to not reject highly energetic nuclei. An algorithm to identify the charge, based on the energy released inside the charge identification system will be thought of in the future. For nuclei coming from above the instrument and interacting inside the tracker, the subsequent planes can be used for different measurements of dE/dx, which is proportional to the module of the charge. A condition similar to the one described above on the ratio between the clusters with an energy release greater than a threshold and the total number of cluster could be applied. In this case, instead of rejecting the particles with ratio lower than a threshold, particles with a ratio higher than the threshold, to be carefully calculated, could pass the trigger for the nuclei.

Chapter 6

Gamma-ray Bursts Detection with GAMMA-400

As mentioned in chap. 1.3 a thorough study of the time response capabilities of GAMMA-400 is still missing. In this chapter a preliminary study of the ability of GAMMA-400 to observe gamma-ray bursts (GRBs, see chap. 1.3.3 for an observational review) is presented. This study is focused on the energy range not accessible to the Konus-FG system (energies greater than 10 MeV) in order to understand if the other parts of the detector can complement the low energy information without losing information because of the pile-up. The simulation set-up will be outlined in chap. 6.1 while the results of the method, described in sec. 6.2, will be presented in sec. 6.3.

6.1 Simulation set-up

The photons from a GRB arrive on the satellite as a plane wave from a point source. To simulate a GRB, photons arriving with a given angle ($\theta = 30°, \phi = 0°$) are generated from a rectangle in order to illuminate all the apparatus, similarly to what described in sec. 4.5.1. Given the large variety of GRB spectra it is not possible to define a spectrum describing them all. The spectrum of the simulated GRB is then chosen to be proportional to $E^{-2.1}$, with an energy between 10 MeV and 500 GeV. A total of $3 \cdot 10^6$ events are simulated.
The information on the photons arrival time are added after the simulation. An arrival time is associated to each simulated event in order to reproduce the light curve of a GRB. Two approaches are used: time intervals taken from the Fermi data of real GRBs and a fraction of the same intervals to simulate higher fluxes. The latter step is necessary in order to have a better understanding of the apparatus

Detector	Deadtime (μs)	Trigger condition
Tracker	80	3 consecutive planes hit in each view
Preshower	300	both Si planes hit in each view
Calorimeter	300	energy deposit at least 8 GeV

Table 6.1: Deadtime and trigger conditions for each of the main detectors. The deadtime values are the results of conservative assumptions.

behaviour in the case of very high fluxes, since in the Fermi data the reconstruction efficiency and deadtime (a minimum of 26.5 μs) are already included.
The information for the photon time arrival are taken from the short GRB 090510 [109] and the long 130427A [79]. Both the LLE (LAT Low Energy [110]) and TRANSIENT classes of events are used. TRANSIENT events are events with energy higher than 100 MeV, reconstructed using a looser background rejection compared to other classes. LLE events are reconstructed with even looser quality cuts, and thus greater error on the direction, comprising also lower energy ($<$ 100 MeV) events. Since the purpose of the analysis is to simulate a GRB, especially its timing characteristics, the use of both these classes of events ensures a more realistic description of the source, reducing also the effect of the Fermi instrumentation on the observation.

6.2 Method

The events were reconstructed only if the time between a trigger and the previous triggered events is higher than the deadtime. The deadtime of each different detector, result of conservative assumptions, as well as the condition for the trigger can be found in table 6.1. Different situations can arise depending on the time t_{trg} between two different triggered events:

- $t_{trg} > 300\mu$s: The two events are reconstructed separately.
- $80\mu\text{s} < t_{trg} < 300\mu$s: If in the last event the calorimeter, or the preshower in the case of the baseline, triggered, the event is not reconstructed. Instead if only the tracker triggered the observation of the previous event, the photon direction and energy of the two events are reconstructed.
- $t_{trg} < 80\mu$s: Only the first event is reconstructed.

The trigger window remains open as long as there are triggered events. This means that, as an example, if an event triggers only in the tracker and the subsequent

event triggers only in the tracker at a time t= 79μs, with no other subsequent event triggering the system, the trigger window stays open for a total of 159μs. This behaviour will depend on the readout system but for this analysis this worst case scenario, that will lead to a greater number of piled-up events, is used.
As previously stated, the Fermi data represents the timing of only the reconstructed photons. To make the results as less simulation dependent as possible, a time is given only to the events that cross the tracker, pre-shower or calorimeter. The simulated events are therefore divided in a different number of simulated GRBs, depending on the number of triggered events and the number of photon timing derived from the Fermi data.

6.3 Results

The light curve of the GRB 090510 as seen by the instruments aboard Fermi is presented in fig. 6.1. As previously stated, the timing of the photons used in this analysis are only the ones of the events seen by the LAT (two bottom panels). To reduce the effect of the reconstruction efficiency on the study, the results of the simulation of several light curves will be presented. Similarly, the light curve of the GRB 130427A as seen by Fermi is presented in fig. 6.1.
The reconstructed light curves of the GRB 090510 are shown on fig. 6.2 and the top of fig. 6.3, while the light curves of the GRB 130427A are shown on fig. 6.5 and the top of fig. 6.6. The differences between the number of simulated and reconstructed events are due mainly to the reconstruction efficiency rather than the pile-up. Indeed, considering all the events that cross the tracker, pre-shower or calorimeter, the pile-up occurs in only in the 0.25% of the cases for the baseline and 1.09% of the cases for the enhanced configuration for the GRB 090510 and in less than $\sim 0.1\%$ in both configurations for the GRB 130427A. The shape of the light curve obtained with the overall reconstruction maps very well the original light curve, exhibiting both the peaks and the continuum.
The analysis of the results of the calorimeter only and preshower only reconstruction is more complicated. While a peak seems to be detected by both configurations in the GRB 090510, in the GRB 130427A there is no indication of an underlying structure. Taking in consideration that only the timing, not the energy, of the photons is taken from the Fermi data and that at energies higher than 8 GeV (minimum energy for the reconstruction using only information from the calorimeter) the background contribution is limited (see also chap. 4.5.4), the absence of a visible peak in the reconstructed light curve is negligible. Not even the high energy Fermi data show a clear indication of a peak in the GRB 130427A, as visible in fig. 6.4.

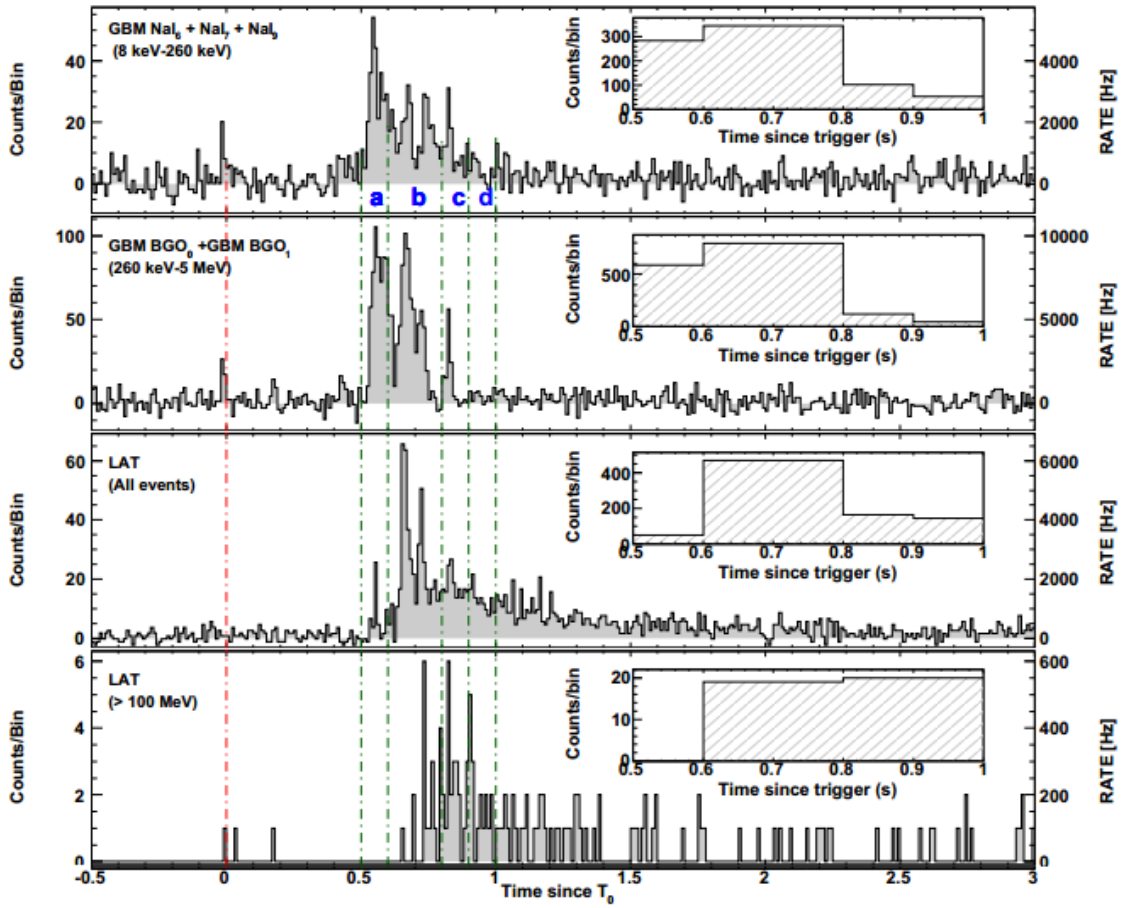

Figure 6.1: Light curves of the GRB 090510 as seen by Fermi GBM (top two panels) and LAT (bottom two panels) from lowest to highest energies. The bin size is 0.01s. The insets show the counts per bin within the time intervals labelled as a to d [109].

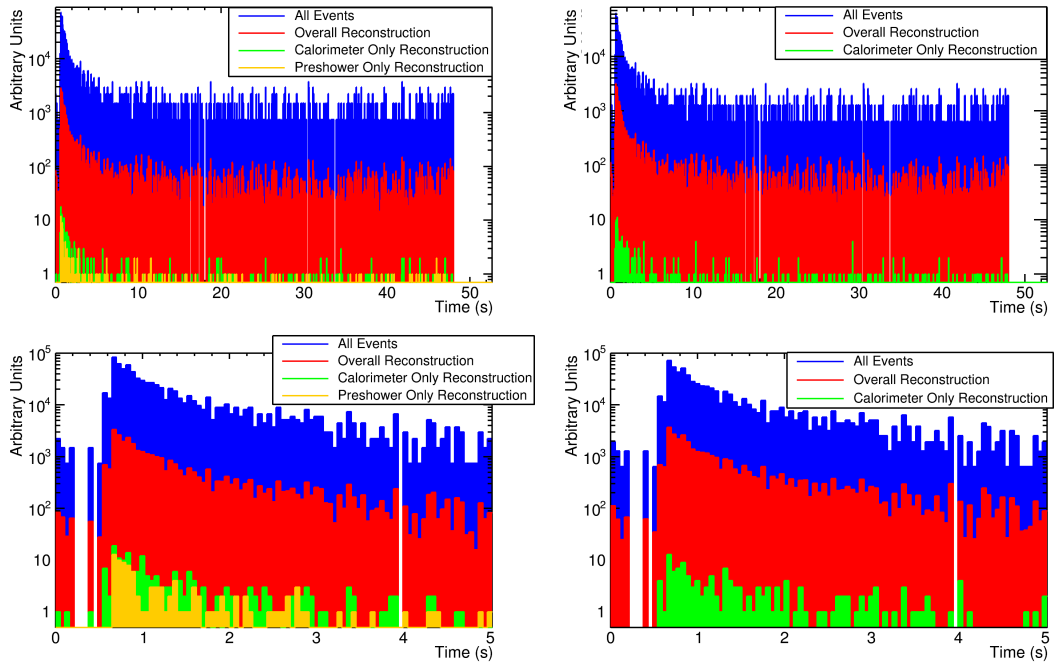

Figure 6.2: *Top*: Light curves of the stacked simulations of the GRB 090510 as seen by the baseline (*left*) and the enhanced configuration (*right*). In blue all the simulated events, red the events reconstructed with the overall procedure, green the events reconstructed using only the calorimeter and orange the events reconstructed using only the pre-shower. *Bottom*: Same as top but with a zoom on the first 5 s.

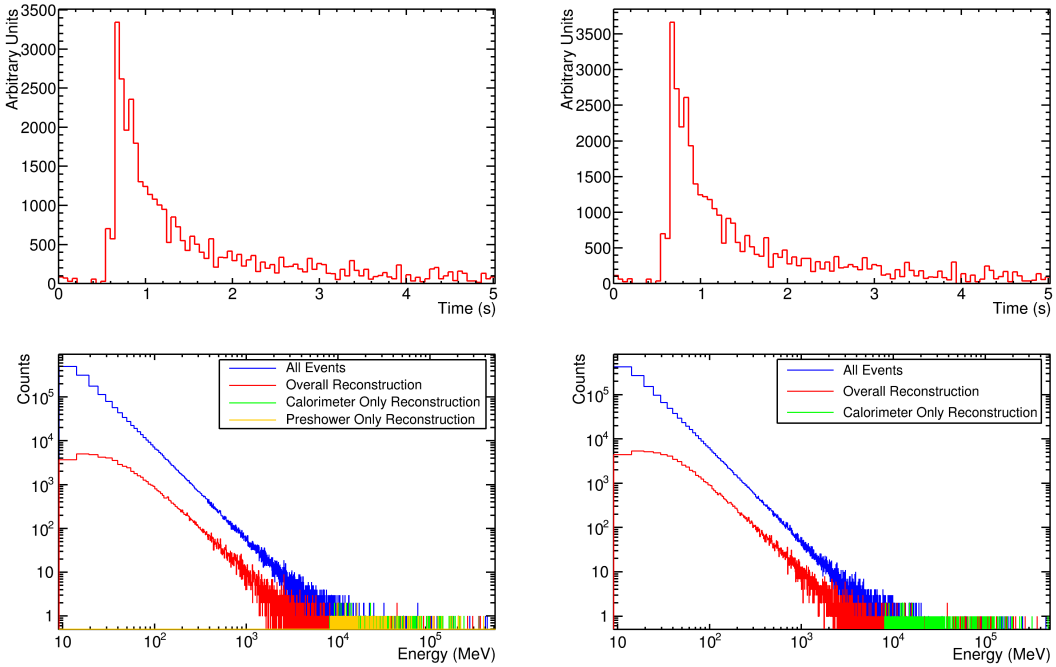

Figure 6.3: *Top*: Light curves of the stacked simulations of the GRB 090510 as seen by the baseline (*left*) and the enhanced configuration (*right*) using the overall reconstruction. The results are the same presented on the bottom of fig. 6.2 but with a linear scale. *Bottom*: Simulated energy of all the gamma rays compared to the simulated energy of the events reconstructed by the overall algorithm (red), only the calorimeter (green) and only the pre-shower (orange). The results of the baseline are presented on the left while the results for the enhanced configuration are shown on the right.

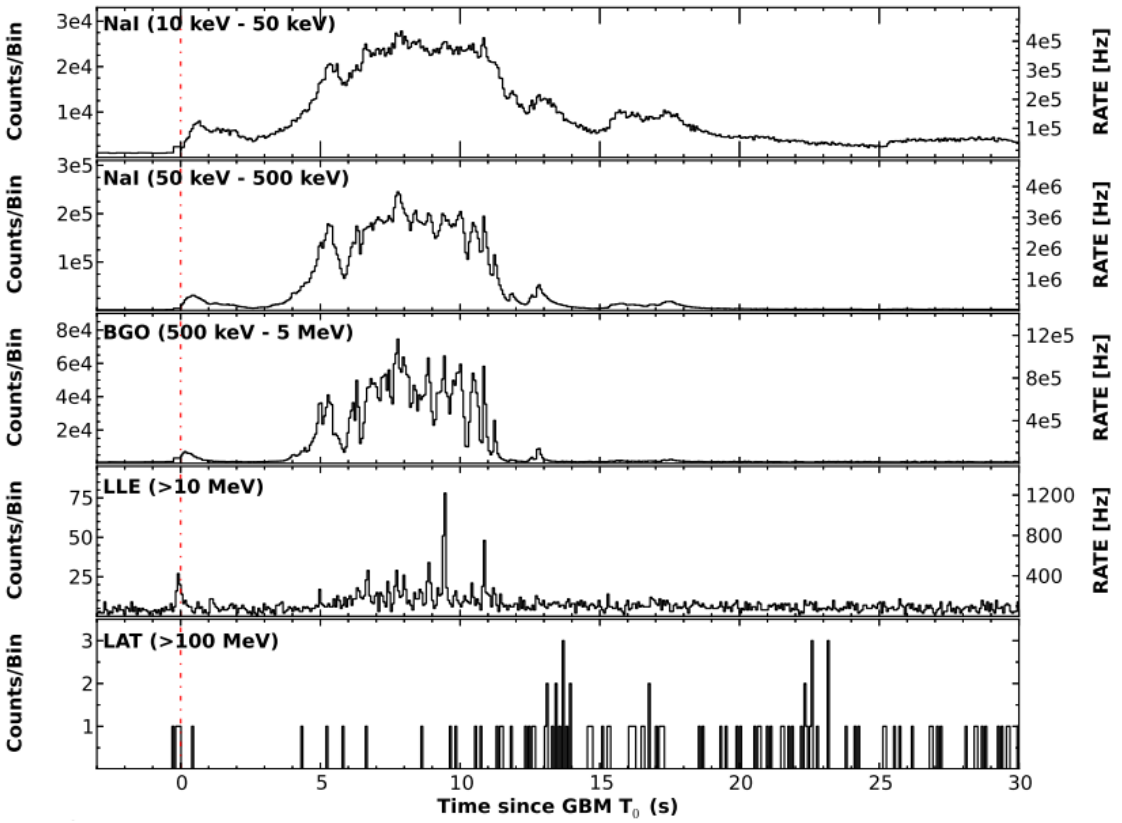

Figure 6.4: Light curves of the GRB 130427A as seen by Fermi GBM (top two panels) and LAT (bottom two panels) from lowest to highest energies in 0.064s bins [79].

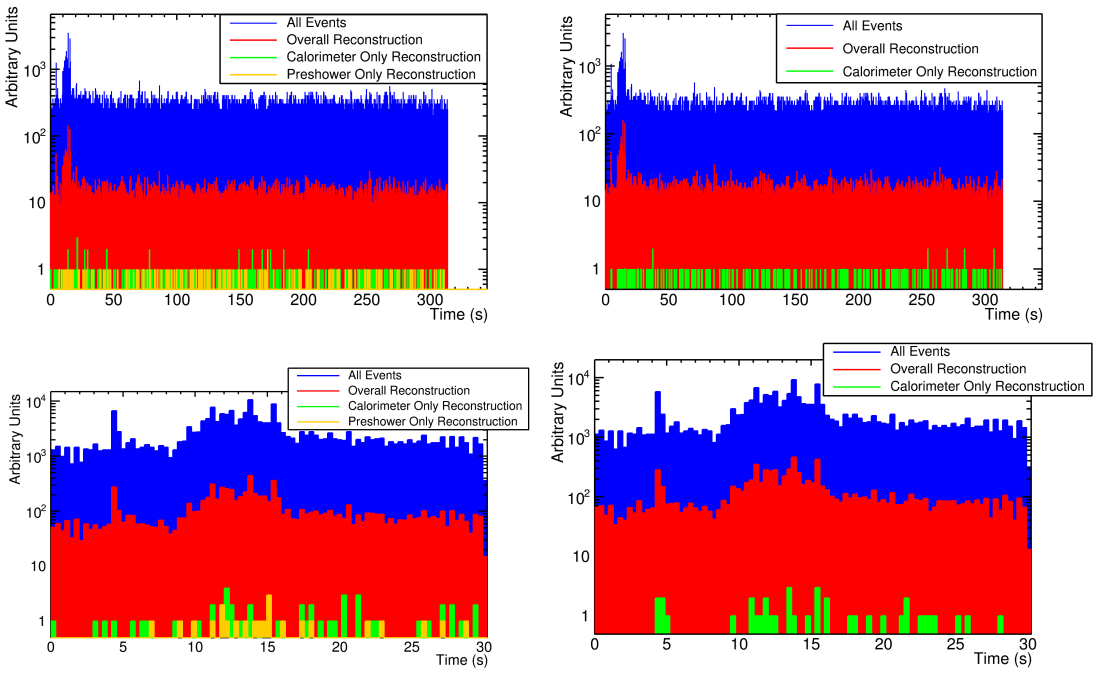

Figure 6.5: *Top*: Light curves of the stacked simulations of the GRB 130427A as seen by the baseline (*left*) and the enhanced configuration (*right*). In blue all the simulated events, red the events reconstructed with the overall procedure, green the events reconstructed using only the calorimeter and orange the events reconstructed using only the pre-shower. *Bottom*: Same as top but with a zoom on the first 30 s.

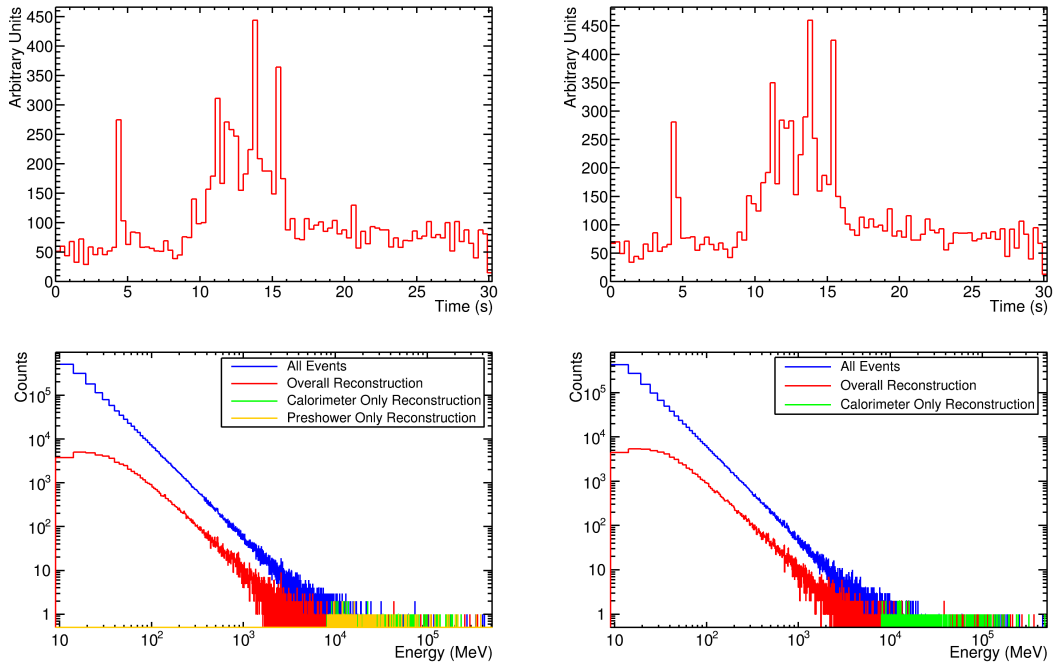

Figure 6.6: *Top*: Light curves of the stacked simulations of the GRB 130427A as seen by the baseline (*left*) and the enhanced configuration (*right*) using the overall reconstruction. The results are the same presented on the bottom of fig. 6.5 but with a linear scale. *Bottom*: Simulated energy of all the gamma rays compared to the simulated energy of the events reconstructed by the overall algorithm (red), only the calorimeter (green) and only the pre-shower (orange). The results of the baseline are presented on the left while the results for the enhanced configuration are shown on the right.

GRB 090510

N×Flux	Baseline	Enhanced
1	0.25%	1.09%
2	0.66%	1.15%
3	1.08%	1.82%
5	1.70%	3.04%
10	3.37%	5.70%

GRB 130427

N×Flux	Baseline	Enhanced
1	0.06%	0.12%
2	0.16 %	0.30%
3	0.28 %	0.44%
5	0.44 %	0.79%
10	0.86 %	1.63%

Table 6.2: Percentage of the piled-up events over the total number of events that cross the tracker, pre-shower or calorimeter at different fluxes, for the GRB 090510 (*left*) and GRB 130427A (*right*).

The ability of the instrument to reconstruct gamma rays in the different energy ranges is shown on the bottom of fig. 6.3 and fig. 6.6. Both instrument have a good coverage of the gamma rays with energy higher than 8 GeV, better for the baseline thanks to a larger total effective area (∼67% events reconstructed for the baseline and ∼57% for the enhanced configuration). These events are reconstructed mainly by the calorimeter and pre-shower only: for the baseline 76% of the reconstructed events, 58% for the enhanced configuration. At low energy the efficiency of the reconstruction drops, reaching a minimum for energies lower than 50 MeV. In this energy range the reconstruction is indeed very difficult because of the strong multiple scattering experienced by the pair created by the gamma ray. To assess the feasibility of GRB study at higher fluxes, the timing of the photon arrival is reduced by a factor of 2, 3, 5 and 10, simulating an increase of the GRB flux. The results are presented in table 6.2. Even with a flux ten time higher than the original, the percentage of piled-up events is always lower than the 6%. It should be also noted that both these GRBs have already a high flux in comparison to other GRBs. A pile-up related loss of less than 6% of the events it can then be considered acceptable and the GRB study with the main instrumentation aboard GAMMA-400 can be done even for the higher of the fluxes.

Conclusions

GAMMA-400 is a dual experiment, devoted to the study of both cosmic rays, protons and nuclei up to an energy of $10^{15} - 10^{16}$ eV and electrons up to the TeV energy range, and gamma rays, from 50 MeV up to few TeV. Using a multimessenger approach, GAMMA-400 will hopefully succeed in explaining the mechanism of acceleration and propagation of cosmic rays as well as identify their sources. It will also be able to search for possible signal from dark matter annihilation or decay, as well as study gamma-ray sources, such as active galactic nuclei, supernova remnants, pulsars and gamma-ray bursts (GRBs). In this thesis the gamma-ray performance of the main instrumentation of GAMMA-400 are estimated. Two different configurations are taken into consideration: the baseline and the so-called enhanced configuration, proposed by the Italian team. The main differences between these two configurations are in the tracker and in the calorimeter. The baseline tracker is composed by ten planes of silicon, eight of which comprise also a $\sim$0.1 X_0 tungsten layer, while the tracker of the enhanced configuration is composed by 25 planes of interleaved silicon and tungsten ($\sim$0.03 X_0 each). The calorimeter of the baseline is divided in two: a first part composed by two planes of caesium iodide and silicon and a second part composed by an array of $28\times28\times12$ caesium iodide cubes. The calorimeter of the enhanced configuration is instead composed only by caesium iodide cubes, arranged in a $20\times20\times20$ array.
To perform the estimation of the performance, a direction reconstruction algorithm is developed. The reconstruction can make use of the information from the tracker, calorimeter and pre-shower, present only in the baseline, both singularly and jointly. The direction obtained using only information from the calorimeter or the pre-shower, while affected by a worse angular resolution, can be helpful in rising the effective area at high energy and to trigger observations of transients from the ground with Cherenkov telescopes. The overall angular resolution is found to be better in the case of the enhanced configuration. At low energy this is due to the less tungsten in the tracker, and consequently less multiple scattering. The smaller but deeper calorimeter of the enhanced configuration hinders a good reconstruction of the energy for high energy gamma rays interacting in the tracker and

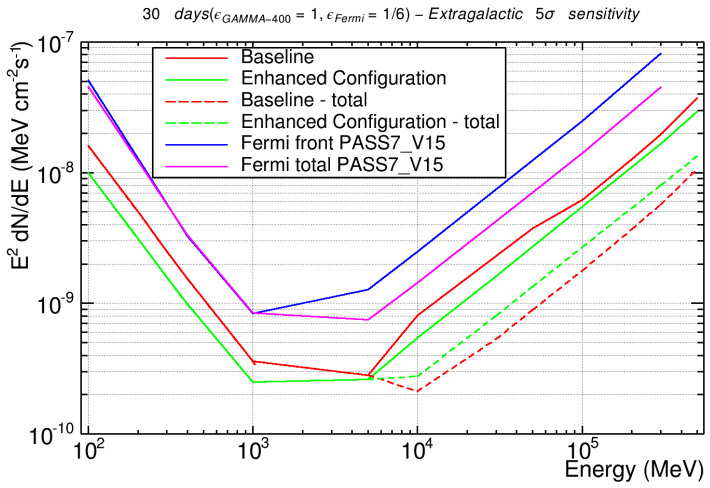

Figure 6.7: Point source (5σ) sensitivity of both configuration of GAMMA-400, Fermi front and Fermi total, derived using the same method. An extragalactic background [54] is assumed for an observation time of 1 month. The dashed lines are computed using the total PSF and effective area, result of the reconstruction using, in order: the tracker, only the pre-shower, in the case of the baseline, and only the calorimeter.

it also produces less backsplashed particles that worsen the track reconstruction. The total effective area of the baseline, counting on a bigger calorimeter and the pre-shower, is bigger, leading to better point source sensitivity for energies higher than 5 GeV. The angular resolution and the effective area, as well as the pointing strategy of the instrument, all contribute to the sensitivity of the satellite. The results for both configurations are compared to the results obtained for Fermi in fig. 6.7. There is also a considerable cost difference between the two configuration due to the different number of Silicon planes, making the baseline the less expensive solution.

A preliminary trigger system for observation of gamma rays using only tracker information is developed. The necessity of rejecting most of the charged particles comes from the high on-orbit background ($\sim 10^6$ protons every gamma ray) and the limited downlink capability of the satellite ($\sim$ 100 GB/day). A difference of less than 1% in the remaining rate of protons is found for the two configurations. While promising, the trigger must be improved, both in its on-board and on the ground segment. Possible improvements are outlined as well.

The reconstruction and trigger algorithm are applied to the analysis of the feasibility of gamma-ray bursts study with the main instrumentation aboard GAMMA-400. By simulating a source and taking the timing of two GRBs from the Fermi

data, an estimation of the number of events that do not get triggered because they fall in the dead time between triggers is made for both configurations. No significant percentage of pile-up is noted in either configuration. Even raising the flux of the GRBs, the percentage of piled-up events is always lower than 6%. It should however be noted that much will depend upon the design of the readout of the detectors that can considerably change the deadtime of the instrument.
The baseline configuration, taking in consideration performance and construction cost, has been officially chosen as the geometrical set-up of the satellite. Currently some possible modifications are under study within the baseline. In particular the use of 80 μm pitch strips inside the silicon planes, instead of 120 μm, as well as a reduce tungsten thickness or some more planes in the tracker, similar to the enhanced configuration, can both help to increase the angular resolution of GAMMA-400 in all the energy ranges.

Bibliography

[1] T. Tait. Perspectives on dark matter interactions, 19-21 September 2013. URL `https://kicp-workshops.uchicago.edu/DM-LHC2013/depot/talk-tait-tim.pdf`. Dark Matter at LHC.

[2] P. Cushman et al. Snowmass CF1 Summary: WIMP Dark Matter Direct Detection. *ArXiv e-prints*, October 2013.

[3] T. Bringmann, C. Weniger. Gamma ray signals from dark matter: Concepts, status and prospects. *Physics of the Dark Universe*, 1:194–217, November 2012. doi: 10.1016/j.dark.2012.10.005.

[4] E. A. Baltz et al. Pre-launch estimates for GLAST sensitivity to dark matter annihilation signals. *Journal of Cosmology and Astro-Particle Physics*, 7:13, 2008.

[5] W. B. Atwood et al. The Large Area Telescope on the Fermi Gamma-Ray Space Telescope Mission. *The Astrophysical Journal*, 697:1071–1102, 2009.

[6] M. Ackermann et al. Constraining Dark Matter Models from a Combined Analysis of Milky Way Satellites with the Fermi Large Area Telescope. *Physical Review Letters*, 107(24):241302, 2011.

[7] M. Ackermann et al. Dark matter constraints from observations of 25 MilkyÂ Way satellite galaxies with the Fermi Large Area Telescope. Phys. Rev. D, 89(4):042001, February 2014. doi: 10.1103/PhysRevD.89.042001.

[8] T. Bringmann et al. Fermi LAT search for internal bremsstrahlung signatures from dark matter annihilation. *Journal of Cosmology and Astro-Particle Physics*, 7:054, July 2012. doi: 10.1088/1475-7516/2012/07/054.

[9] Fermi-LAT Collaboration. Search for Gamma-ray Spectral Lines with the Fermi Large Area Telescope and Dark Matter Implications. *ArXiv e-prints*, May 2013.

[10] C. Weniger. Searches for spectral lines, 8-11 October 2013. URL `http://cdsagenda5.ictp.trieste.it/full_display.php?ida=a12213`. Workshop on the Future of Dark Matter Astro-Particle Physics.

[11] T. Daylan et al. The Characterization of the Gamma-Ray Signal from the Central Milky Way: A Compelling Case for Annihilating Dark Matter. *ArXiv e-prints*, February 2014.

[12] J. Petrović, P. Dario Serpico, G. Zaharijaš. Galactic Center gamma-ray "excess" from an active past of the Galactic Centre? J. Cosmology Astropart. Phys., 10:052, October 2014. doi: 10.1088/1475-7516/2014/10/052.

[13] A. A. Moiseev et al. Dark Matter Search Perspectives with GAMMA-400. *ArXiv e-prints*, July 2013.

[14] L. Bergström et al. Investigating gamma-ray lines from dark matter with future observatories. *Journal of Cosmology and Astro-Particle Physics*, 11: 025, November 2012. doi: 10.1088/1475-7516/2012/11/025.

[15] L. Bergström. 130 GeV fingerprint of right-handed neutrino dark matter. *Physical Review D*, 86(10):103514, November 2012. doi: 10.1103/PhysRevD.86.103514.

[16] A. W. Strong, I. V. Moskalenko, O. Reimer. Diffuse Galactic Continuum Gamma Rays: A Model Compatible with EGRET Data and Cosmic-Ray Measurements. *The Astrophysical Journal*, 613:962–976, 2004.

[17] A. A. Abdo et al. Measurement of the Cosmic Ray e^++e^- Spectrum from 20GeV to 1TeV with the Fermi Large Area Telescope. *Physical Review Letters*, 102(18):181101, 2009.

[18] E.-S. Seo et al. Advanced thin ionization calorimeter to measure ultrahigh energy cosmic rays. *Advances in Space Research*, 19:711–718, May 1997. doi: 10.1016/S0273-1177(97)00392-X.

[19] J. Chang et al. Resolving electrons from protons in ATIC. *Advances in Space Research*, 42:431–436, 2008.

[20] P. Picozza et al. PAMELA A payload for antimatter matter exploration and light-nuclei astrophysics. *Astroparticle Physics*, 27:296–315, 2007.

[21] O. Adriani et al. An anomalous positron abundance in cosmic rays with energies 1.5-100GeV. *Nature*, 458:607–609, 2009.

[22] The Fermi LAT Collaboration et al. Measurement of separate cosmic-ray electron and positron spectra with the Fermi Large Area Telescope. *ArXiv e-prints*, 2011.

[23] A. Kounine. The Alpha Magnetic Spectrometer on the International Space Station. *International Journal of Modern Physics E*, 21:1230005, August 2012. doi: 10.1142/S0218301312300056.

[24] M. Aguilar et al. First Result from the Alpha Magnetic Spectrometer on the International Space Station: Precision Measurement of the Positron Fraction in Primary Cosmic Rays of 0.5-350 GeV. *Physical Review Letters*, 110(14): 141102, April 2013. doi: 10.1103/PhysRevLett.110.141102.

[25] F. Aharonian et al. Probing the ATIC peak in the cosmic-ray electron spectrum with H.E.S.S. *Astronomy and Astrophysics*, 508:561–564, 2009.

[26] P. M. Chadwick. Status of the H.E.S.S. experiment and first results. *European Physical Journal C*, 33:935–937, 2004. doi: 10.1140/epjcd/s2004-03-1629-3.

[27] P. Meade et al. Dark Matter interpretations of the $e^{\pm}$ excesses after FERMI. *Nuclear Physics B*, 831:178–203, May 2010. doi: 10.1016/j.nuclphysb.2010.01.012.

[28] P. Picozza, M. Boezio. Multi messenger astronomy and CTA: TeV cosmic rays and electrons. *Astroparticle Physics*, 43:163–170, March 2013. doi: 10.1016/j.astropartphys.2012.07.004.

[29] J. Beringer et al. (Particle Data Group). Review of particle physics. *Physical Review D*, 86:010001, 2012.

[30] W. D. Apel et al. Kneelike Structure in the Spectrum of the Heavy Component of Cosmic Rays Observed with KASCADE-Grande. *Physical Review Letters*, 107(17):171104, October 2011. doi: 10.1103/PhysRevLett.107.171104.

[31] P. O. Lagage, C. J. Cesarsky. The maximum energy of cosmic rays accelerated by supernova shocks. *Astronomy and Astrophysics*, 125:249–257, 1983.

[32] E. Amato. The origin of galactic cosmic rays. *International Journal of Modern Physics D*, 23:1430013, May 2014. doi: 10.1142/S0218271814300134.

[33] J. R. Hörandel. Models of the knee in the energy spectrum of cosmic rays. *Astroparticle Physics*, 21:241–265, 2004.

[34] T. Kobayashi et al. The Most Likely Sources of High-Energy Cosmic-Ray Electrons in Supernova Remnants. *Astrophysical Journal*, 601:340–351, 2004.

[35] S. Profumo. The detection of a cosmic-ray electron-positron anisotropy is a sufficient (but not necessary) condition to discard a Dark Matter origin for the anomalous positron fraction. *ArXiv e-prints*, May 2014.

[36] O. Adriani et al. PAMELA Measurements of Cosmic-Ray Proton and Helium Spectra. *Science*, 332:69–, 2011.

[37] E.S. Seo et al. Cosmic-ray energetics and mass (cream) balloon project. *Advances in Space Research*, 33(10):1777 – 1785, 2004. ISSN 0273-1177. doi: http://dx.doi.org/10.1016/j.asr.2003.05.019. URL `http://www.sciencedirect.com/science/article/pii/S027311770301158X`. The Next Generation in Scientific Ballooning.

[38] H. S. Ahn et al. Discrepant Hardening Observed in Cosmic-ray Elemental Spectra. *The Astrophysical Journal Letters*, 714:L89–L93, 2010.

[39] C. Consolandi, on Behalf of the AMS-02 Collaboration. Primary Cosmic Ray Proton Flux Measured by AMS-02. *ArXiv e-prints*, February 2014.

[40] AMS-02 Collaboration, . URL `http://www.ams02.org/2013/07/new-results-from-ams-presented-at-icrc-2013/`.

[41] O. Adriani et al. Measurement of Boron and Carbon Fluxes in Cosmic Rays with the PAMELA Experiment. *The Astrophysical Journal*, 791:93, August 2014. doi: 10.1088/0004-637X/791/2/93.

[42] A. W. Strong, I. V. Moskalenko. Propagation of Cosmic-Ray Nucleons in the Galaxy. *The Astrophysical Journal*, 509:212–228, December 1998. doi: 10.1086/306470.

[43] M. Ahlers, P. Mertsch, S. Sarkar. Cosmic ray acceleration in supernova remnants and the FERMI/PAMELA data. *Physical Review D*, 80(12):123017, 2009.

[44] F. Aharonian et al. Primary particle acceleration above 100 TeV in the shell-type supernova remnant RX J1713.7-3946 with deep HESS observations. *Astronomy and Astrophysics*, 464:235–243, March 2007. doi: 10.1051/0004-6361:20066381.

[45] G. E. Allen et al. Evidence of X-Ray Synchrotron Emission from Electrons Accelerated to 40 TeV in the Supernova Remnant Cassiopeia A. *The Astrophysical Journal Letters*, 487:L97, 1997.

[46] K. Koyama et al. Evidence for shock acceleration of high-energy electrons in the supernova remnant SN1006. *Nature*, 378:255–258, 1995.

[47] M. Ackermann et al. Detection of the Characteristic Pion-Decay Signature in Supernova Remnants. *Science*, 339:807–811, February 2013. doi: 10.1126/science.1231160.

[48] A. Giuliani et al. Neutral Pion Emission from Accelerated Protons in the Supernova Remnant W44. *The Astrophysical Journal Letters*, 742:L30, December 2011. doi: 10.1088/2041-8205/742/2/L30.

[49] M. Cardillo et al. The supernova remnant W44: Confirmations and challenges for cosmic-ray acceleration. *Astronomy and Astrophysics*, 565:A74, May 2014. doi: 10.1051/0004-6361/201322685.

[50] F. Giordano et al. Fermi Large Area Telescope Detection of the Young Supernova Remnant Tycho. *The Astrophysical Journal Letters*, 744:L2, January 2012. doi: 10.1088/2041-8205/744/1/L2.

[51] P. F. Michelson, W. B. Atwood, S. Ritz. Fermi Gamma-ray Space Telescope: high-energy results from the first year. *Reports on Progress in Physics*, 73 (7):074901, 2010.

[52] A. A. Abdo et al. The Fermi-LAT High-Latitude Survey: Source Count Distributions and the Origin of the Extragalactic Diffuse Background. *The Astrophysical Journal*, 720:435–453, September 2010. doi: 10.1088/0004-637X/720/1/435.

[53] A. A. Abdo et al. Fermi Observations of Cassiopeia and Cepheus: Diffuse Gamma-ray Emission in the Outer Galaxy. *The Astrophysical Journal*, 710: 133–149, 2010.

[54] A. A. Abdo et al. Spectrum of the Isotropic Diffuse Gamma-Ray Emission Derived from First-Year Fermi Large Area Telescope Data. *Physical Review Letters*, 104(10):101101, 2010.

[55] T. DeYoung, HAWC Collaboration. The HAWC observatory. *Nuclear Instruments and Methods in Physics Research A*, 692:72–76, November 2012. doi: 10.1016/j.nima.2012.01.026.

[56] Fermi-LAT Collaboration. The Spectrum and Morphology of the Fermi Bubbles. *ArXiv e-prints*, July 2014.

[57] M. Su, T. R. Slatyer, D. P. Finkbeiner. Giant Gamma-ray Bubbles from Fermi-LAT: Active Galactic Nucleus Activity or Bipolar Galactic Wind? *The Astrophysical Journal*, 724:1044–1082, December 2010. doi: 10.1088/0004-637X/724/2/1044.

[58] S. L. Snowden et al. ROSAT Survey Diffuse X-Ray Background Maps. II. *The Astrophysical Journal*, 485:125–135, August 1997.

[59] C. J. Law. A Multiwavelength View of a Mass Outflow from the Galactic Center. *The Astrophysical Journal*, 708:474–484, January 2010. doi: 10.1088/0004-637X/708/1/474.

[60] C. L. Bennett et al. The Microwave Anisotropy Probe Mission. ApJ, 583: 1–23, January 2003. doi: 10.1086/345346.

[61] D. P. Finkbeiner. Microwave Interstellar Medium Emission Observed by the Wilkinson Microwave Anisotropy Probe. *The Astrophysical Journal*, 614: 186–193, October 2004. doi: 10.1086/423482.

[62] The Planck Collaboration. The Scientific Programme of Planck. *ArXiv Astrophysics e-prints*, April 2006.

[63] Planck Collaboration et al. Planck intermediate results. IX. Detection of the Galactic haze with Planck. *Astronomy and Astrophysics*, 554:A139, June 2013. doi: 10.1051/0004-6361/201220271.

[64] F. Guo, W. G. Mathews. The Fermi Bubbles. I. Possible Evidence for Recent AGN Jet Activity in the Galaxy. ApJ, 756:181, September 2012. doi: 10.1088/0004-637X/756/2/181.

[65] K. Zubovas, A. R. King, S. Nayakshin. The Milky Way's Fermi bubbles: echoes of the last quasar outburst? MNRAS, 415:L21–L25, July 2011. doi: 10.1111/j.1745-3933.2011.01070.x.

[66] R. M. Crocker, F. Aharonian. Fermi Bubbles: Giant, Multibillion-Year-Old Reservoirs of Galactic Center Cosmic Rays. *Physical Review Letters*, 106 (10):101102, March 2011. doi: 10.1103/PhysRevLett.106.101102.

[67] K.-S. Cheng et al. Origin of the Fermi Bubble. ApJ, 731:L17, April 2011. doi: 10.1088/2041-8205/731/1/L17.

[68] M. Ackermann et al. The Second Catalog of Active Galactic Nuclei Detected by the Fermi Large Area Telescope. ApJ, 743:171, December 2011. doi: 10.1088/0004-637X/743/2/171.

[69] H. Krawczynski, E. Treister. Active galactic nuclei - the physics of individual sources and the cosmic history of formation and evolution. *Frontiers of Physics*, 8:609–629, December 2013. doi: 10.1007/s11467-013-0310-3.

[70] A. A. Abdo et al. Gamma-ray Light Curves and Variability of Bright Fermi-detected Blazars. ApJ, 722:520–542, October 2010. doi: 10.1088/0004-637X/722/1/520.

[71] P. L. Nolan et al. Fermi Large Area Telescope Second Source Catalog. ApJS, 199:31, April 2012. doi: 10.1088/0067-0049/199/2/31.

[72] R. Bühler, R. Blandford. The surprising Crab pulsar and its nebula: a review. *Reports on Progress in Physics*, 77(6):066901, June 2014. doi: 10.1088/0034-4885/77/6/066901.

[73] M. Tavani et al. Science with AGILE. In S. Ritz, N. Gehrels, C. R. Shrader, editors, *Gamma 2001: Gamma-Ray Astrophysics*, volume 587 of *American Institute of Physics Conference Series*, pages 729–738, October 2001. doi: 10.1063/1.1419490.

[74] M. Tavani et al. Discovery of Powerful Gamma-Ray Flares from the Crab Nebula. *Science*, 331:736–, 2011.

[75] A. A. Abdo et al. Gamma-Ray Flares from the Crab Nebula. *Science*, 331:739–, February 2011. doi: 10.1126/science.1199705.

[76] E. Striani et al. Variable Gamma-Ray Emission from the Crab Nebula: Short Flares and Long "Waves". ApJ, 765:52, March 2013. doi: 10.1088/0004-637X/765/1/52.

[77] M. Ackermann et al. The First Fermi-LAT Gamma-Ray Burst Catalog. ApJS, 209:11, November 2013. doi: 10.1088/0067-0049/209/1/11.

[78] A. A. Abdo et al. Fermi Observations of GRB 090902B: A Distinct Spectral Component in the Prompt and Delayed Emission. *The Astrophysical Journal Letters*, 706:L138–L144, 2009.

[79] M. Ackermann et al. Fermi-LAT Observations of the Gamma-Ray Burst GRB 130427A. *Science*, 343:42–47, January 2014. doi: 10.1126/science.1242353.

[80] W. B. Atwood et al. New Fermi-LAT Event Reconstruction Reveals More High-energy Gamma Rays from Gamma-Ray Bursts. ApJ, 774:76, September 2013. doi: 10.1088/0004-637X/774/1/76.

[81] J. Biteau. Constraining gamma-ray propagation on cosmic distances. In L. Cambresy et al., editors, *SF2A-2013: Proceedings of the Annual meeting of the French Society of Astronomy and Astrophysics*, pages 303–312, November 2013.

[82] A. A. Abdo et al. Fermi Large Area Telescope Constraints on the Gamma-ray Opacity of the Universe. ApJ, 723:1082–1096, November 2010. doi: 10.1088/0004-637X/723/2/1082.

[83] M. Tavani et al. The AGILE Mission. *Astronomy and Astrophysics*, 502: 995–1013, 2009.

[84] A. W. Chen et al. Calibration of AGILE-GRID with in-flight data and Monte Carlo simulations. A&A, 558:A37, October 2013. doi: 10.1051/0004-6361/201321767.

[85] Fermi LAT Collaboration, . URL `http://www.slac.stanford.edu/exp/glast/groups/canda/lat_Performance.htm`.

[86] C. Meegan et al. The Fermi Gamma-ray Burst Monitor. ApJ, 702:791, September 2009. doi: 10.1088/0004-637X/702/1/791.

[87] V. A. Dogiel et al. Some tasks of observational gamma-ray astronomy in the energy range 5-400 GeV. *Space Science Reviews*, 49:215–226, 1988.

[88] V.L. Ginzburg et al. Russian version of telescope to record diffuse gamma-rays in energy range 10 to 1000 GeV. *Bulletin of the Russian Academy of Sciences: Physics*, 69:489–492, 2005.

[89] A. M. Galper et al. Design and performance of the GAMMA-400 gamma-ray telescope for dark matter searches. In J. F. Ormes, editor, *American Institute of Physics Conference Series*, volume 1516 of *American Institute of Physics Conference Series*, pages 288–292, February 2013. doi: 10.1063/1.4792586.

[90] G. F. Bignami et al. The COS-B experiment for gamma-ray astronomy. *Space Science Instrumentation*, 1:245–268, August 1975.

[91] A. M. Galper et al. The Space-Based Gamma-Ray Telescope GAMMA-400 and Its Scientific Goals. *ArXiv e-prints*, June 2013.

[92] G. Barbiellini et al. The AGILE silicon tracker: testbeam results of the prototype silicon detector. *Nuclear Instruments and Methods in Physics Research A*, 490:146–158, September 2002. doi: 10.1016/S0168-9002(02)01062-8.

[93] The Italian GAMMA-400 Collaboration. GAMMA-400: Gamma-Ray and Particle Physics in Space, an overview. Private document for the INFN CSN2, 2013.

[94] V. V. Kadilin et al. Neutron Detector for the GAMMA-400 Space Observatory. In Prof. Dr. G. Ristic, editor, *Second International Conference on Radiation and Dosimetry in Various Fields of Research - RAD 2014*, pages 5–7, 2014.

[95] E. Mocchiutti et al. The GAMMA-400 Space Experiment: Gammas, Electrons and Nuclei Measurements. *Nucl.Phys.Proc.Suppl.*, 239-240:204–209, 2013. doi: 10.1016/j.nuclphysbps.2013.05.047.

[96] N. Mori et al. Homogeneous and isotropic calorimetry for space experiments. *Nuclear Instruments and Methods in Physics Research Section A: Accelerators, Spectrometers, Detectors and Associated Equipment*, 732(0): 311 – 315, 2013. ISSN 0168-9002. doi: http://dx.doi.org/10.1016/j.nima.2013.05.138. URL `http://www.sciencedirect.com/science/article/pii/S0168900213007493`. Vienna Conference on Instrumentation 2013.

[97] Alfredo Ferrari et al. FLUKA: A multi-particle transport code (Program version 2005). 2005.

[98] G. Battistoni et al. The FLUKA code: description and benchmarking. In M. Albrow, R. Raja, editors, *Hadronic Shower Simulition Workshop*, volume 896 of *American Institute of Physics Conference Series*, pages 31–49, March 2007. doi: 10.1063/1.2720455.

[99] S. Agostinelli, et al. GEANT4: A simulation toolkit. *Nucl. Instrum. Meth.*, A506:250–303, 2003.

[100] R. Frühwirth. Application of Kalman filtering to track and vertex fitting. *Nuclear Instruments and Methods in Physics Research A*, 262:444–450, December 1987. doi: 10.1016/0168-9002(87)90887-4.

[101] R. Turchetta. Spatial resolution of silicon microstrip detectors. *Nuclear Instruments and Methods in Physics Research A*, 335:44–58, October 1993. doi: 10.1016/0168-9002(93)90255-G.

[102] B. B. Jones. A Search for Gamma-Ray Bursts and Pulsars, and the Application of Kalman Filters to Gamma-Ray Reconstruction. *ArXiv Astrophysics e-prints*, February 2002.

[103] A. Giuliani. Studio e Ottimizzazione della Risoluzione Angolare del Telescopio Spaziale per Astronomia Gamma AGILE,. Master Thesis, Università degli Studi di Pavia, 2001.

[104] C. Pittori, M. Tavani. Gamma-ray imaging by silicon detectors in space: the AREM method. *Nuclear Instruments and Methods in Physics Research A*, 488:295–306, August 2002.

[105] A. A. Leonov et al. The GAMMA-400 gamma-ray telescope characteristics. Angular resolution and electrons/protons separation. *ArXiv e-prints*, December 2014.

[106] F. Longo, V. Cocco, M. Tavani. Simulation of the AGILE gamma-ray imaging detector performance: part I. *Nuclear Instruments and Methods in Physics Research A*, 486:610–622, July 2002. doi: 10.1016/S0168-9002(01)02159-3.

[107] V. Cocco, F. Longo, M. Tavani. Simulation of the AGILE gamma-ray imaging detector performance: Part II. *Nuclear Instruments and Methods in Physics Research A*, 486:623–638, July 2002. doi: 10.1016/S0168-9002(01)02160-X.

[108] M. Ackermann et al. The Fermi Large Area Telescope on Orbit: Event Classification, Instrument Response Functions, and Calibration. ApJS, 203:4, November 2012. doi: 10.1088/0067-0049/203/1/4.

[109] M. Ackermann et al. Fermi Observations of GRB 090510: A Short-Hard Gamma-ray Burst with an Additional, Hard Power-law Component from 10 keV TO GeV Energies. ApJ, 716:1178–1190, June 2010. doi: 10.1088/0004-637X/716/2/1178.

[110] V. Pelassa et al. The LAT Low-Energy technique for Fermi Gamma-Ray Bursts spectral analysis. *ArXiv e-prints*, February 2010.